HIGHLY-DISPERSED IRIDIUM CATALYSTS WITH SUB-NANOMETER DIAMETERS FOR CARBON MONOXIDE OXIDATION

A THESIS SUBMITTED

TO THE GRADUATE SCHOOL OF ENGINEERING AND SCIENCE

OF BILKENT UNIVERSITY

IN PARTIAL FULFILLMENT OF THE REQUIREMENTS FOR

THE DEGREE OF

MASTER OF SCIENCE

IN

CHEMISTRY

By

SEYEDSABER HOSSEINI

September 2021

I certify that I have read this thesis and that in my opinion it is fully adequate, in scope and in quality, as a thesis for the degree of Master of Science.

.....

Prof. Emrah Özensoy (Advisor)

I certify that I have read this thesis and that in my opinion it is fully adequate, in scope and in quality, as a thesis for the degree of Master of Science

.....

Assist. Prof. Dr. Ferdi Karadaş

I certify that I have read this thesis and that in my opinion it is fully adequate, in scope and in quality, as a thesis for the degree of Master of Science

.....

Assist. Prof. Dr. Zafer Say

Approved for the Graduate School of Engineering and Science:

.....

Prof. Dr. Ezhan Karaşan

Director of the Graduate School

ABSTRACT

HIGHLY-DISPERSED IRIDIUM CATALYSTS WITH SUB-NANOMETER DIAMETERS FOR CARBON MONOXIDE OXIDATION

Seyedsaber Hosseini
M.S. in Chemistry
Supervisor: Prof. Dr. Emrah Özensoy
September 13, 2021

Novel catalytic architectures composed of catalytic centers with sub-nanometer diameters for CO oxidation reaction were designed, synthesized, and characterized. Accordingly, well-dispersed iridium precious metal active sites were supported on various catalytic support materials. Namely, magnesium oxide (MgO), ceria (CeO_2), lanthana-zirconia (La_2O_3–ZrO_2) and titania-zirconia (TiO_2–ZrO_2) systems were chosen as different support systems. The favorable catalytic effect of highly-dispersed Ir active sites with sub-nanometer diameters were demonstrated in flow-mode catalytic performance tests, where the lower loadings of highly dispersed Ir sites showed comparable catalytic activity in CO oxidation to that of bigger Ir clusters with higher metal loading. Furthermore, influence of the catalyst pre-treatment conditions (e.g., reduction in H_2, oxidation in O_2, and calcination in air) on the catalyst structure and performance were also studied via XRD, Raman, BET, XPS, TEM, EDX, and in-situ FTIR spectroscopy techniques. Our results indicate that in all the catalytic systems, high-dispersion Ir sites can be generated on supports where Ir exists as small clusters with < 1 nm particle size. Moreover, catalyst pretreatment conditions revealed noticeable alterations in the catalyst structure in terms of average support particle size, reduction extent of the support, specific surface area, pore volume, pore size, and Ir oxidation state. Finally, catalytic performance results indicated that under reaction conditions yielding close to 100% CO conversion, 0.2 and 0.5 wt.% Ir catalysts led to comparable performance to that of 1 wt.% Ir catalyst demonstrating the advantage of catalytic systems with highly dispersed sub-nanometer diameter active sites with extremely low metal loading.

Keywords: Air pollution, CO oxidation, sub-nanometer diameter, metal-support system, heterogeneous catalysis, high dispersion, selectivity, activity.

ÖZET

KARBON MONOKSİT OKSİDASYONU İÇİN YÜKSEK YÜZEY DAĞILIMLI ve NANOMETREDEN KÜÇÜK ÇAPLI İRİDYUM KATALİZÖRLER

Seyedsaber Hosseini

Kimya Yüksek Lisans

Danışman: Prof. Dr. Emrah Özensoy

13 Eylül 2021

CO oksidasyon reaksiyonu için 1 nm'den küçük çaplı katalitik merkezlere sahip, özgün katalitik yapılar tasarlanmış ve sentezlenmiştir. Bu yapıların karakterizasyon çalışmaları yürütülmüştür. Yüksek yüzey dağılımlı değerli iridyum metali aktif siteleri, çeşitli katalitik destek malzemeleri üzerine dağıtılmıştır. Destek malzemesi olarak magnezyum oksit (MgO), seryum oksit (CeO_2), lantan-zirkonyum oksit (La_2O_3–ZrO_2) ve titanyum-zirkonyum oksit (TiO_2–ZrO_2) kullanılmıştır. Yüksek yüzey dağılımlı Ir aktif sitelerinin olumlu katalitik etkisi, akış modunda katalitik performans testleriyle kanıtlanmıştır. CO oksidasyonunda, bu sitelerin düşük metal yüklemeleri daha yüksek metal yüklenmiş büyük Ir kümeleriyle karşılaştırılabilir katalitik aktivite göstermiştir. Ayrıca, katalizöre uygulanan ön işlemlerin (H_2 ile indirgenme, O_2 ile oksidasyon, hava ortamında kalsinasyon) katalizör yapısına ve performansına etkisi karakterizasyon yöntemleriyle araştırılmıştır. Karakterizasyon çalışmalarında, XRD, Raman, BET, XPS, TEM, EDX, ve in-situ FTIR spektroskopi tekniklerinden yararlanılmıştır. Tüm katalitik sistemlerde, yüksek yüzey dağılımlı Ir sitelerinin 1 nm'den küçük parçacık boyutundaki Ir kümelerinde oluşturulabildiği görülmüştür. Bunlara ek olarak, katalizör ön işlemlerinin katalizör yapısında gözle görülür değişiklikler meydana getirdiği ortaya konmuştur. Ortalama destek parçacık boyutu, desteğin indirgenme derecesi, Ir oksidasyon derecesi, spesifik yüzey alanı, gözenek hacmi ve boyutunda değişiklikler gözlemlenmiştir. Son olarak, kütlece % 0,2 ve % 0,5 Ir katalizörlerinin, kütlece %1 Ir katalizörüyle karşılaştırılabilir performanslar sergilediği katalitik performans çalışmalarında belirtilmiştir. Bu da küçük çaplı, yüksek yüzey dağılımlı aktif sitelerin bulunduğu katalitik sistemlerin, son derece düşük metal yüklemelerinde de avantajlı olduğunu ortaya koymaktadır.

Anahtar Kelimeler: Hava Kirliliği, CO oksidasyonu, küçük nanometre çap, metal-destek sistemi, heterojen kataliz, yüksek yüzey dağılımı, seçicilik, aktivite.

To my sisters

Parents

And sincere friends

ACKNOWLEDGEMENT

I would like to extend my gratitude to;

Prof. Dr. Emrah Özensoy for his endless encouragement, supervision, and kind supports throughout my studies. It was a priceless opportunity to work in his research group; my group members for their kindness and sincere support; the UNAM Scientific and Technical Research Center for its helpful technicians and high-level instruments.

A special thank you to Assist. Prof. Zafer Say for his endless kindness, who guided me in carrying out my work.

In addition, I would like to thank my M.Sc. thesis committee member Assist. Prof. Ferdi Karadaş.

TABLE OF CONTENTS

LIST OF FIGURES

LIST OF TABLES

LIST of ABBREVIATIONS

BET: Brunauer-Emmett-Teller

FTIR: Fourier Transform Infrared Spectroscopy

HAADF: High-Angle Annular Dark Field

JCPDS: Joint Committee on Powder Diffraction Standards

ICDD: International Center for Diffraction Database

QMS: Quadruple Mass Spectrometer

TEM-EDX: Transmission Electron Microscopy-Energy Dispersive X-ray

HRTEM: High Resolution Transmission Electron Microscopy

TOF: Turnover Frequency

TPD: Temperature Programmed Desorption

XRD: X-Ray Diffraction

SMSI: Strong Metal Support Interaction

XPS: X-ray Photoelectron Spectroscopy

NPs: Nano Particles

MCT: Mercury Cadmium Telluride

SSA: Specific Surface Area

WHSV: Weight Hourly Space Velocity

GHSV: Gas Hourly Space Velocity

UHV: Ultra High Vacuum

WHO: World Health Organization

PGM: Platinum Metal Group

CI: Classical Impregnation

IWI: Incipient to Wetness Impregnation

HFR: High Flow Rate

MFR: Moderate Flow Rate

1. INTRODUCTION

1.1 Overview

Emission of highly toxic and dangerous pollutants into the environment is a leading global problem (Figures 1-2) [1]. Various gases (such as ammonia, carbon monoxide, sulfur dioxide, nitrous oxides, methane, and chlorofluorocarbons), particulates (both organic and inorganic), and biological molecules could contribute to air pollution [2]. Chemical pollution in the air severely affects ca. 7 million people globally every year leading to a high number of casualties. Based on World Health Organization (WHO)'s report, about 90% of the people in all over the world breathe polluted air [3].

Figure 1. Industrial revolution and air pollution [1].

Figure 2. Urban air pollution and smog [1].

1.1.1 Air Pollution and its Effects on Human Health

Figures 3, 4 and 5 show different possible sources of pollution. Figure 6 demonstrates typical damaging effects of air pollution on human health, including respiratory infections, heart diseases, stroke, and lung cancer [6]. Other detrimental health effects may include difficulty in breathing, wheezing, coughing, asthma, and worsening of pre-existing respiratory and cardiac conditions. These side effects can lead to increased medication use, more doctor or emergency room visits, more hospital admissions, and premature death. Poor air quality has far-reaching effects on human health, but it primarily affects the respiratory and cardiovascular systems. Individual responses to

air pollutants vary depending on the type of pollutant, the degree of exposure, and the individual's health status and genetics [5],[7].

Figure 3. Pollutants and their sources [4].

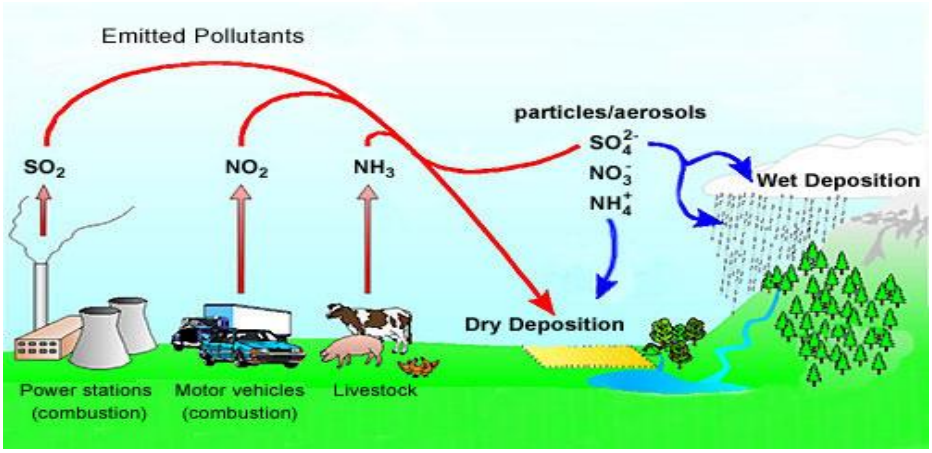

Figure 4. Origin and spreading of common air pollutants [5].

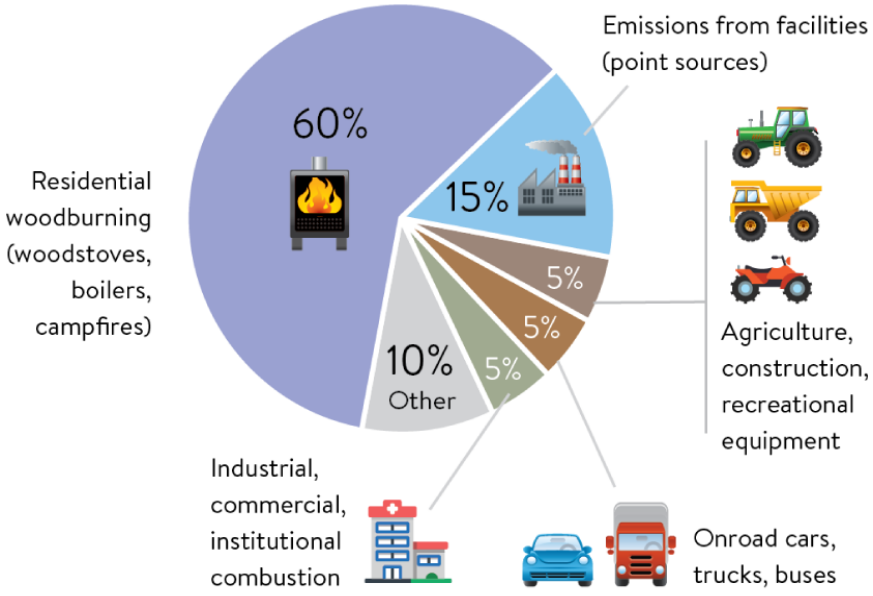

Figure 5. Distribution of the origins of fossil fuel-based pollutants [5].

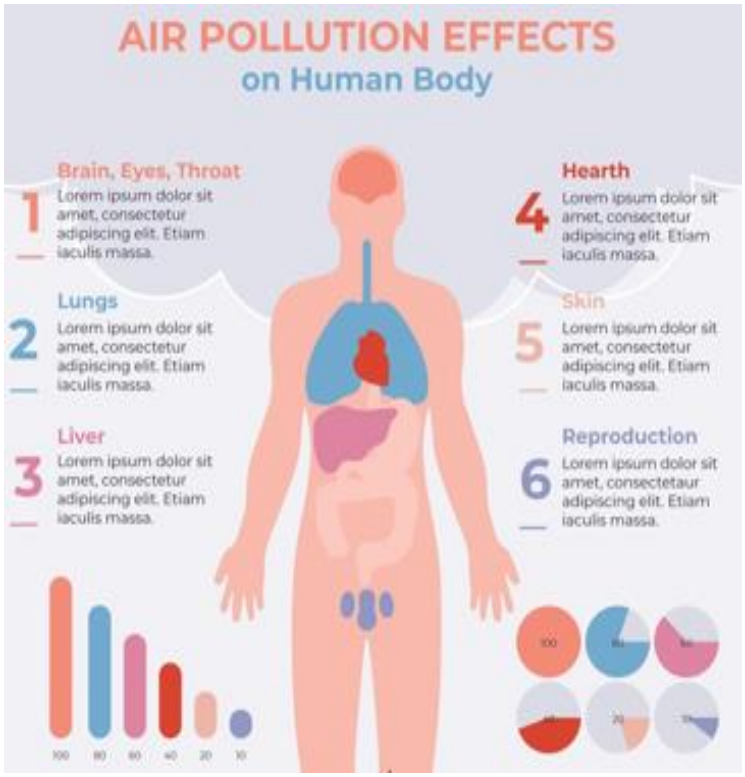

Figure 6. Typical damaging effects of air pollution on human health [7].

1.1.2. Catalytic Abatement of CO Emissions

CO releases to the atmosphere as a result of the partial oxidation of carbon-containing compounds. The main source of CO emissions is the transportation sector (Tables 1-2). Thus, the oxidation of poisonous CO to nonpoisonous CO_2 at low temperatures is essentially important. Furthermore, low-temperature CO oxidation is critical in reducing emissions during an internal combustion engine's cold start [8].

Table 1. Composition of CO in dry atmosphere, by volume [8].

Concentration	Source
0.1 ppmv	Normal atmosphere level (MOPITT)
0.5–5 ppmv	Average level in homes
5–15 ppmv	Near-properly used to gas stoves in homes, modern automobile emissions
5000 ppmv	Exhaust from a residence wood fire
7000 ppmv	Undiluted warm car exhaust without a catalytic converter

ppmv: parts per million by volume.
MOPITT: measurement of pollution in the troposphere.

Table 2. CO emission limits for various vehicles in different countries in 2018 [8].

Vehicle Type	India (gm/Km)	U.S. (gm/Km)	Canada(gm/Km)	China (gm/Km)	Europe (gm/Km)	Japan (gm/Km)
Two wheelers	0.5	0.40	1.42	0.75	0.80	1.36
Four wheelers (Petrol engine)	1.25	1.0	2.11	2.1	1.22	2.0
Four wheelers (Diesel engine)	1.00	0.5	1.50	1.50	0.70	1.60
Six wheelers (Petrol engine)	2.20	2.60	2.20	2.0	2.20	2.20
Six wheelers (Diesel engine)	2.20	2.40	2.00	2.0	1.0	2.00

In catalytic air pollution aftertreatment systems, the primary aim is to convert hydrocarbons (HC) and CO in the exhaust to CO_2, and H_2O, and to reduce NO_x to N_2 [9]. Some of the other relevant pollutants in the engine emission tail pipe systems are given in Table 3. The catalytic converter system typically consists of a ceramic honeycomb structure, or a monolith located in the exhaust stream [9].

Table 3. Typical exhaust gas Composition [9].

Component	Concentration	Component	Concentration
CO	100–1000 ppm	Ammonia	2.0 mg/mile
CO_2	2–12 vol%	Aldehydes	0.0 mg/mile
HC	50–500 ppm	Benzene	6.0 mg/mile
NO_X	30–1000 ppm	Cyanides	1.0 mg/mile
PM (Soot)	20–200 mg/m^3	PAH	0.3 mg/mile
SO_X	2–7 ppm	Toluene	2.0 mg/mile

Some of the basic overall reactions that are simultaneously carried out by a typical catalytic converter system are given below [10]:

$$2\ NO_x + CO + HC \rightarrow CO_2 + H_2O + N_2 \quad (1)$$

$$2\ CO + O_2 \rightarrow 2\ CO_2 \quad (2)$$

$$C_nH_{(2n+2)} + (3n + 1)/2\ O_2 \rightarrow n\ CO_2 + (n+1)\ H_2O \quad (3)$$

When a fossil fuel engine first starts up, both the engine and the catalyst are typically cold. The high-temperature combustion reaction from the engine begins to warm the exhaust piping. Finally, when the catalyst is heated to the critical temperature (i.e., light off temperature) catalytic action is initiated depending on the catalyst type, feed composition and their associated kinetics. [10].

1.1.3. CO Adsorption on Catalytic Active Sites

CO can poison the catalyst and block the active metal sites by strongly binding to the active metal centers. Traditionally, Pt has been the most frequently used and the most effective catalyst for catalytic CO oxidation [11-14]. DFT calculations revealed that adsorption energy of CO increases with the increasing energy of the d-band center of the metal with respect to the Fermi level [12]. Some of the transition metals are evaluated for their catalytic activity in CO oxidation reaction as a function of the position of their d-band centers. The correlation between them established the order in the CO oxidation activity as follows: Ag < Au < Ru≈ Pd < Rh < Pt [13].

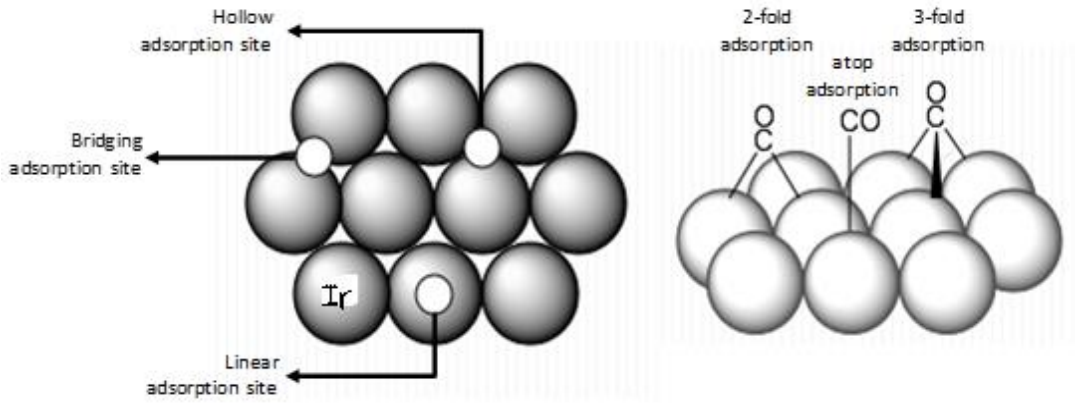

Figure 7. Typical adsorption geometries of CO on a face-centered-cubic (FCC) (111) surface (e.g. Pt(111), Pd(111), Ir(111) etc.) [12].

There are several different geometries that a metal-adsorbate pair can acquire depending on factors such as available sites, electronic structure and adsorbate coverage (Figure 8).

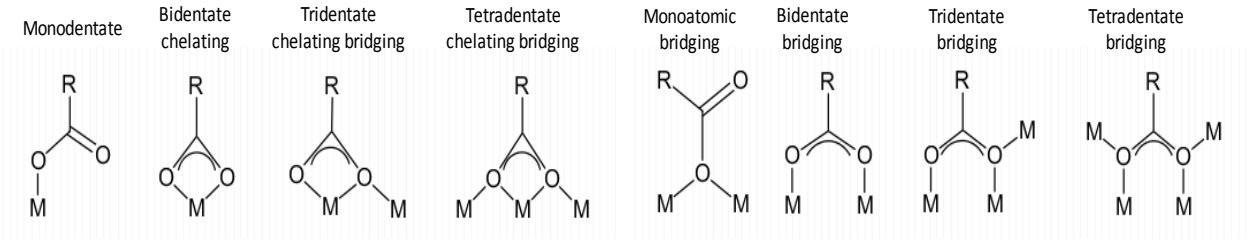

Figure 8. Possible ways of adsorption of an adsorbate onto a metal surface with various geometries [35].

The dependence of the catalytic activity and performance on the surface structure is not straightforward; electronic properties as well as structural features of the active metal nano particles (NPs) affect the rate determining step of the reaction.

The vibrational frequency of the CO molecule changes in accordance with the coordination number of the adsorbed CO molecule. With the increasing electron density of the d-orbitals of a PGM atom (e.g., Ir), electron back-donation from PGM atom to CO anti-bonding orbital π^* increases and consequently bond order of CO decreases (Figure 9). The vibrational frequency of a classical harmonic oscillator is expressed as follows:

$$V = \frac{1}{2\pi}\left(\frac{k}{\mu}\right)^{1/2} \qquad (4)$$

μ is the reduced mass and k is the force constant of the oscillator where the latter is directly proportional to bond order of the oscillator. A decrease in the bond order implies the weakening of the bond strength as well as the decreasing of the force constant along with the decreasing of the vibrational frequency of the adsorbed CO molecule. Typical vibrational frequencies of atop, 2-fold and 3-fold adsorbed CO on PGM adsorption sites are in the range of 2100-1900 cm^{-1}, 1900-1800 cm^{-1}, 1800-1700 cm^{-1} respectively [14].

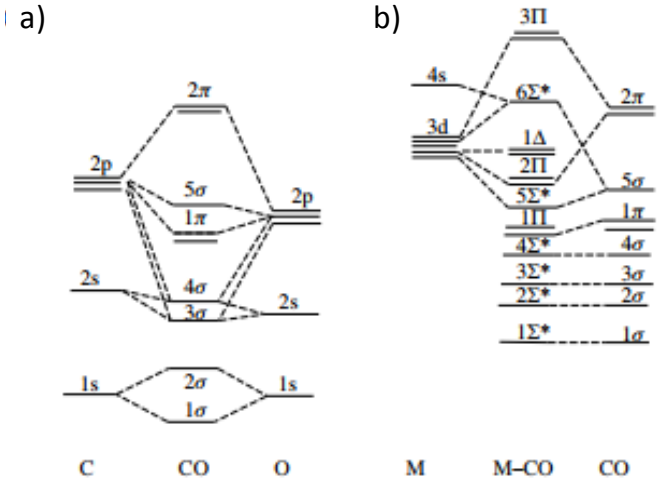

Figure 9. Molecular orbitals of (a) gas phase (free) CO and (b) linear M-CO adsorption system [14].

1.2 CO OXIDATION

The CO oxidation reaction, $CO + ½ O_2 \rightarrow CO_2$ (5), often serves as a prototypical reaction in heterogeneous catalysis. [15]. Basic information about this reaction is provided in the forthcoming sections.

1.2.1 Heterogeneous Catalysts for CO Oxidation

The catalytic conversion of CO at lower temperatures has received significant attention due to its relevance to mining, deep sea diving, space investigation, CO sensors and CO_2 lasers [16-19]. The CO oxidation has also applications in large scale chemical processes such as water–gas shift reaction and production of methanol [20]. At lower temperatures, catalytic oxidation of CO is

difficult due to the strong CO adsorption on the PGM active sites and self-poisoning of the catalyst as a result of the accumulation of CO on the catalyst surface [21-23].

Commercially available CO oxidation catalysts fall into three categories:

1. Noble metal catalysts

2. Transition metal catalysts

3. Mixed metal oxide catalysts

Various transition metals (e.g., Cu, Mn, Co, Cr, Ni, Fe, etc.), noble metals (e.g., Pt, Pd, Rh, Au, etc.), and metal oxides (e.g., Cu_2O, CeO_2, ZnO, ZrO_2, TiO_2, etc.) have been widely used as catalysts for CO oxidation. Particularly, precious PGM sites have been reported to reveal high catalytic activity and stability as a function of reaction temperature [24-27].

1.2.1.1 Noble Metal Catalysts

Pt, Rh, Ru, Ag, Pd, Ir, and Au, are noble metals which are commonly utilized in catalytic converter applications. Rh is typically used as a NO_x reduction catalyst and Pd is utilized as a CO/NO/HC oxidation catalyst, whereas Pt can act as both as a NO_x reduction and a CO/HC oxidation catalyst [25-27]. Au was reported to exhibit good performance in low-temperature CO oxidation upon its deposition on reducible metal oxides [28]. Au supported on reducible oxides is known to catalyze the CO oxidation efficiently even below 0 °C). Pt/SnO_2 and Pd/SnO_2 catalysts have been widely used for ambient temperature oxidation of CO [29]. The catalytic performance of PtO_x, PdO_x, RhO_x, and RuO_x is strongly influenced by the oxygen coordination on the PGM sites where the oxidized noble-metal catalyst has been indeed more active than the completely reduced PGM particles [30]. Noble metal catalysts are less preferable due to their high-cost and lower availability. While most noble metal catalysts are moisture tolerant, they generally require high temperatures (i.e., above 100 °C) for efficient operation [26]

1.2.2 Kinetics of the Catalytic CO Oxidation Reaction

Catalytic CO oxidation reaction on noble metals takes place through mostly Langmuir-Hinshelwood mechanism [31]. Kinetic rate order of the reaction with respect to each reactant depends on several parameters such as the catalyst type, temperature, total pressure, relative concentrations of reactants, and the presence of other external species (e.g., water) etc. [32]

According to Figure 10, since CO can adsorb on the catalyst surface stronger than O_2 molecule, at low temperatures surface will be covered by CO molecules leading to CO poisoning. Consequently, rate order of the reaction with respect to CO will be negative, while its rate order with respect to O_2 will be positive. This fact shows that any further increase in CO pressure will decrease the rate of the reaction as a result of blocking of the active sites by CO molecules. At high temperatures, residence time of species on the surface will be short and they will desorb quickly from the surface. Furthermore, activation of the O_2 molecule by O=O cleavage to form atomic O species active in the oxidation mechanism is facilitated at elevated temperatures. As a result, increase in pressure of reactants can increase the rate of the reaction, since the orders of the reaction with respect to these species are positive and there exists sufficient number of active sites available on the surface. [32].

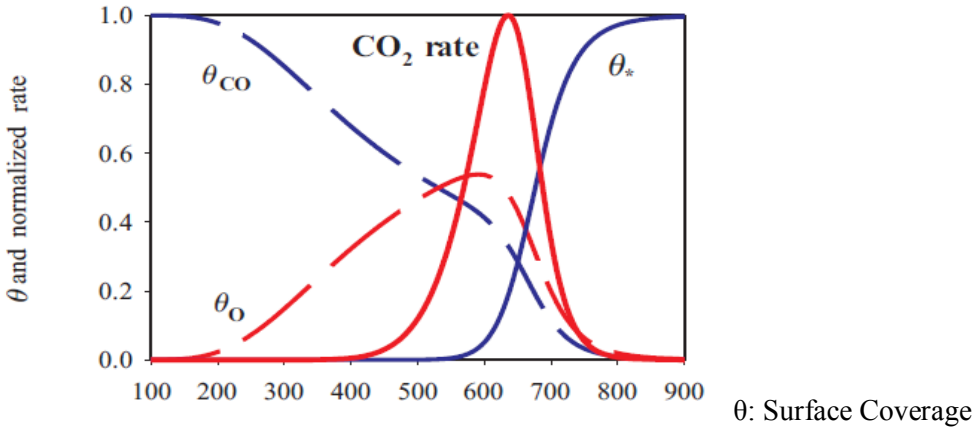

Figure 10. Surface coverage of CO (θ_{CO}) and O (θ_O) species and the CO_2 formation rate as a function of temperature in a typical CO oxidation reaction following Langmuir-Hinshelwood kinetics [32].

1.3 Surface Free Energy

The work that needs to be spent to increase the surface area of a material is defined as the surface free energy (γ). The relation between the surface free energy as a function of the geometric distribution of atoms in a PGM nanoparticle can be described using the so called Wulff construction [33]. In this approach, the surface free energy is considered to be proportional to the length of the vector originating from the center of the nanoparticle and normal to the crystal facet [33]. Principally, Wulff plot is constructed by reuniting points representing the particular surface energy of a plane in that orientation. Since the equilibrium structure will be determined by the minimum surface free energy, it is possible to reach the equilibrium shape by tangent lines perpendicular to the circular Wulff plot lines.

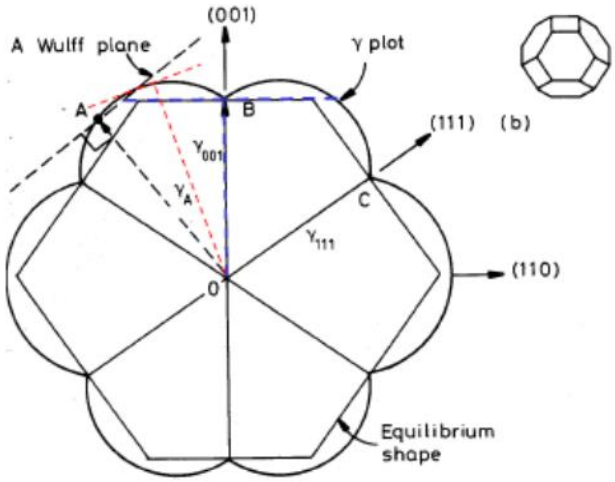

Figure 11. A simplistic way to construct Wulff plot [34].

The main driving force for the adsorption is to decrease the surface free energy of the substrate via adsorption of external molecules (e.g., CO).

1.4 Operational Parameters in CO Oxidation

There are various factors effective on the rate and yield of CO oxidation reaction. Some of these factors which have a significant influence on catalytic CO oxidation reaction given below will be discussed in more depth in this section [36-40]:

• Catalyst type

•Amount of sample

•Feed composition

•Flow rate of the reaction mixture

a) Catalyst type

Due to the low loading of the Ir active sites utilized in the current work (i.e., 0.2, 0.5, and 1 wt%), limitations in CO oxidation activity are expected. Thus, in the current work, we attempt to synthesize extremely small active centers with diameters typically less than 1 nm to take advantage of the efficiency of the low coordination of catalytic Ir centers. In addition to maximizing the number of exposed Ir sites by synthesizing small Ir clusters, we also aim to increase the catalytic activity of each particular Ir active site by obtaining unique electronic interactions between small Ir clusters and the metal oxide support [36].

b) Amount of Sample

Mass transfer and heat transfer phenomena are closely linked to the catalyst amount in the reactor. Accordingly, the amount of catalyst must be optimized to avoid mass transfer and heat transfer limitations in the reactor. Thus, sieving of the catalyst powder using a proper mesh size is necessary to obtain a homogeneous and a favorable grain size, which can avoid pressure drop in the reactor as well as heat/mass transfer limitations. It is worth mentioning that utilization of a catalytically inert diluent material is also critical. Since CO oxidation is an exothermic reaction, it is common to observe the formation of unwanted hot spots in the catalyst bed which may hinder temperature control and alter the isothermal conditions in the catalytic reactor. [37], [38].

c) Feed composition

If active sites are not exposed to sufficient number of reactants, catalytic conversion can be suppressed. On the other hand, relative concentrations of reactants (in our case CO vs O_2

concentrations in the feed) should be optimized in order to maximize the conversion and minimize catalytic poisoning effects or over oxidation of the catalyst active sites. [39].

d) Flow rate of the reaction mixture

For reasonable flow rate values, reactants can spend enough time on the catalyst surface and readily encounter each other on the active sites leading to high activity and conversion. In contrast, extremely high flow rates limit the residence time of the reactants on the catalyst surface resulting in low conversion [40].

1.5 Motivation of the Study

The main motivation of the current work is to synthesize low metal loading Ir catalysts with high PGM dispersion, exhibiting catalytic performance in CO oxidation reaction that is comparable to that of conventional PGM catalysts with higher metal loadings. Along these lines, two different synthesis methods have been applied to synthesize catalysts on four different support materials (i.e., MgO, CeO_2, La_2O_3/ZrO_2 and TiO_2/ZrO_2). Furthermore, we also investigated the effect of sample pretreatment conditions after the catalyst synthesis and utilized three different sample pre-treatment conditions (i.e., annealing in H_2, annealing in O_2, and atmospheric calcination) to analyze their influence on average particle size, reduction extent of the support, specific surface area, pore volume, pore size, and Ir oxidation state.

2. EXPERIMENTAL

2.1 SAMPLE PREPARATION

2.1.1 Preparation of Catalysts with Sub-nanometer Diameters

Upon careful investigation of the former studies in the literature regarding the synthesis of highly dispersed, small PGM clusters on metal oxide support materials [41-50], we have designed synthesis recipes which are inspired by these existing reports. As a result, we decided to use two different synthesis methods (i.e., Classical Impregnation (CI) and Incipient to Wetness Impregnation (IWI)) to synthesize various types of catalysts, and compared their structures as well as catalytic activities.

2.1.1.1 "Classical Impregnation" Synthesis Method

Figure 12 illustrates different steps and parameters applied to synthesize two family of catalysts via classical impregnation (CI) method.

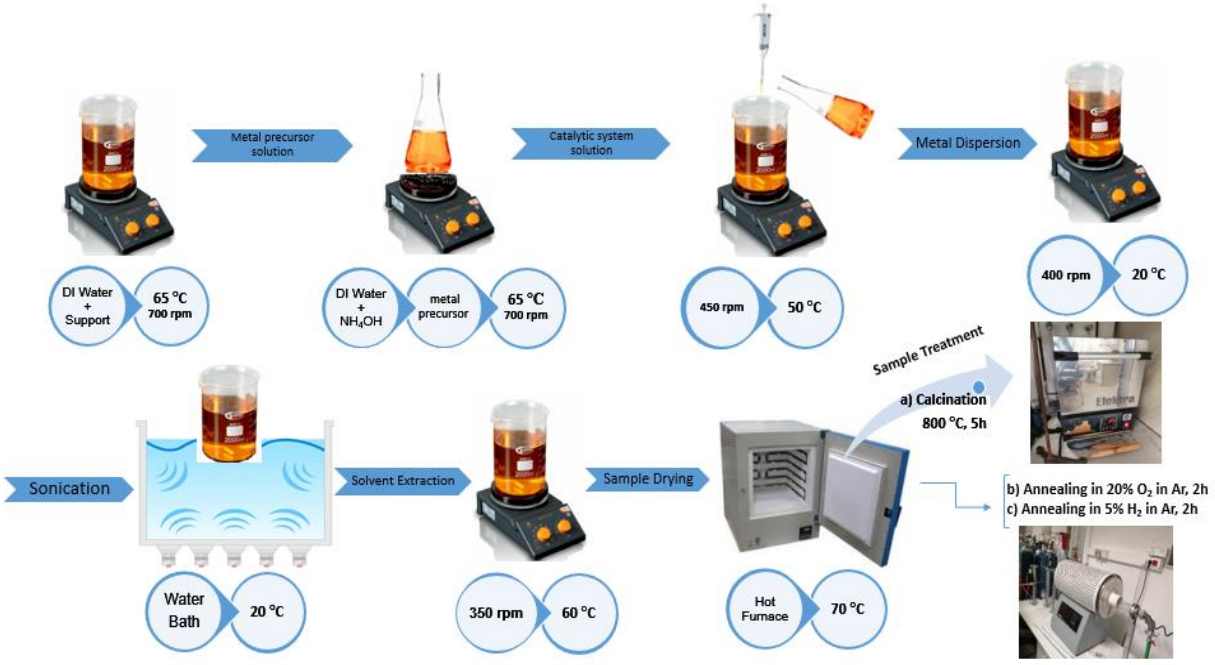

Figure 12. Schematic representation of "classical impregnation" synthesis method.

2.1.1.1.1 Synthesis of $IrCl_3$-CeO_2

For the synthesis of 0.2 and 0.5 wt% $IrCl_3$ ($IrCl_3.3H_2O$, 99.9%, Sigma Aldrich) on ceria (type A, >99%, Daiichi Kigenso Kagaku-Koyogo), classical impregnation method was followed. This method is summarized below.

0.998 g ceria (for 0.2 wt% Ir) (or 0.995 g ceria for 0.5 wt% Ir) of ceria support was mixed with deionized (DI) water to have a mixture volume of 40 ml. In the second step, 0.310 g (or 0.775 g for 0.5 wt%) metal precursor ($IrCl_3$) was weighted, then mixed with DI water to obtain a 50 ml solution. In order to fully dissolve the metal precursor, two drops of NH_4OH (99.99%, Sigma Aldrich) was added to the mixture while simultaneous heating at 65 °C and stirring with a rotation rate of 700 rpm for 20 min took place. Finally, a brownish yellow solution as metal precursor solution was obtained. Then, the metal precursor solution was added dropwise to the support solution during stirring (T: 50 °C, rotation rate: 450 rpm). Sequentially, stirring (T: 20 °C, rotation rate: 400 rpm) of the sample solution for 16 h took place. After 16 h, solution was sonicated for 1 h. To evaporate the solvent, sample solution was stirred (T: 60 °C, rotation rate: 350 rpm) for 12 h. In Tables 4-6, some of the involved parameters for aforementioned synthesis are given.

2.1.1.1.2 Synthesis of $Ir(acac)_3$-CeO_2

Acetylacetonate (acac, ($C_5H_8O_2$)) is the metal precursor which is used to synthesize second catalytic family in this work. 1.98 g ceria (for 0.2 wt% Ir) (or 1.95 g ceria for 0.5 wt% Ir) ceria support (type A, >99%, Daiichi Kigenso Kagaku-Koyogo) was mixed with 30 ml n-pentane (>99%, Sigma Aldrich) as solvent. To prepare metal precursor solution, 0.010 g (or 0.025 g for 0.5 wt%) $Ir(acac)_3$ (97%, Sigma Aldrich) was mixed with 20 ml solvent (n-pentane) while simultaneous heating at 65 °C and stirring with a rotation rate of 700 rpm for 20 min took place. Then, the metal precursor solution was added dropwise to the support solution during stirring (T: 50 °C, rotation rate: 450 rpm). Sequentially, stirring (T: 20 °C, rotation rate: 400 rpm) of the sample solution for 16 h took place. To evacuate the remained solvent, sonication under vacuum for 1 h was applied.

2.1.1.1.3 Synthesis of $Ir(acac)_3$-MgO

1.98 g MgO (for 0.2 wt% Ir) (or 1.95 g MgO for 0.5 wt% Ir) support (99.99%, Daiichi Kigenso Kagaku-Koyogo) was mixed with 30 ml n-pentane (>99%, Sigma Aldrich) as solvent. To prepare metal precursor solution, 0.010 g (or 0.025 g for 0.5 wt%) $Ir(acac)_3$ (97%, Sigma Aldrich) was mixed with 20 ml solvent (n-pentane) while simultaneous heating at 65 °C and stirring with a rotation rate of 700 rpm for 20 min took place. Then, the metal precursor solution was added dropwise to the support solution during stirring (T: 50 °C, rotation rate: 450 rpm). Sequentially, stirring (T: 20 °C, rotation rate: 400 rpm) of the sample solution for 16 h took place. To evacuate the remained solvent, sonication under vacuum for 1 h was applied.

Finally, all the synthesized samples after drying at 70 °C for 20 h in an atmospheric furnace, have gone through different types of treatments. Annealing in O_2 (20% O_2 in Ar, flow rate: 100 ml/min) at 500 °C, annealing in H_2 (5% H_2 in Ar, flow rate: 100 ml/min) at 500 °C and calcination up to 800 °C in atmosphere are three different types of treatments that have been used.

Table 4. Various parameters regarding the synthesis of the catalysts via "classical impregnation" method.

Catalyst	**Metal Precursor**	**Support**	**Ir wt.%**	**Nominal Total Catalyst Mass**	**Solvent**
$IrCl_3$-CeO_2	$IrCl_3$	CeO_2	0.2	1 g sample (0.998 g support+ 0.31 g precursor)	DI Water (H_2O)
$IrCl_3$-CeO_2	$IrCl_3$	CeO_2	0.5	1 g sample (0.995 g support+ 0.775 g precursor)	DI Water (H_2O)
Ir(acac)-CeO_2	Ir(acac)	CeO_2	0.2	2 g sample (1.98 g support+ 0.010 g precursor)	n-Pentane (C_5H_{12})
Ir(acac)-CeO_2	Ir(acac)	CeO_2	0.5	2 g sample (1.95 g support+ 0.025 g precursor)	n-Pentane (C_5H_{12})

Ir(acac)-MgO	Ir(acac)	MgO	0.2	2 g sample (1.98 g support+ 0.010 g precursor)	n-Pentane (C_5H_{12})
Ir(acac)-MgO	Ir(acac)	MgO	0.5	2 g sample (1.95 g support+ 0.025 g precursor)	n-Pentane (C_5H_{12})

Table 5. Solution details regarding the synthesis of the catalysts via "classical impregnation" method.

Solution Stirring Rate (rpm)	Solution Stirring Overall Time (h)	Solution Stirring Temperature (C)	Solvent Extraction stirring rate (rpm) Stirring Rate (rpm)	Solvent Extraction Overall Time (h)	Solvent Extraction Temperature (C) Temperature (°C)	Sonication Time (h)	Sonicator Temperature (C)	Vacuum Pressure (mmHg) (Air Exclusion)
400	16	20	350	12	60	1	30	200

Table 6. Pretreatment parameters used in the sample preparation.

Treatment Type	**Gas Concentration**	**Temperature (C)**	**Flow Rate (ml/min)**	**Heating Ramp (°C/min)**	**Treatment Overall Time (h)**
Calcination		800		120	5
Annealing in O_2	20% in Ar	500	100	75	2
Annealing in H_2	5% in Ar	500	100	75	2

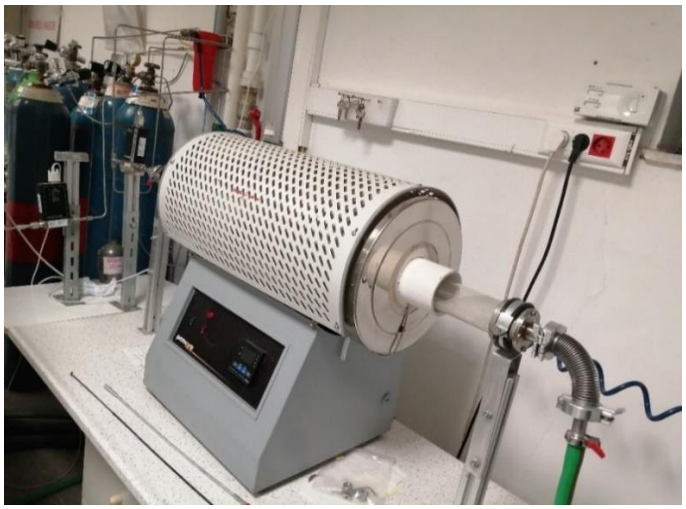

Figure 13. Tube furnace used in the pretreatment protocols.

Figure 14. Muffle furnace used in the calcination step of the pretreatment protocols.

2.1.1.2. "Incipient to Wetness Impregnation" Synthesis Method

2.1.1.2.1 "Incipient to Wetness Impregnation" in General

A technique for creating heterogeneous catalysts is incipient to wetness impregnation , also known as capillary impregnation or dry impregnation. In this technique, the metal precursor is dissolved in solution (organic or aqueous), and the resulting metal-containing solution is dispersed on a support with the same pore volume as the added solution. The solution is drawn into the pores by capillary action [51].

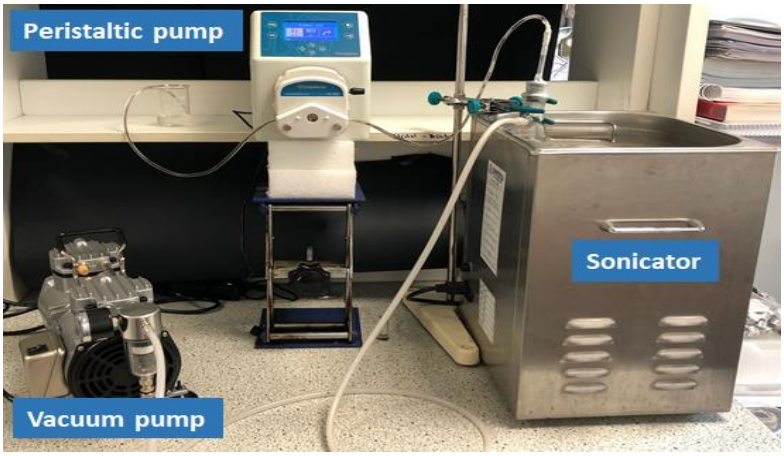

Figure 15. "Incipient to wetness impregnation" set-up.

The support material was weighed in the vacuum flask and then the bottom surface of the flask was placed into the sonicator. One end of the vacuum flask was connected to the vacuum pump and the other end was connected to the hose of the peristaltic pump using a glass pipette. One of the three cylinders of the peristaltic pump was adjusted to be upward, so that air contact was prevented. After the installation, the vacuum pump which was brought to the lowest speed (to achieve a pressure of 400 mmHg) was turned-on and then the sonicator was switched on. The support material was kept under vacuum for 45 min in order to evacuate the pores of the material and to desorb water/adsorbates in the pores. Figure 16 illustrates different steps and parameters applied to synthesize three family of catalysts via incipient to wetness impregnation method (IWI).

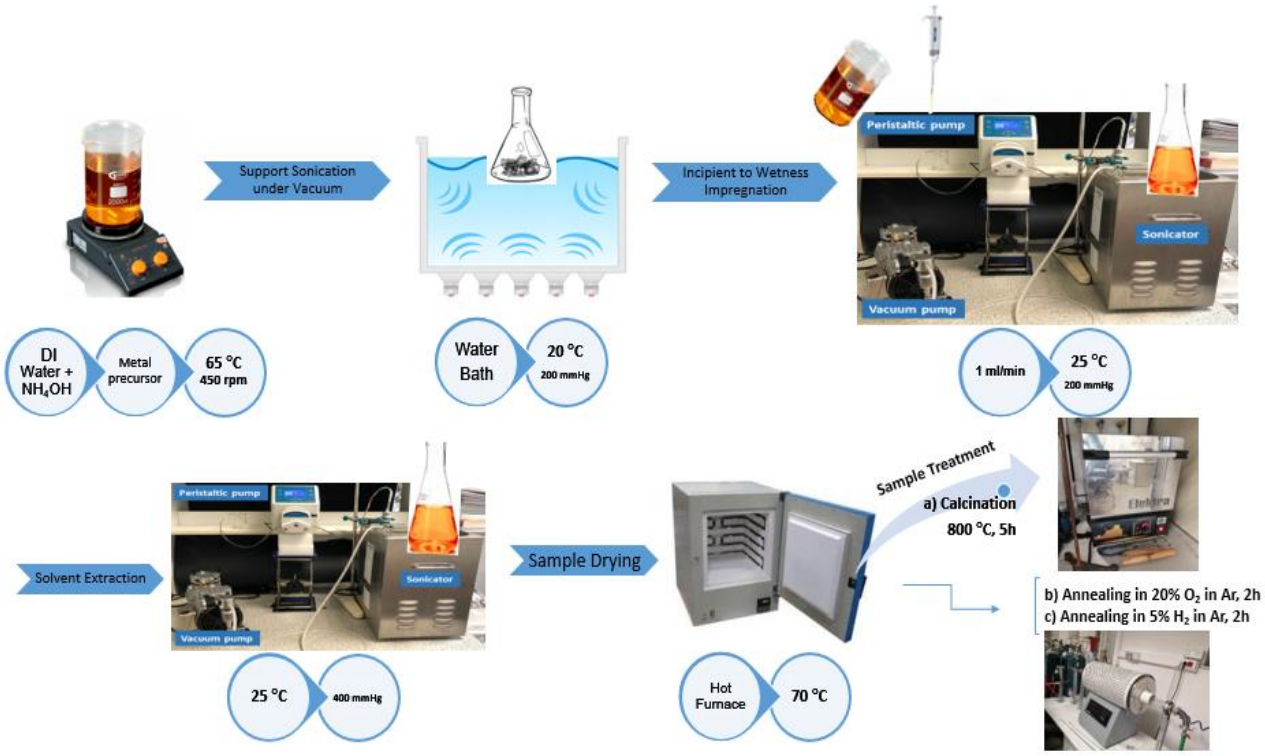

Figure 16. Schematic representation of "incipient to wetness impregnation" synthesis method.

2.1.1.2.2 Synthesis of $IrCl_3$-CeO_2

For sample with 0.2 wt% metal loading, sample solution was prepared with 5 ml ammonia (99.99%, Sigma Aldrich), 8 ml DI water, 93 mg $IrCl_3$ ($IrCl_3.3H_2O$, 99.9%, Sigma Aldrich), and 2.98 g support (ceria type A, >99%, Daiichi Kigenso Kagaku-Koyogo). Solution composition for 0.5 wt% metal loading sample was 5 ml ammonia, 8 ml DI water, 232.5 mg metal precursor, and 2.95 g support, and composition for 1 wt% metal loading sample was 5 ml ammonia, 8 ml DI water, 465 mg metal precursor, and 2.90 g support. After solution was ready and support was sonicated for 45 min under vacuum, 13 ml precursor solution was added into the support dropwise in sonication mode under 200 mmHg vacuum. Then, solvent extraction for 2 h under 400 mmHg vacuum while sonicator was running took place. All the synthesized samples were dried for 20 h at 70 °C, and treatments of the samples (calcination, annealing in O_2 and H_2) took place as the last step. Some of the involved parameters are mentioned in Tables 7-9 in detail.

2.1.1.2.3 Synthesis of $IrCl_3$- La_2O_3/ZrO_2

For sample with 0.2 wt% metal loading, sample solution included 10 ml ammonia, 14 ml DI water, 93 mg $IrCl_3$, and 2.98 g support (9%La_2O_3/ZrO_2, >99%, Daiichi Kigenso Kagaku-Koyogo) Composition of the solution for 0.5 wt% metal loading sample was 10 ml ammonia, 14 ml DI water, 232.5 mg metal precursor, and 2.95 g support, and composition for 1 wt% metal loading sample was 10 ml ammonia, 14 ml DI water, 465 mg metal precursor, and 2.90 g support. After solution was ready and support was sonicated for 45 min under vacuum, 24 ml precursor solution was added into the support dropwise in sonication mode under 200 mmHg vacuum. Then, solvent extraction for 2 h under 400 mmHg vacuum while sonicator was running took place. All the synthesized samples were dried for 20 h at 70 °C, and treatments of the samples (calcination, annealing in O_2 and H_2) took place as the last step.

2.1.1.2.4 Synthesis of $IrCl_3$-TiO_2/ ZrO_2

For sample with 0.2 wt% metal loading, sample solution included 12 ml ammonia, 15 ml DI water, 93 mg $IrCl_3$, and 2.98 g support (30%TiO_2/ZrO_2, >99%, Daiichi Kigenso Kagaku-Koyogo) Composition for 0.5 wt% metal loading sample was 12 ml ammonia, 15 ml DI water, 232.5 mg metal precursor, and 2.95 g support, and composition for 1 wt% metal loading sample was 12 ml ammonia, 15 ml DI water, 465 mg metal precursor, and 2.90 g support). After solution was ready and support was sonicated for 45 min under vacuum, 27 ml precursor solution was added into the support dropwise in sonication mode under 200 mmHg vacuum. Then, solvent extraction for 2 h under 400 mmHg vacuum while sonicator was running took place. All the synthesized samples were dried for 20 h at 70 °C, and treatments of the samples (calcination, annealing in O_2 and H_2) took place as the last step.

Table 7. Various parameters regarding the synthesis of the catalysts via "incipient to wetness impregnation" method.

Catalyst	Metal Precursor	Support	Ir wt.%	Nominal Total Catalyst Mass	Solvent
$IrCl_3$-CeO_2	$IrCl_3$	CeO_2	0.2	3 g sample (2.98 g support+ 93 mg precursor)	DI Water+ NH_4OH
$IrCl_3$-CeO_2	$IrCl_3$	CeO_2	0.5	3 g sample (2.95 g support+ 232.5 mg precursor)	DI Water+ NH_4OH
$IrCl_3$-CeO_2	$IrCl_3$	CeO_2	1	3 g sample (2.98 g support+ 465 mg precursor	DI Water+ NH_4OH
$IrCl_3$-La_2O_3/ZrO_2	$IrCl_3$	La_2O_3/ZrO_2	0.2	3 g sample (2.98 g support+ 93 mg precursor)	DI Water+ NH_4OH
$IrCl_3$-La_2O_3/ZrO_2	$IrCl_3$	La_2O_3/ZrO_2	0.5	3 g sample (2.95 g support+ 232.5 mg precursor)	DI Water+ NH_4OH
$IrCl_3$-La_2O_3/ZrO_2	$IrCl_3$	La_2O_3/ZrO_2	1	3 g sample (2.98 g support+ 465 mg precursor	DI Water+ NH_4OH
$IrCl_3$-TiO_2/ ZrO_2	$IrCl_3$	TiO_2/ ZrO_2	0.2	3 g sample (2.98 g support+ 93 mg precursor)	DI Water+ NH_4OH
$IrCl_3$- TiO_2/ ZrO_2	$IrCl_3$	TiO_2/ ZrO_2	0.5	3 g sample (2.95 g support+ 232.5 mg precursor)	DI Water+ NH_4OH
$IrCl_3$- TiO_2/ ZrO_2	$IrCl_3$	TiO_2/ ZrO_2	1	3 g sample (2.98 g support+ 465 mg precursor	DI Water+ NH_4OH

Table 8. Incipient to wetness impregnation set-up parameters.

Drop casting Rate (drop/min)	Drop casting Overall Time (min)	Vacuum Range (mmHg)	Sonication Overall Time (min)	Sonicator Temperature (C)
1	13-27	200-400	45-120	30

Table 9. Pretreatment parameters used in the sample preparation.

Treatment Type	Gas Concentration	Temperature (C)	Flow Rate (ml/min)	Heating Ramp (°C/min)	Treatment Overall Time (h)
Calcination		800		120	5
Annealing in O_2	20% in Ar	500	100	75	2
Annealing in H_2	5% in Ar	500	100	75	2

2.2 In-situ FTIR

FTIR spectroscopic measurements were carried out in transmission mode in a batch-type catalytic reactor coupled to an FTIR spectrometer (Bruker Tensor 27) and a Quadruple Mass Spectrometer (QMS) (Stanford Research System, RGA 200) for Temperature-Programmed Desorption (TPD) and residual gas analysis (RGA). A Hg-Cd-Te (MCT) detector was used to record FTIR spectra, with 128 scans for acquiring each spectrum and spectral resolution of 4 cm^{-1} (Figure 17). The samples were mounted into the stainless-steel IR cell equipped with optically-polished BaF_2 windows. This IR cell was connected to a gas manifold (including a dual-stage rotary vane pump and two turbomolecular pumps) so that the pressure in the cell could be varied within $1000\text{-}10^{-6}$ Torr. About 30 mg of finely ground powder sample was pressed onto a high-transmittance, lithographically etched tungsten grid which was mounted on a copper sample holder assembly, attached to a ceramic vacuum feed through. A K-type thermocouple was spot-welded to the surface of a thin tantalum plate attached on the W-grid to monitor the sample temperature. The sample

temperature was controlled within 298 K-1100 K via a computer-controlled DC resistive heating system using the voltage feedback from the thermocouple.

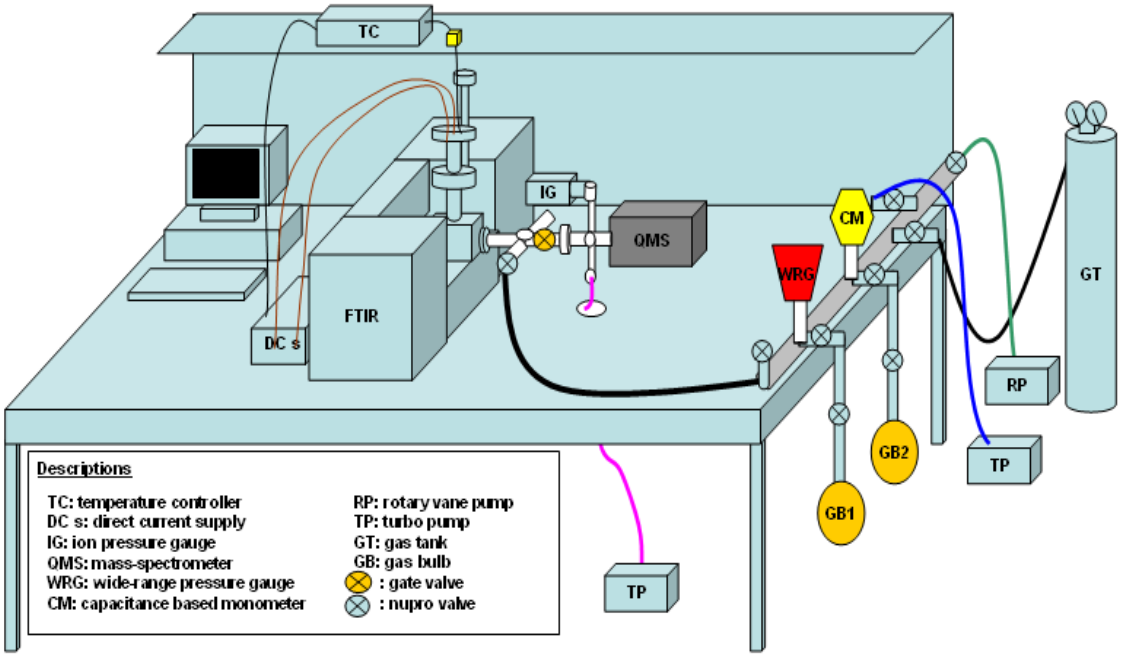

Figure 17. Simplified schematic of the custom-designed in situ-FTIR catalytic analysis system coupled to the quadrupole mass spectrometer chamber. (Courtesy of Emine Kayhan/Ozensoy Research Group)

2.2.1 In-situ FTIR Experiment: CO Adsorption

Before the in-situ FTIR spectroscopic experiments, pre-treated catalyst sample was annealed in vacuum (10^{-3} Torr) at 450 °C to clean the surface of the catalyst surface, the reactor walls and IR optics from impurities such as carbonaceous species and water molecules Then, the sample was cooled to 60 °C, and 20 Torr of CO (Air Products, >99.995%) was dosed onto the catalyst for 30 min. Afterwards, CO was pumped out from the in-situ cell and FTIR spectra were acquired.

2.3 XRD

X-ray diffraction (XRD) patterns of the catalysts were obtained by using a Pananalytical Multi-Purpose X-Ray Diffractometer (XRD-MPD) equipped with a Cu Kα (1.5405 Å) X-Ray source operating at 45 kV/40 mA). Finely ground catalyst sample (Figure 18) was placed on a silicon

single crystal wafer as shown in Figure 19 and then placed into the diffractometer. Other XRD parameters used in the data acquisition are given in Table 10.

Table 10. XRD data acquisition parameters used in the measurements.

Parameter	Value
Range	80
2Theta	50
Offset	0
Step size	0.01
Time per step	30

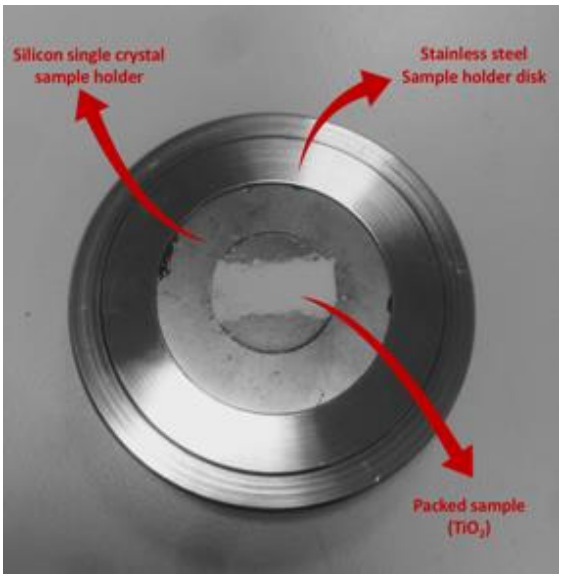

Figure 18. Catalyst powder sample loading for XRD-MPD measurements on a silicon single crystal.

2.4 XPS

Thermo Scientific K-Alpha X-ray photoelectron spectrometer (ESCALAB 250) was used to record the XPS spectra. Monochromatic Al K_α radiation (1486.6 eV) was used to stimulate

photoemission. A pass energy of 200 eV was used for survey scans while high-resolution scans were performed with a 30 eV pass energy. C1s binding energy was set at 284.8 eV for the calibration of the binding energies (B.E.). Number of scans were 2 and 20 for the survey and high-resolution spectra, respectively. Thermo Avantage software was used in spectra analysis, where smart background was used for background subtraction.

2.5 Raman Spectroscopy

Raman spectra were recorded on a WiTec alpha 300 RS instrument, equipped with a confocal Raman BX41 microscope, spectrograph with an 800 mm focal length and a nitrogen cooled CCD detector. The Raman spectrometer was equipped with a Nd:YAG laser (λ = 532.1nm). During the Raman experiments, the laser power was tuned to 20 mW, measured at the sample position, in order to minimize the sample heating effects. The incident light source was dispersed by holographic grating with a 600 grooves/mm and focused onto the sample by using a 50X objective. The confocal hole and the slit entrance were set at 1100 μm and 200 μm, respectively. The spectrometer was regularly calibrated by adjusting the zero-order position of the grating and comparing the measured Si Raman band frequency with the typical reference value of 520.7 cm^{-1}. The powder samples were mechanically dispersed onto a single-crystal Si holder for the Raman measurements and all Raman spectra were acquired within 100-4000 cm^{-1} with an acquisition time of 213 s and a spectral resolution of 4 cm^{-1}.

2.6 BET

Micromeritics ASAP 2000 gas sorption and porosimetry system was employed for the specific surface area (SSA, m^2/g), pore volume (cm^3/g), and pore size (Å) measurements using the twelve-point Brunauer-Emmett-Teller (BET) method. In order to remove physisorbed species on the powder catalyst, samples were initially pretreated under vacuum first at room temperature (RT) for 1 h then at 200 ^oC for 5 h to eliminate water.

2.7 TEM-EDX

FEI Technai G2F30 transmission electron microscope (TEM) was used to carry out TEM and energy dispersive X-ray (EDX) measurements. The powdered catalysts were dispersed and

sonicated in ethanol, followed by drop casting the mixture on carbon-coated copper grids. TEM imaging was carried out in bright-field (BF) conditions.

2.8 Flow-mode Catalytic Test Reactor

The activities of the catalysts in CO oxidation were measured within a temperature range of 25–400 °C with different heating ramps (2, 4 and 8 C/min) under a total pressure of 1 bar. A plug flow reactor (continuous tubular fixed-bed reactor with a 0.8 cm diameter, and quartz wool bed with 40 mg weight) equipped with a SRS RGA 200 QMS was used to perform the flow mode CO oxidation catalytic performance tests (Figure 19). The reactant gas feed contained 1% CO, 10% O_2 with Ar as the balance gas. In each catalytic CO oxidation test, 100 mg of the catalyst was mixed with 300 mg 100-120 mesh α-Al_2O_3 diluent, which served as a filler for better temperature control in the catalytic bed and to preserve isothermal conditions during the catalytic performance tests. A K-type thermocouple inserted in a custom designed quartz rod was placed in the middle of the catalytic bed to monitor the reaction temperature. The following gas mixtures and gases (all supplied by Linde) were used: Argon (Ar) (>99.99% purity), 2% CO in Ar (CO purity >99.99%), Oxygen (O_2) (>99.99% purity), Hydrogen (H_2) (>99.99% purity). For all CO oxidation reactions, the total flow rate was 500 ml.STP.min^{-1} (for the High Flow Rate (HFR) procedure) and 200 ml/min (for the Moderate Flow Rate (MFR) procedure), and the total catalyst and filler volume was 0.5 ml.

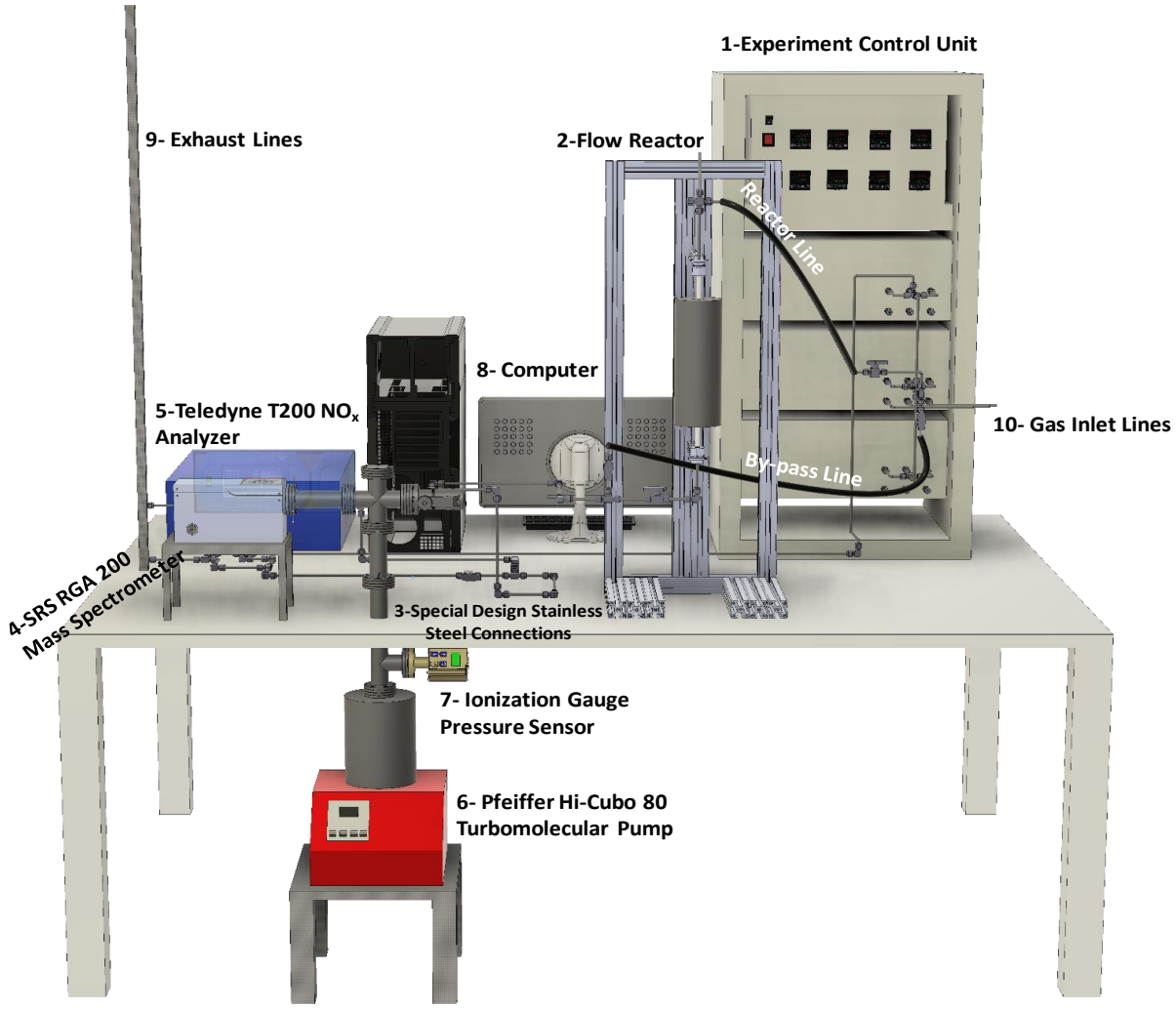

Figure 19. Reaction setup for the catalytic carbon monoxide (CO) oxidation. (Courtesy of Kerem E. Ercan/Ozensoy Research Group)

The Weight Hourly Space Velocity (WHSV) and the Gas Hourly Space Velocity (GHSV) parameters used in the catalytic CO oxidation tests were 300 000 $cm^3.STP.g^{-1}.h^{-1}$ (3.87 g/h. cm^3. $g_{catalyst}$) and 270 000 h^{-1}, respectively (for the first procedure with the higher flow rate)), 120000 $cm^3.STP.g^{-1}.h^{-1}$ (1.55 g/h. cm^3. $g_{catalyst}$) and 110000 1/h, respectively (for the second procedure with the moderate flow rate). The percentage of converted CO was calculated using the equation (5) where $(CO)_{in}$ and $(CO)_{out}$ stand for the CO concentrations in the inlet and the outlet of the reactor:

$$CO\ \%\ conversion = \left|\frac{(CO)_{in}-(CO)_{out}}{(CO)_{in}}\right| X\ 100 \qquad (5)$$

3. RESULTS AND DISCUSSION

3.1. Functional Characterization

3.1.1 Flow-mode Catalytic CO Oxidation Reaction Measurements

Before running the flow reactor catalytic tests, the following experimental points were carefully considered:

•**Sieving the Samples:** samples were sieved with proper mesh sizes before the experiments in order to minimize pressure drop as well as heat/mass transfer limitations in the reactor during catalytic performance tests. All the samples and diluent were sieved with mesh size between 100-120 μm.

•**Effect of Diluent:** Mixing the sample with a proper diluent is critical to prevent the formation of hot spots in the catalyst bed during the exothermic CO oxidation reaction [52]. Alpha-alumina was used as a catalytically inert diluent material in all activity measurements.

•**Sample Weight:** Our control experiments showed that 100 mg is a suitable catalyst mass to avoid pressure drop, heat and mass transfer limitations.

•**Feed ratio:** Based on former kinetic data [32], [53], a $CO:O_2$ ratio of 1:10 ratio was used in the reaction feed to enable complete oxidation of CO with excess O_2.

•**Flow Rate:** Two different total reactant gas mixture flow rates (i.e., 500 and 200 ml/min) were utilized in the current work in order to investigate the influence of the WHSV and GHSV and also indirectly the corresponding reactant residence times on the catalytic reactivity. Lower flow rates are expected to yield higher reactant residence times on the catalyst surface resulting in higher conversion at the expense of slower reaction rates.

•**Sample Pre-treatment (Reduction):** Reducing of the samples under hydrogen-rich environment (5% H_2 in Ar, flow rate: 200/500 ml/min, t: 60 min) was carried out in order to expose more active sites with lower oxidation states and coordination numbers.

•**Temperature range:** Catalytic activity tests were executed within 25 –500 °C. This temperature range was sufficient to observe 100% CO conversion for all of the investigated catalysts.

•**Reactant Gas Mixture Total Pressure:** all the experiments were carried out under 1 bar constant pressure.

Catalytic CO oxidation procedure for the higher flow rate (HFR):

Step 1. Reduction of the sample with 5% H_2 in Ar (balance) at room temperature and heating the catalyst in this gas mixture with a 8 °C/min ramp for 60 min up to 500 °C.

Step 2. Soaking at 500 °C for 60 min in 5% H_2 in Ar (balanced) mixture.

Step 3. Cooling of the catalyst with a 4 °C/min ramp for 70 min down to 185 °C, then with a 2 °C/min ramp for 80 min down to room temperature.

Step 4. Switching to 100% Ar flow for 30 min at room temperature.

Step 5. Switching to 1% CO and 10% O_2 in Argon (balance) at room temperature for 60 min, then heating the sample in this gas mixture with a 8 °C/min ramp for 60 min up to 500 °C.

Step 6. Soaking at 500 °C for 30 min in the 1% CO and 10% O_2 in Argon (balance) mixture.

Step 7. Cooling the catalyst with a 4 °C/min ramp for 70 min down to 185 °C, then with a 2 °C/min ramp for 80 min down to room temperature.

Step 8. Switching to 5% H_2 in Ar (balance) at room temperature for 30 min, then heating the sample with a 8 °C/min ramp for 60 min up to 500 °C.

Step 9. Soaking at 500 °C for 120 min in 5% H_2 in Ar (balance) mixture.

Step 10. Cooling the catalyst with a 4 °C/min ramp for 70 min down to 185 °C, then with a 2 °C/ min ramp for 80 min down to room temperature.

Step 11. Switching to 100% Ar flow for 30 min at room temperature.

Step 12. Switching to 1% CO and 10% O_2 in Argon (balance) at room temperature for 60 min, then heating the sample in this gas mixture with a 8 °C/min ramp for 60 min up to 500 °C.

Step 13. Soak at 500 °C for 30 min in the 1% CO and 10% O_2 in Argon (balance) mixture.

Step 14. Cooling the catalyst with a 4 °C/min ramp for 70 min down to 185 °C, then with a 2 °C/min ramp for 80 min down to room temperature.

Step 15. Switching to 100% Ar flow for 120 min at room temperature.

Note that the first (step 1-3) and the second (step 4-7) cycles aim to measure the activity of catalysts whereas, the third (step 8-10) and the fourth (step 11-15) cycles intend to measure the stability of the catalysts.

One of the major differences between the first and the second catalytic performance test procedures was that in the second procedure (MFR), we used a lower flow rate (200 ml/min) which decreases the WHSV as well as GHSV (with the same amount of catalyst, i.e., 100 mg). Moreover, temperature range for the second procedure was 25-400 °C. The remaining parameters were kept identical in both of the procedures.

Fig. 20a shows the catalytic CO oxidation test results for 0.2 wt% and 1 wt% $IrCl_3$-CeO_2 samples synthesized with incipient wetness impregnation (IWI) method and test under high flow rate (HFR, 500 ml/min) test conditions. As can be seen in Fig. 20, 50% and 90% CO to CO_2 conversion took place at T_{50} = 221 °C and T_{90} = 267 °C for 0.2 wt% $IrCl_3$-CeO_2 (IWI-HFR), respectively. Note that T_{50} is also called the light-off temperature. On the other hand, in the case of 1 wt% $IrCl_3$-CeO_2 (IWI-HFR), T_{50} and T_{90} values were observed at 197 °C and 241 °C, respectively (Fig. 20b).

Similar experiments were also carried out for 0.2-0.5-1 wt% $IrCl_3$-CeO_2 at a moderate flow rate of 200 ml/min corresponding to a longer residence time and a lower GHSV as illustrated in Fig. 21a-b. As expected, improved (i.e., lower) T_{50} and T_{90} values were obtained under moderate flow rate conditions due to the slower kinetics and lower overall reaction rate. Influence of the flow rate on the activation temperatures was also explicitly depicted in Fig. 22 for the 1 wt% $IrCl_3$-CeO_2 (IWI-MFR) catalyst which illustrates that T_{50} , $T_{90,}$ and T_{100} values are higher for the higher reactant flow rate used in the catalytic tests.

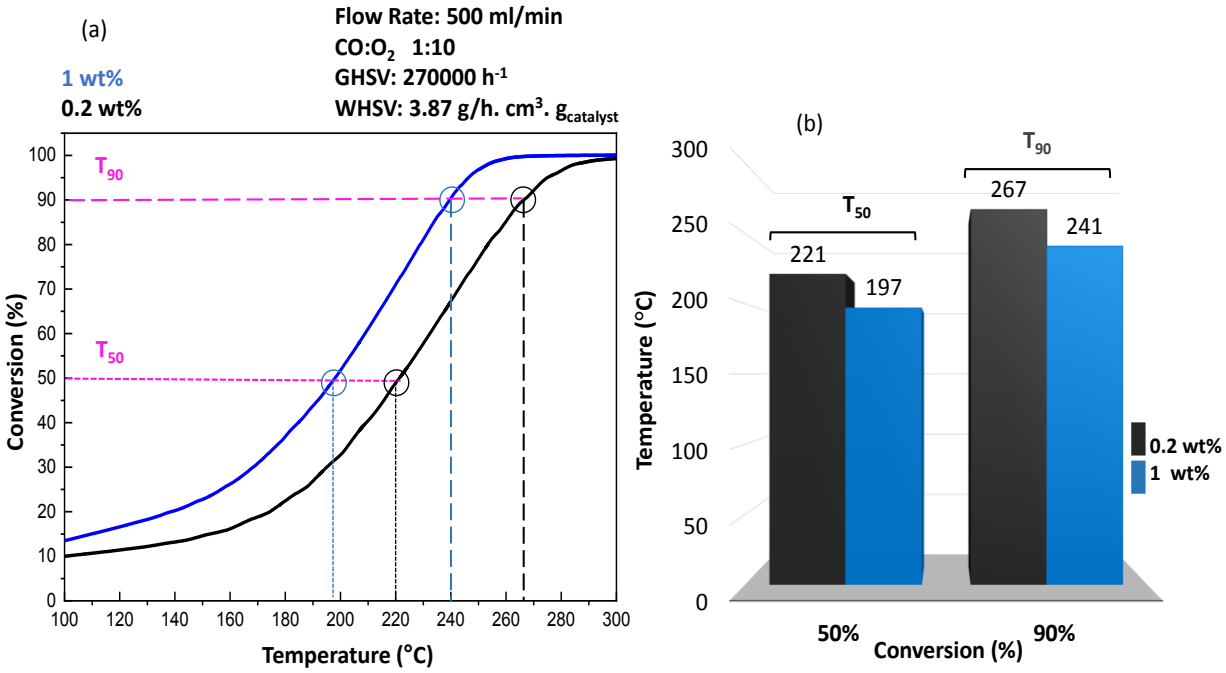

Figure 20. Catalytic CO oxidation test results for 0.2 wt% $IrCl_3$-CeO_2(IWI-HFR), and 1 wt% $IrCl_3$-CeO_2(IWI-HFR) samples. (a) CO conversion % data, (b) T_{50} and T_{90} comparison for different catalysts. All the samples were treated in 5 wt.% H_2 in Ar with a flow rate of 500 ml/min at 500 °C for 2 h inside the catalytic reactor before the catalytic tests.

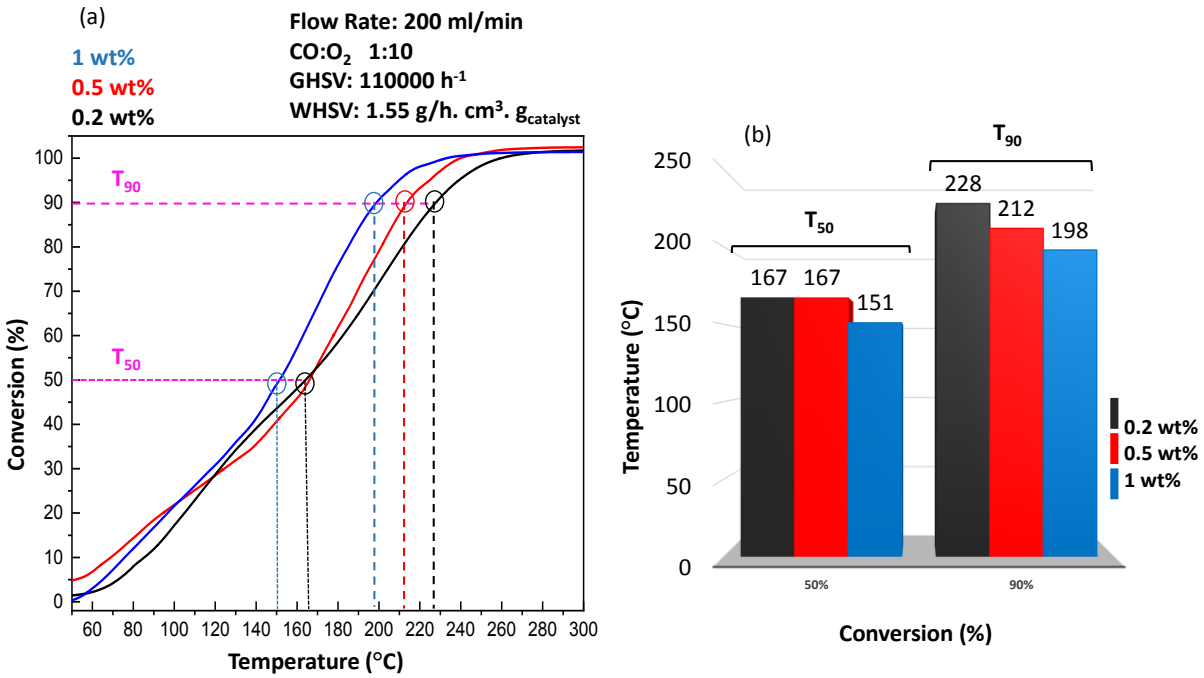

Figure 21. Catalytic CO oxidation test results for 0.2 wt% $IrCl_3$-CeO_2(IWI-MFR), 0.5 wt% $IrCl_3$-CeO_2(IWI-MFR), and 1 wt% $IrCl_3$-CeO_2(IWI-MFR) samples. (a) CO conversion % data, (b) T_{50} and T_{90} comparison for different catalysts. All the samples were treated in 5 wt.% H_2 in Ar with a flow rate of 200 ml/min at 400 °C for 2 h inside the catalytic reactor before the catalytic tests.

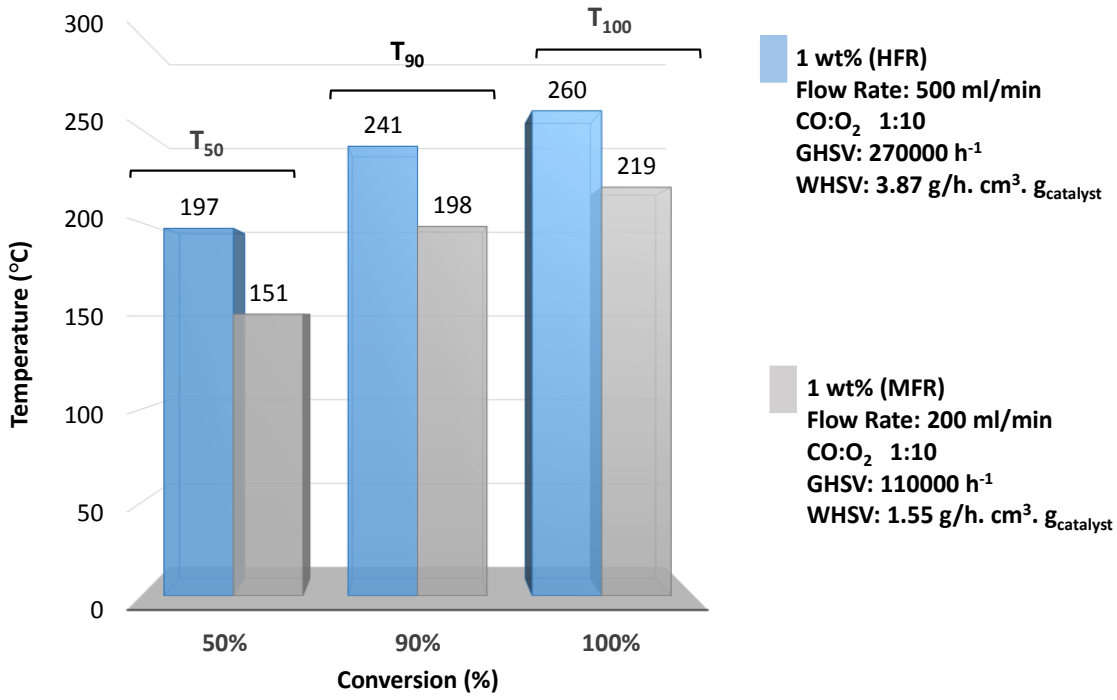

Figure 22. Effect of flow rate and space velocity on catalytic performance of the 1 wt% $IrCl_3$-CeO_2(IWI-MFR) catalyst.

In an analogous manner, we performed catalytic CO oxidation performance tests on other families of catalysts which were synthesized by IWI method ($IrCl_3$ on LaZr, and TiZr for three different metal loadings (i.e., 0.2, 0.5 and 1 wt%)). Since Fig. 20-22 indicate that activation temperatures were favorably lowered under moderate flow rate (MFR) conditions, we used MFR for the catalytic tests on the catalysts containing LaZr (Fig. 23) and TiZr (Fig. 24) support materials.

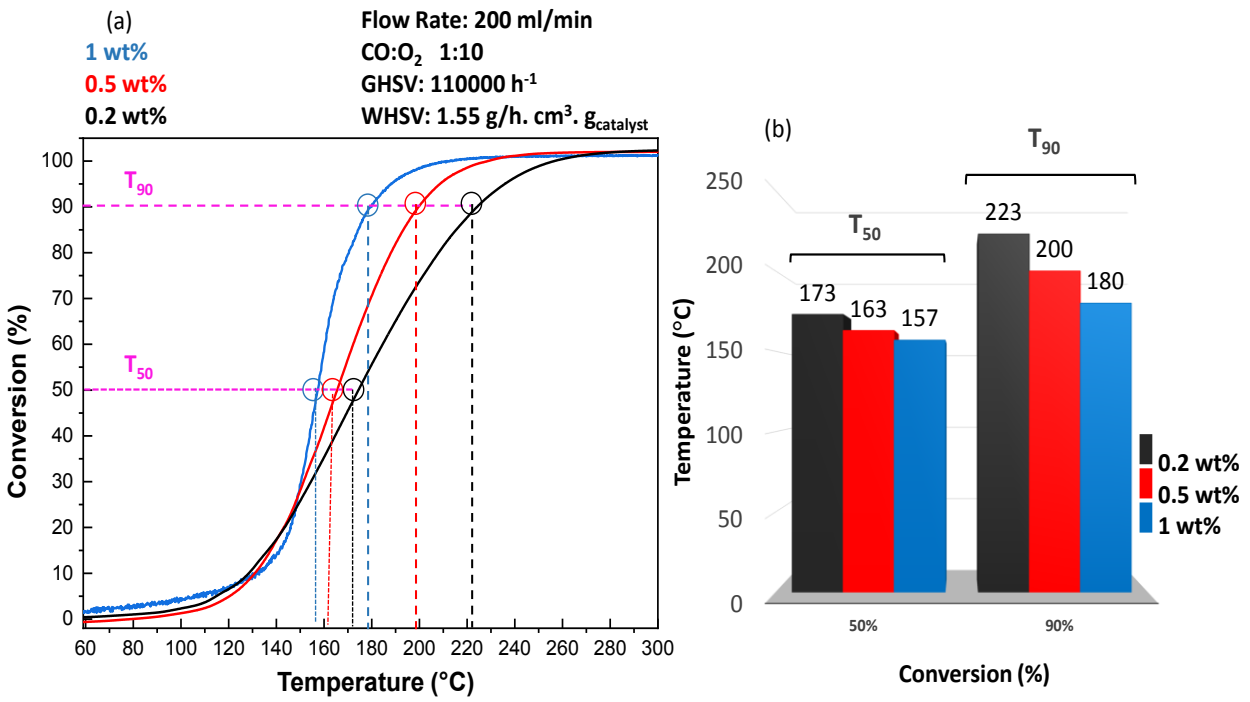

Figure 23 Catalytic CO oxidation test results for 0.2 wt% $IrCl_3$-LaZr(IWI-MFR), 0.5 wt% $IrCl_3$-LaZr(IWI-MFR), and 1 wt% $IrCl_3$-LaZr(IWI-MFR) samples. (a) CO conversion % data, (b) T_{50} and T_{90} comparison for different catalysts. All the samples were treated in 5 wt.% H_2 in Ar with a flow rate of 200 ml/min at 400 °C for 2 h inside the catalytic reactor before the catalytic tests.

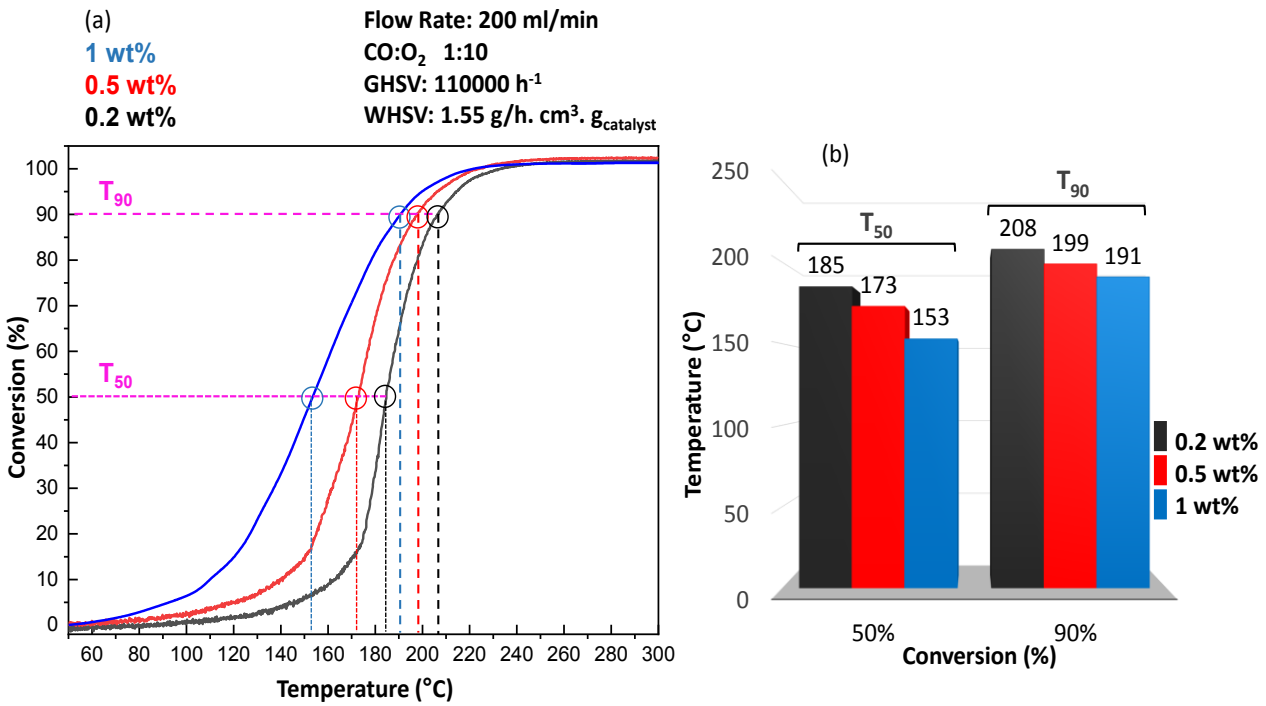

Figure 24 Catalytic CO oxidation test results for 0.2 wt% $IrCl_3$-TiZr(IWI-MFR), 0.5 wt% $IrCl_3$-TiZr(IWI-MFR), and 1 wt% $IrCl_3$-TiZr(IWI-MFR) samples. (a) CO conversion % data, (b) T_{50} and T_{90} comparison for different catalysts. All the samples were treated in 5 wt.% H_2 in Ar with a flow rate of 200 ml/min at 400 °C for 2 h inside the catalytic reactor before the catalytic tests.

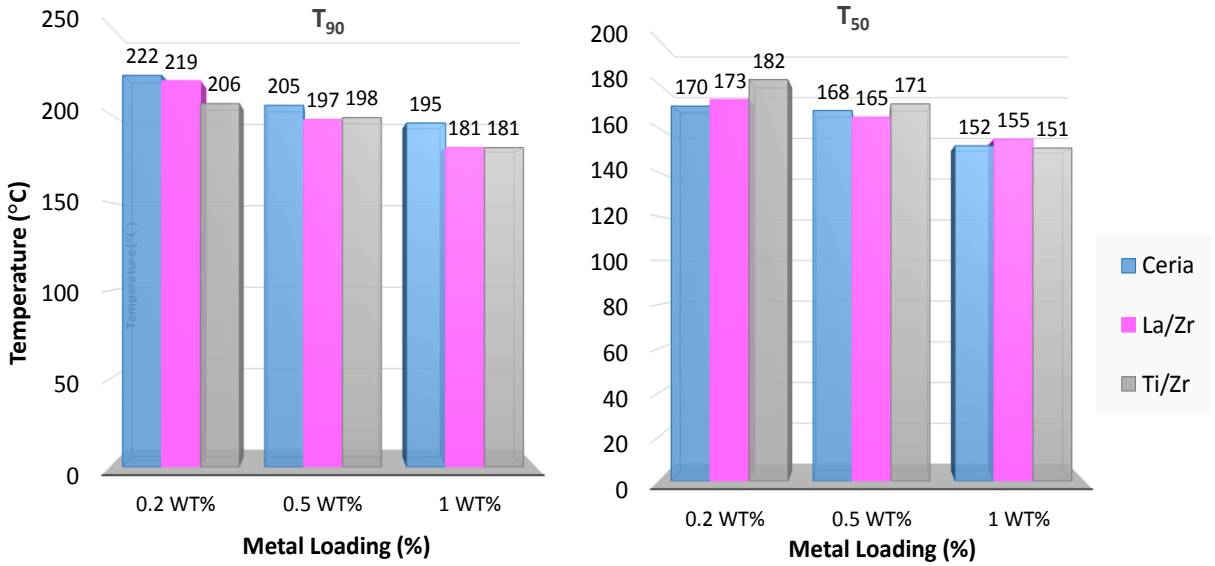

Figure 25. Comparison of T_{90} and T_{50} values for Ir catalysts supported on CeO_2, LaZr and TiZr via IWI method in catalytic CO oxidation under MFR conditions.

As can be realized in Fig. 25, for all support materials, increasing Ir loading enables lower 50% and 90% conversion temperatures. This can be ascribed to the increasing number of Ir active sites with increasing Ir loading of the catalysts. Fig. 25 indicates that, influence of the support type on T_{50} and T_{90} values is rather limited for a given Ir metal loading. In other words, for a given metal loading, T_{50} and T_{90} values only vary by maximum 16 °C on different support materials. Thus, the reducible metal oxide support materials used in the current work (i.e., ceria, lanthana-zirconia, and titania-zirconia) lead to comparable reactivity for Ir active sites in catalytic CO oxidation under moderate flow rate (200 ml/min) conditions.

On the other hand, an interesting trend can be observed when activity trends at two different isothermal conditions are compared for a given support material at different loadings as presented in Fig. 26. In Fig. 26, CO conversion at 150 °C vs. 180 °C are plotted for the $IrCl_3$-LaZr(IWI-MFR) catalysts as a function of Ir loading. For an ideal Ir dispersion on the LaZr support material where all Ir active sites are fully exposed to reactants, one may expect that the catalytic CO conversion at a given temperature should increase linearly with increasing Ir loading in the catalyst formulation. This is shown by the dashed lines in Fig. 26 marked as "Expectation". On the other hand, under realistic experimental conditions, due to the inefficient dispersion of Ir active sites on the LaZr support material leading to the formation of Ir clusters/nanoparticles where not all of the Ir active sites are exposed to the reactants, actual conversion values are measured to be lower than that of the ideal case. This is plotted by the solid lines in Fig. 26 and marked as "experiment". It is apparent that at a high Ir loading of 1 wt%, there exists a drastic gap between the "expected" and the "experimental" CO conversions. Strikingly, this gap is actually very small for 0.5 wt% case. This important finding suggests that extremely high dispersion Ir actives sites can be obtained on LaZr support material by keeping the Ir loading at $\leq$0.5 wt.% where higher loadings of Ir lead to agglomeration of Ir to form larger clusters/nanoparticles rendering some Ir active sites inaccessible by the reactants. Hence, current experimental results suggest that for the design of cost-efficient Ir catalysts for CO oxidation, rather than using high (e.g., 1 wt%) Ir loadings on a reducible support material, using a lower Ir loading of 0.5 wt.% and utilization of greater total catalyst masses may be a better strategy to optimize Ir the atom economy of the catalyst (Fig. 27).

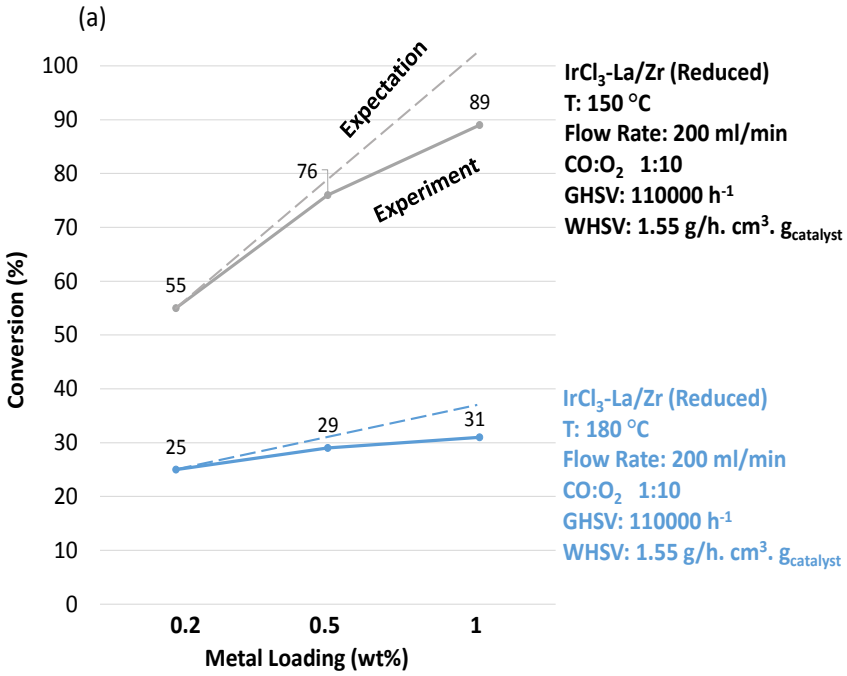
(a)
100
90
80
70
60
50
40
30
20
10
0
Conversion (%)
Expectation
Experiment
89
76
55
29
31
25
0.2
0.5
1
Metal Loading (wt%)
IrCl3-La/Zr (Reduced)
T: 150 °C
Flow Rate: 200 ml/min
CO:O2 1:10
GHSV: 110000 h-1
WHSV: 1.55 g/h. cm3. gcatalyst
IrCl3-La/Zr (Reduced)
T: 180 °C
Flow Rate: 200 ml/min
CO:O2 1:10
GHSV: 110000 h-1
WHSV: 1.55 g/h. cm3. gcatalyst

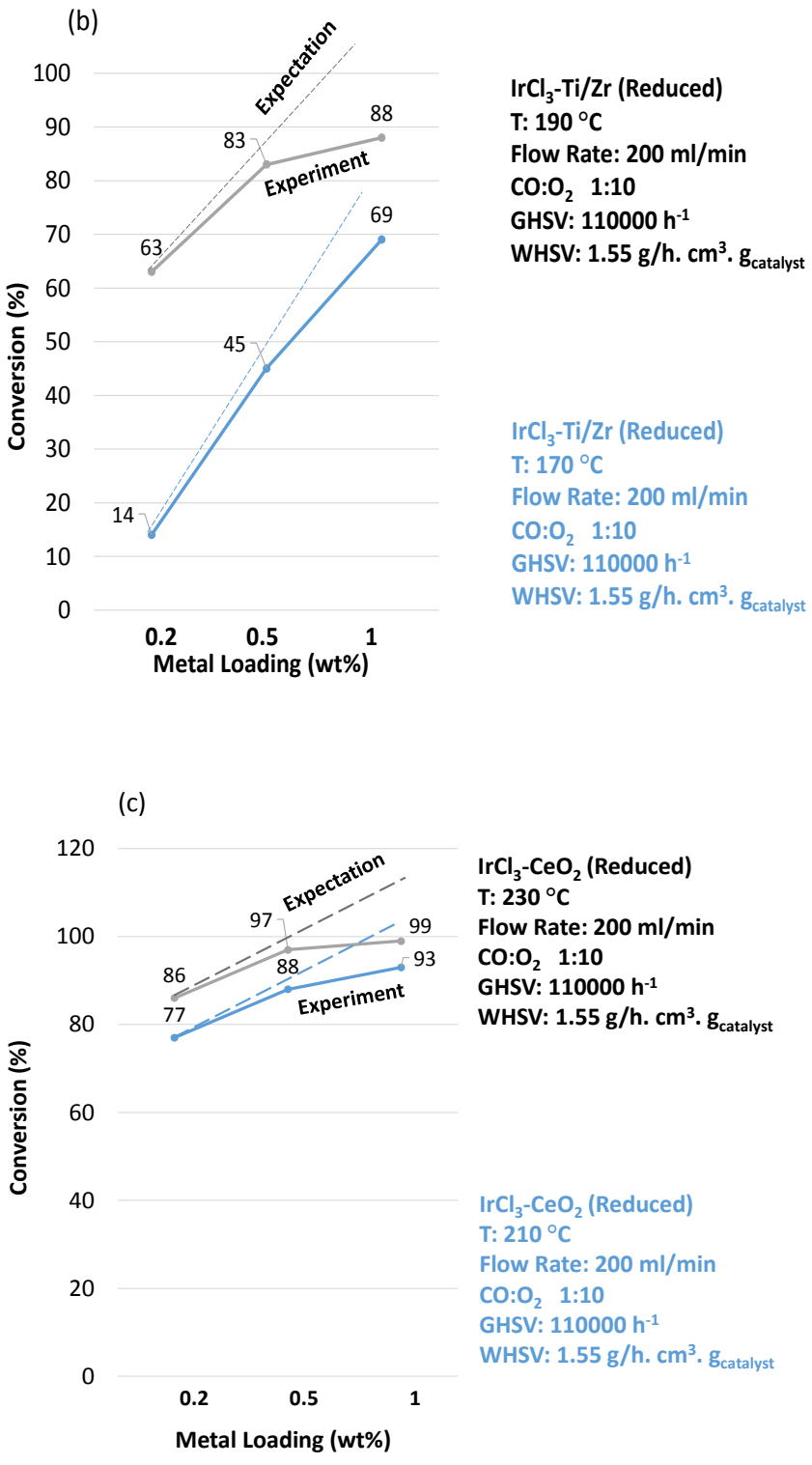

Figure 26. Comparison of the isothermal CO oxidation conversion values at two different temperstures for 1 wt% (IWI-MFR) catalysts as a function of Ir loading.

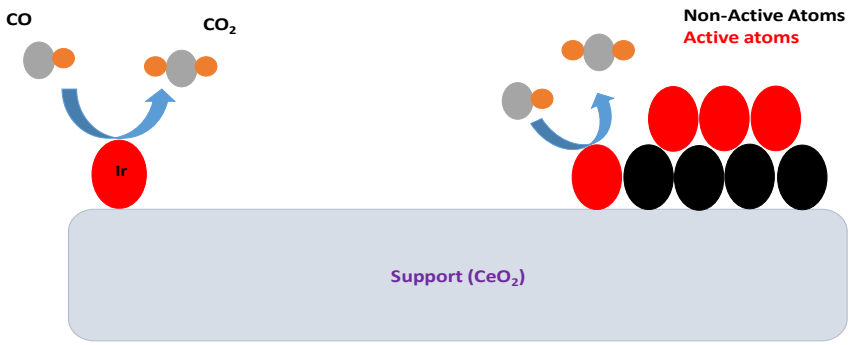

Figure 27. Conceptual representation of active and inactive Ir atoms in supported IR catalysts in CO oxidation.

After obtaining detailed information on the reactivity of the investigated catalysts in the CO oxidation reaction, we carried out detailed characterization experiments to find structure-functionality relationships for the investigated catalysts. These results are presented in the forthcoming sections given below.

3.1.2 In-situ FTIR Spectroscopic Studies

3.1.2.1 CO Adsorption on the Investigated Catalysts via In-Situ FTIR

Detailed investigation of the in-situ FTIR spectra of adsorbed CO molecules on catalyst surfaces such as the positions, width and relative intensities of the IR bands may yield valuable information regarding the dispersion, oxidation states, and relative particle sizes of the PGM sites. Furthermore, use of CO as an informative probe molecule in in-situ FTIR studies on catalyst surfaces may also reveal insights on the influence of pretreatment conditions on the catalyst structure, presence of contaminations and structural differences in the support materials used in the synthesis [54-61].

Former in-situ FTIR studies in the literature reported the presence of small Ir clusters evident by the observation of gem-dicarbonyls on Ir [62-68]. Furthermore, it was also demonstrated in other studies that as the full width at half maximum (FHWM) of the CO IR bands decreases (i.e., as the IR bands become sharper) Ir cluster size decreases and Ir dispersion on the catalyst support typically increases (Fig. 28-29). [69-74]. In addition, absence of high frequency CO stretching peaks (> 2080 cm^{-1}) typically indicates the presence of species with lower oxidation states [54].

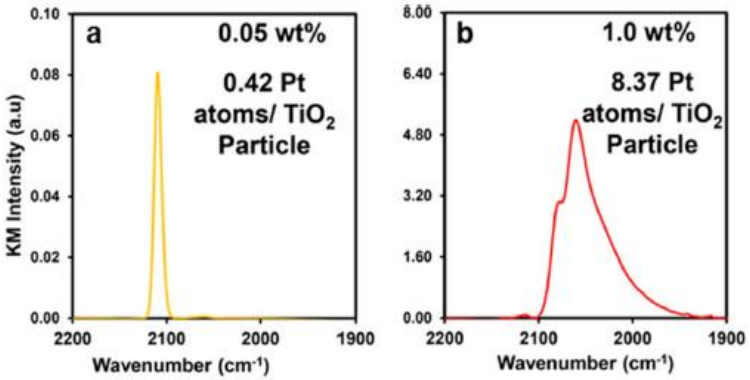

Figure 28. In-situ FTIR spectra for CO adsorption on Pt/TiO_2 catalysts with different Pt loading leading to different Pt cluster sizes. Here, low loading (a) corresponds to atomic Pt dispersion and sharp IR bands and higher loading (a) corresponds to the formation of bigger Pt nanoparticles and broader Ir bands [56].

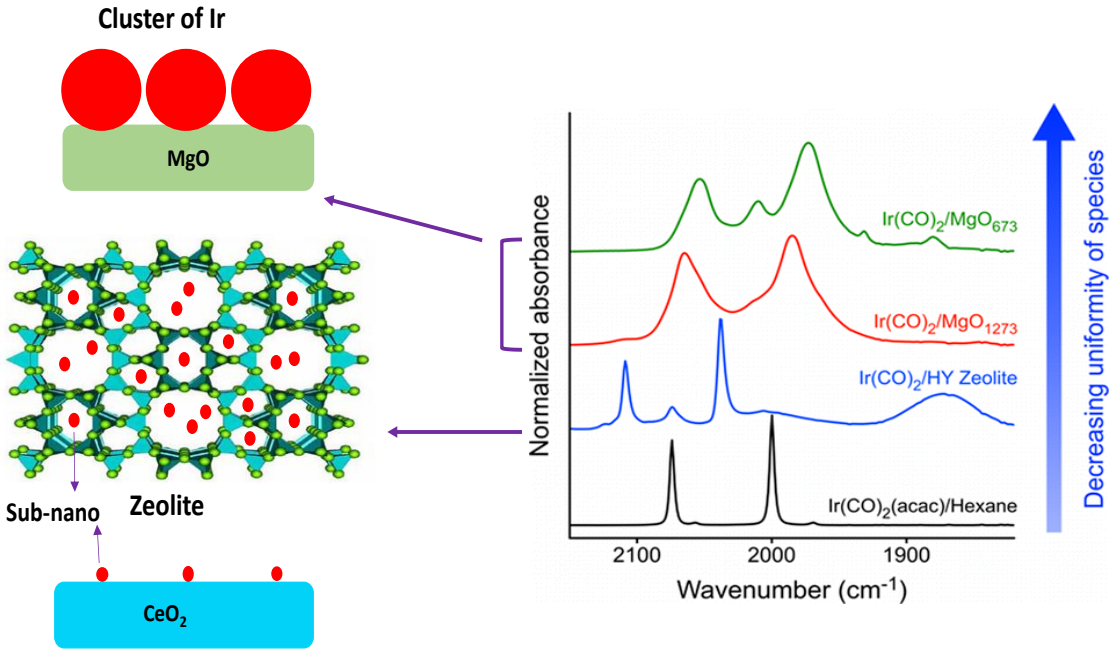

Figure 29. In-situ FTIR spectra for CO adsorption on iridium sites on different supports [62].

Table 11 lists typical vibrational frequencies for various types of CO adsorption configurations on different Ir adsorption sites.

Table 11. Typical vibrational frequencies for various types of CO adsorption configurations on different Ir adsorption sites [62].

Type of Interactions	Wavenumber Range (cm^{-1})
O Bridging (Ir-C-Ir)	1700-1930
Gem-Dicarbonyls (OC-Ir-CO)	1820-1980 (Asymmetric Stretching) and 1890-2060 (Symmetric Stretching)
Atop/ontop/linear (Ir-CO)	2000-2290

3.1.2.1.1 In-situ FTIR: CO Adsorption on Samples Synthesized by "Classical Impregnation" (CI) Method

3.1.2.1.1.1 $Ir(acac)_3$-MgO (CI)

Using CO adsorption via in-situ FTIR spectroscopy as an effective functional characterization method, we aimed to determine the existence of highly dispersed small Ir clusters on the chosen support materials. Fig. 30 shows the corresponding in-situ FTIR data for 0.2 and 0.5 wt% $Ir(acac)_3$-MgO (CI) samples synthesized via classical impregnation method and pretreated at various conditions. It is seen in Fig. 30a that 0.2 and 0.5 wt% $Ir(acac)_3$-MgO (CI) samples annealed in oxygen did not yield sharp and intense vibrational features indicating the lack of small Ir clusters accessible for CO adsorption on the MgO support. Similar observations were also found for this sample treated in hydrogen (Fig. 30b) or air (Fig. 30c). Presence of a broad and convoluted feature at 1940-1970 in Fig 30b-c suggests the existence of large and metallic Ir nanoparticles on MgO with low dispersion [62]. The 2170 cm^{-1} feature seen in Fig.30b is consistent with the presence of additional oxidic (IrO_x) species [63]. In light of these findings, no further detailed catalytic tests were carried out on the MgO support material.

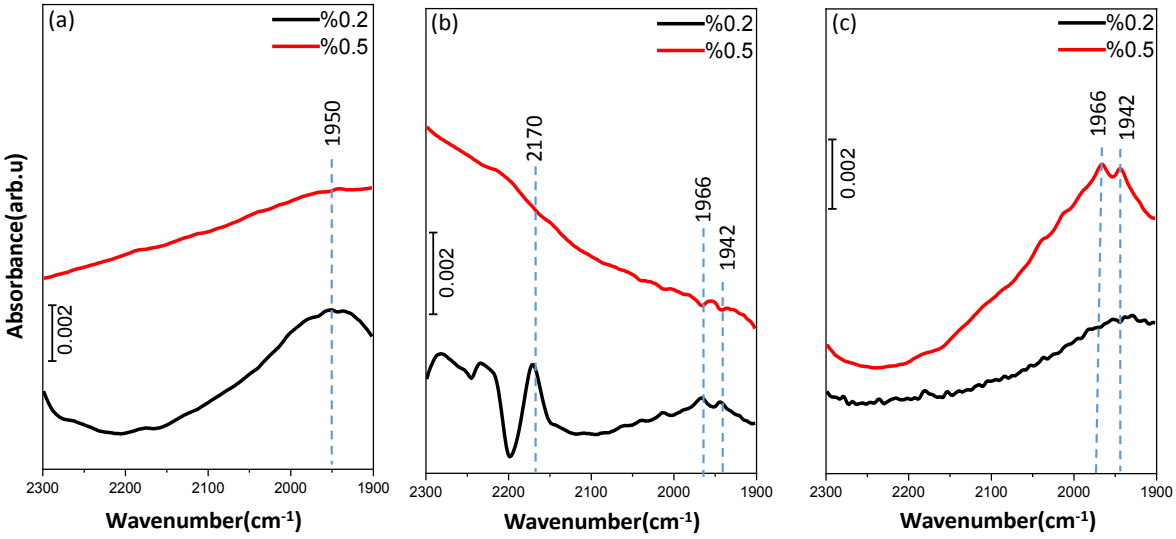

Figure 30. In-situ CO adsorption FTIR spectra for 0.2 and 0.5 wt% $Ir(acac)_3$-MgO (CI) samples a) annealed in 20% O_2 in Ar for 2 h at 500 °C, b) annealed in 5% H_2 in Ar for 2 h at 500 °C, and c) calcined in air for 5 h at 800 °C.

3.1.2.1.1.2 $Ir(acac)_3$-CeO_2 (CI)

Similar in-situ FTIR analysis on 0.2 and 0.5 wt% $Ir(acac)_3$-CeO_2 (CI) samples where CO was used as a probe molecule indicated more intense but still broad signals located at 2173-2130, 2040-2050, and 1960-1980 cm^{-1}. The first set of bands within 2193-2130 cm^{-1} can be ascribed to CO adsorption on oxidic Ir sites (IrO_x) with different oxidation states due to the presence of large (> 1 nm) IrO_x nanoparticles [57]. The second set of bands at 2040-2060 cm^{-1} can be assigned to CO atop/linear adsorption on large metallic Ir nanoparticles. Finally, the third group of bands within 1960-1980 cm^{-1} are associated to bridging CO adsorption on metallic Ir nanoparticles. Figure 31 shows that pretreatment conditions have a strong effect on the oxidation state and morphology of the Ir/IrOx nanoparticles on CeO_2 prepared with CI method. Disappearance/attenuation of the FTIR signals for particular Ir loadings after some pretreatment conditions is probably an indication for the well-known "Strong Metal Support Interaction" (SMSI) where metal oxide surface covers the PGM active sites and make them unavailable for CO adsorption [58]. Note that the negative

features observed in Fig 31 can be due to substitution of CO probe molecules with acetylacetonate-related residues originating from the Ir precursor ($Ir(acac)_3$) [61].

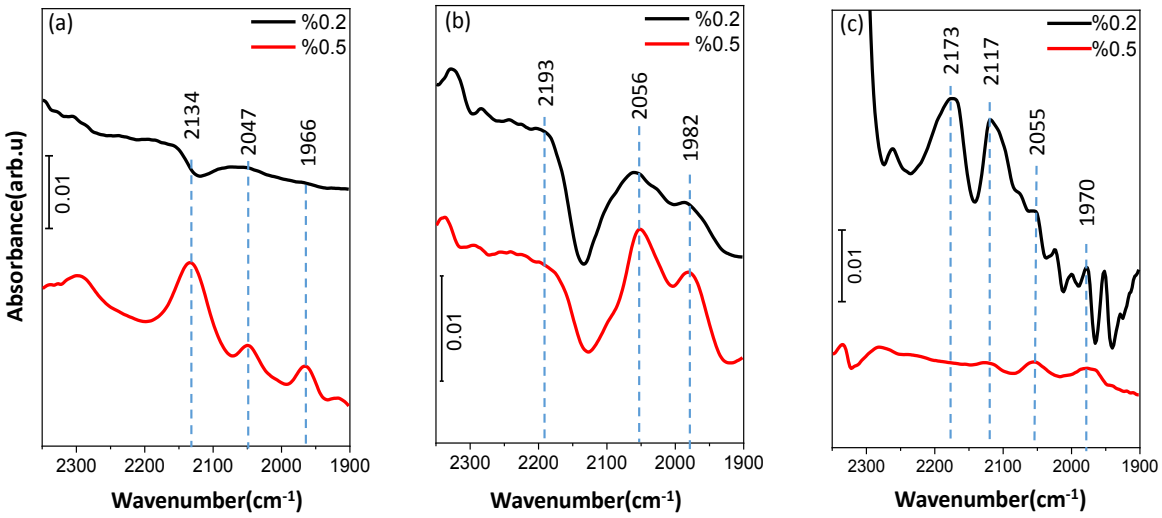

Figure 31. In-situ CO adsorption FTIR spectra for 0.2 and 0.5 wt% $Ir(acac)_3$-CeO_2 (CI) samples a) annealed in 20% O_2 in Ar for 2 h at 500 °C, b) annealed in 5% H_2 in Ar for 2 h at 500 °C, and c) calcined in air for 5 h at 800 °C.

3.1.2.1.1.3 $IrCl_3$- CeO_2 (CI)

Since $Ir(acac)_3$-CeO_2 (CI) samples prepared with an "acac" precursor did not yield indications of the predominance of high Ir dispersion and small Ir clusters, we tried similar experiments on ceria support by changing the Ir precursor where we utilized $IrCl_3$ as the source of Ir. In-situ FTIR results for these samples are given in Fig. 32.

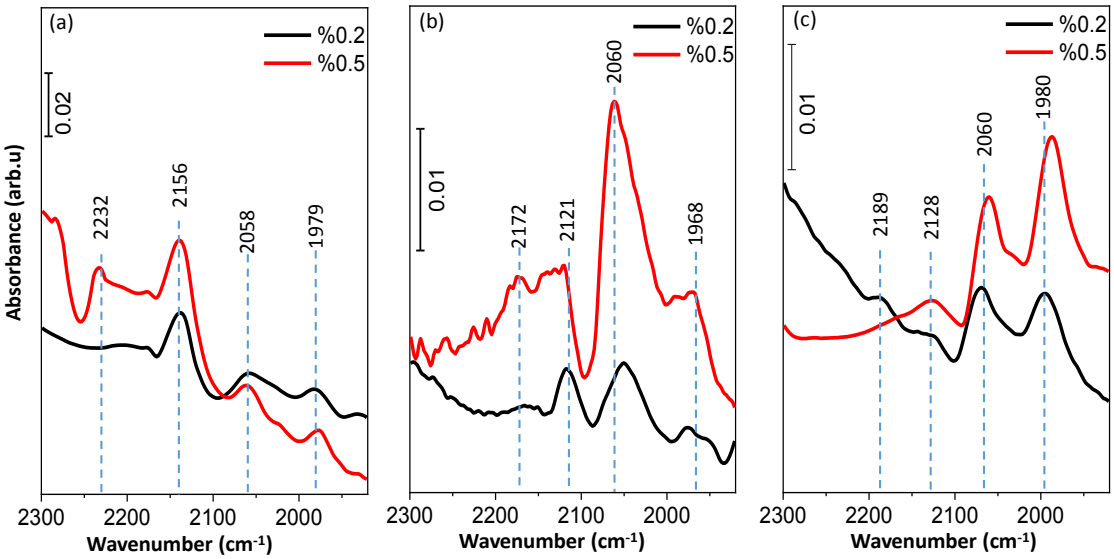

Figure 32. In-situ CO adsorption FTIR spectra for 0.2 and 0.5 wt% $IrCl_3$-CeO_2 (CI) samples a) annealed in 20% O_2 in Ar for 2 h at 500 °C, b) annealed in 5% H_2 in Ar for 2 h at 500 °C, and c) calcined in air for 5 h at 800 °C.

Annealing of the $IrCl_3$- CeO_2 (CI) samples in O_2 (Fig. 32a) mostly leads to large and oxidic Ir nanoparticles evident by the presence of a major vibrational signature at a high frequency of 2156 cm^{-1}. Weaker broad features at 2058 and 1979 cm^{-1} can be ascribed to atop and bridging adsorption on metallic Ir nanoparticles, respectively [68]. Reduction of the $IrCl_3$- CeO_2 (CI) sample in H_2 (Fig. 32b) results significant growth in the broad IR band at 2060 cm^{-1} due to atop CO adsorption on large metallic Ir nanoparticles (while smaller metallic Ir clusters may also exist for 0.2 wt% Ir case), consistent with the reducing effect of hydrogen treatment. Note that Fig 32b indicates that some oxidic Ir species are also present on this latter sample verified by the presence of vibrational signatures at 2172-2121 cm^{-1} particularly for the 1 wt% Ir case. On the other hand, calcination of the $IrCl_3$- CeO_2 (CI) samples in air (Fig. 32c) has a weaker oxidizing effect as compared to annealing in O_2 (Fig. 32a). In-situ FTIR spectra given in Fig. 32c shows that while IrO_x species existed on this sample (2189-2123 cm^{-1}), the predominant species were large metallic Ir nanoparticles indicated by the intense and convoluted 2060, 1980 cm^{-1} features associated with atop and bridging CO adsorption on Ir^0 sites, respectively.

As the classical impregnation method typically yielded mostly large Ir/IrOx nanoparticles on MgO and ceria support materials, we decided to change both the Ir deposition method and some of the support materials and proceeded our characterization studies with the incipient to wetness impregnation method using $IrCl_3$ precursor on ceria, lanthana-zirconia and titania-zirconia materials as discussed in the forthcoming sections.

3.1.2.1.2 In-situ FTIR: CO Adsorption for Samples Synthesized by "Incipient to Wetness Impregnation" (IWI) Method

3.1.2.1.2.1 $IrCl_3$-CeO_2 (IWI)

Fig. 33 presents in-situ FTIR data for CO adsorption on 0.2, 0.5 and 1 wt% $IrCl_3$-CeO_2 (IWI) samples pretreated under different conditions. In contrast to Fig. 30-32 corresponding to the samples synthesized via classical impregnation, Fig. 33 shows significantly sharper and well-resolved/uncovoluted FTIR signals with narrower FWHM values of 15-20 cm^{-1}. These observations (particularly for Fig. 33a and b) suggest the presence of both large Ir/IrOx nanoparticles as well as small Ir/Ir^{x+} clusters on the $IrCl_3$-CeO_2 (IWI) samples pretreated in O_2 or H_2. IR bands at 2055 and 1977 cm^{-1} (Fig. 33b) probably characterize the symmetric and asymmetric stretching frequencies of adsorbed CO probe molecules, with the frequencies matching those reported for single-site iridium carbonyls and confirming the formation of a supported iridium gem-dicarbonyl [62]. In contrast, broadening of the IR signals in Fig. 33c for calcination in air can be explained by sintering and growth of bigger Ir/IrO_x nanoparticles as a result of hydrothermal aging originating from humidity and O_2 in air. This will be further justified by the current TEM results presented in the forthcoming sections.

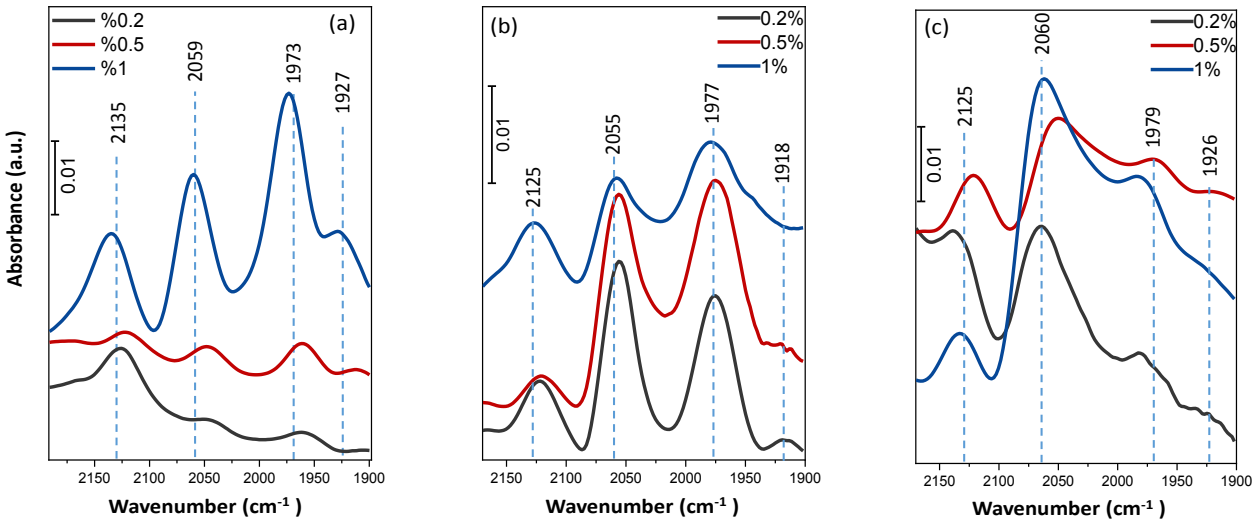

Figure 33. In-situ CO adsorption FTIR spectra for 0.2, 0.5 and 1 wt% $IrCl_3$-CeO_2 (IWI) samples a) annealed in 20% O_2 in Ar for 2 h at 500 °C, b) annealed in 5% H_2 in Ar for 2 h at 500 °C, and c) calcined in air for 5 h at 800 °C.

3.1.2.1.2.2 $IrCl_3$-La_2O_3/ZrO_2 (IWI)

In-situ FTIR spectra of the $IrCl_3$-La_2O_3/ZrO_2 (IWI) catalysts with different loadings given in Fig. 34 includes a broad and very high frequency vibrational feature at 2281 cm^{-1} which can be due to CO adsorption on the lanthana-zirconia support or on Ir^{x+} sites with a large diameter. In addition to this feature, there exists other low frequency IR peaks in Fig. 34 at < 2010 cm^{-1}, which can be attributed to CO adsorption with atop and bridging configurations on large metallic Ir nanoparticles. Strengthening of the band at 1901-1892 cm^{-1} after reduction in hydrogen (Fig. 34b) and calcination in air (Fig. 34c) is also consistent with the sintering and growth of Ir nanoparticles after aging.

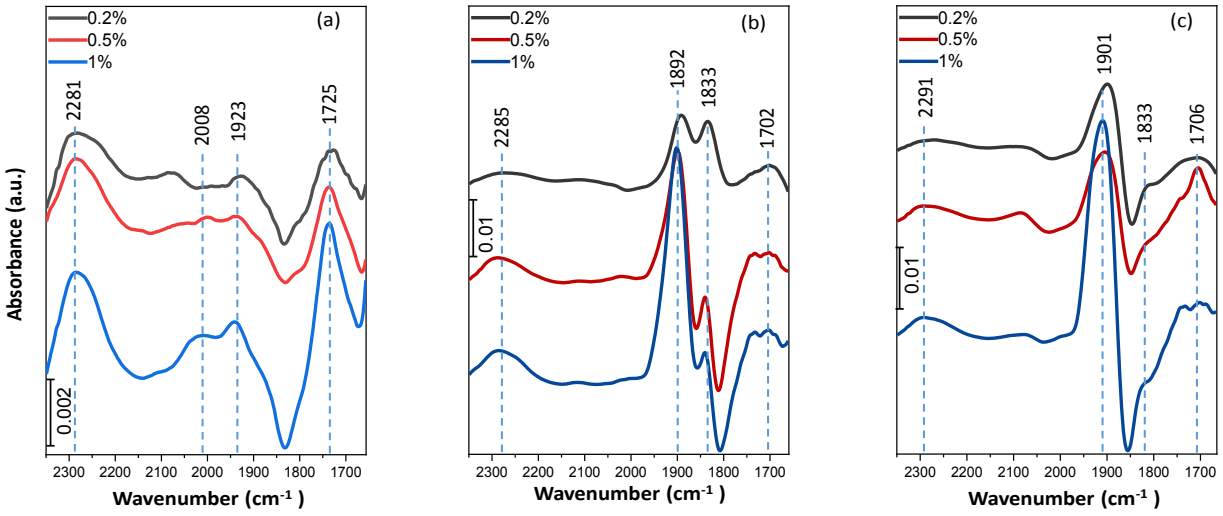

Figure 34. In-situ CO adsorption FTIR spectra for 0.2, 0.5 and 1 wt% $IrCl_3$-La_2O_3/ZrO_2 (IWI) samples a) annealed in 20% O_2 in Ar for 2 h at 500 °C, b) annealed in 5% H_2 in Ar for 2 h at 500 °C, and c) calcined in air for 5 h at 800 °C

3.1.2.1.2.3 $IrCl_3$-TiO_2/ZrO_2 (IWI)

Analogous in-situ FTIR spectroscopic analysis of $IrCl_3$-TiO_2/ZrO_2 (IWI) catalysts prepared with different loadings and pretreated under various conditions (Fig. 35) reveal the lack of clear signatures for the predominance of small Ir clusters. These spectra prevalently included relatively convoluted, broad and low frequency (< 2010 cm^{-1}) IR signatures which are indications of high coordination CO adsorption on large metallic Ir nanoparticles. On the other hand, presence of small sub-nanometer Ir clusters as minority species cannot be excluded.

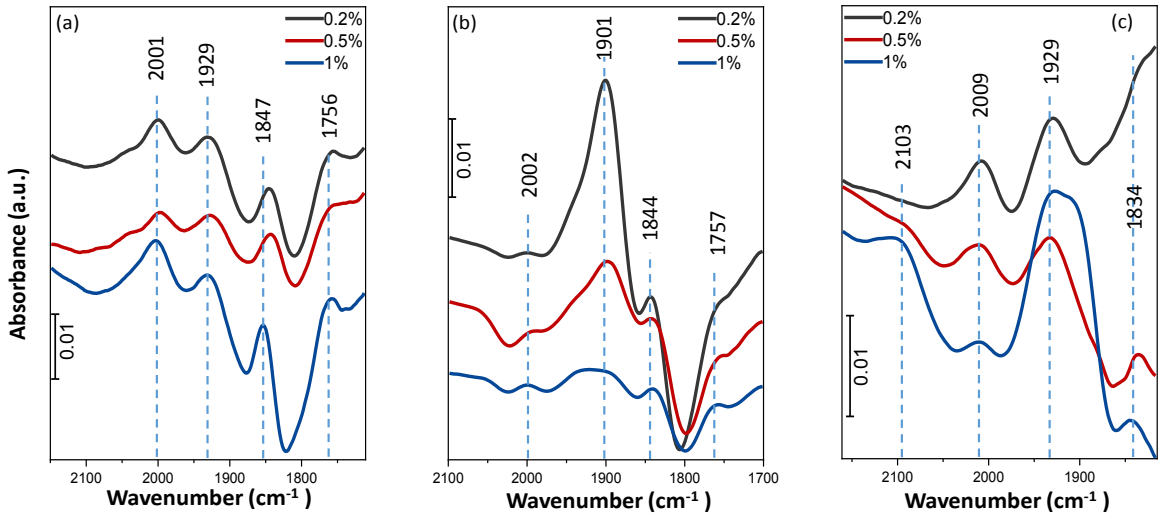

Figure 35. In-situ CO adsorption FTIR spectra for 0.2, 0.5 and wt% $IrCl_3$- TiO_2/ZrO_2 (IWI) samples a) annealed in 20% O_2 in Ar for 2 h at 500 °C, b) annealed in 5% H_2 in Ar for 2 h at 500 °C, and c) calcined in air for 5 h at 800 °C.

3.2 Structural characterization

3.2.1 TEM-EDX

CO adsorption via in-situ FTIR spectroscopic results indicated that among the samples studied, $IrCl_3$-CeO_2 (IWI) samples revealed the strongest indication for the presence of small and highly dispersed Ir clusters. Thus, this ample was investigated in detail via TEM and EDX techniques after various pretreatment conditions. As can be seen in the TEM image given in Fig. 36, despite the relatively high Ir loading of this particular catalyst (i.e., 1 wt%), there are no clearly visible Ir clusters detectable via TEM. This observation is in line with the dominant presence of small and well-dispersed (< 1 nm) Ir clusters on the $IrCl_3$-CeO_2 (IWI) catalyst after reduction in hydrogen, which is in good accordance with the current in-situ FTIR results (Fig. 33). Fine dispersion of 1 wt% $IrCl_3$-CeO_2 (IWI) catalyst after hydrogen treatment is also seen in the TEM-EDX data given in Fig. 37. Due to the fine dispersion of Ir, corresponding EDX signal falls below the instrumental detection limit, while the presence of Ir in this sample is justified by the current in-situ FTIR data (Fig. 33a).

Figure 36. HRTEM image of 1 wt% $IrCl_3$-CeO_2 (IWI) catalyst after reduction in 5% H_2 in Ar at 500 °C for 5 h.

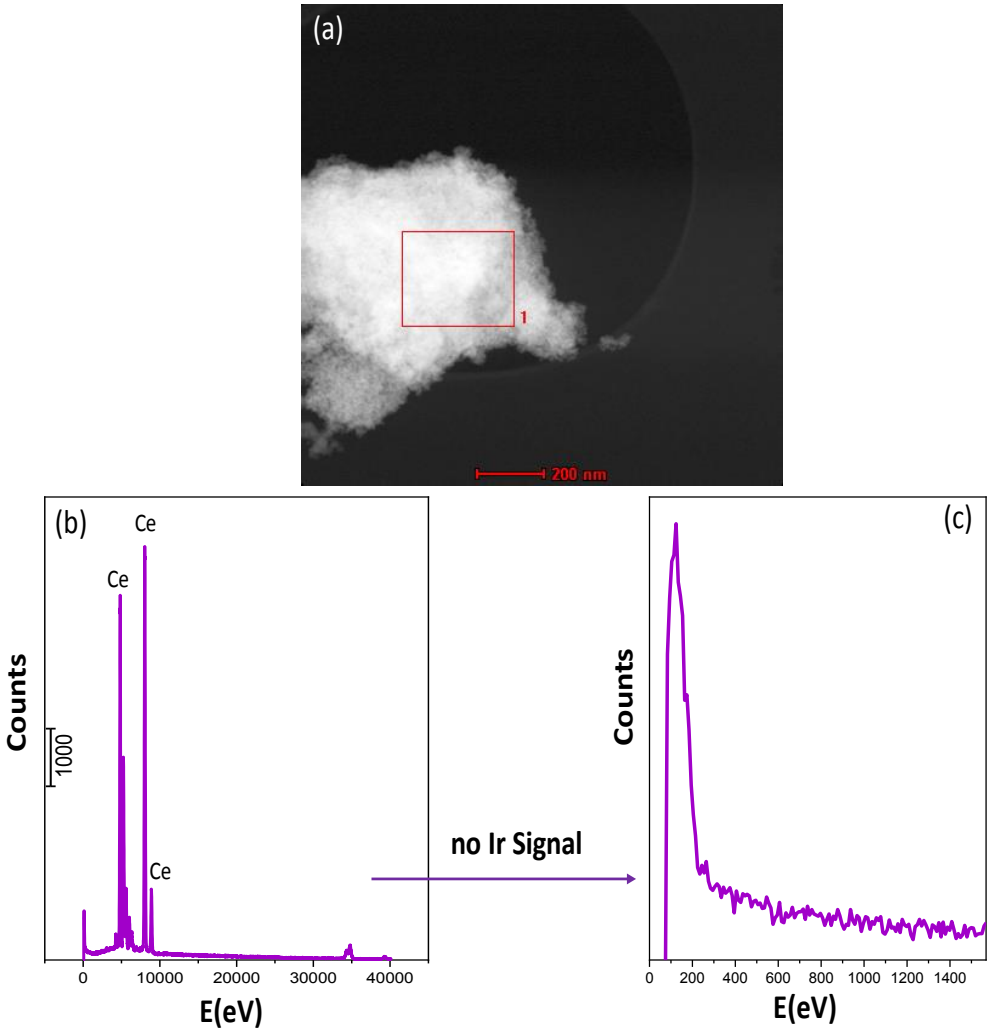

Figure 37. HAADF-TEM image (a) and TEM-EDX spectra (b and c) for 1 wt% $IrCl_3$-CeO_2 (IWI) sample annealed in H_2 catalyst. Spectra in (b-c) were collected from specified region depicted in (a).

Fig. 38 shows the TEM analysis of 1 wt% $IrCl_3$-CeO_2 (IWI) catalyst after annealing in oxygen. As expected from the corresponding in-situ FTIR data (Fig. 33b), large Ir nanoparticles are not observed for this sample and the average Ir particle size (< 1 nm) seems to be below the spatial detection limit of the currently used TEM.

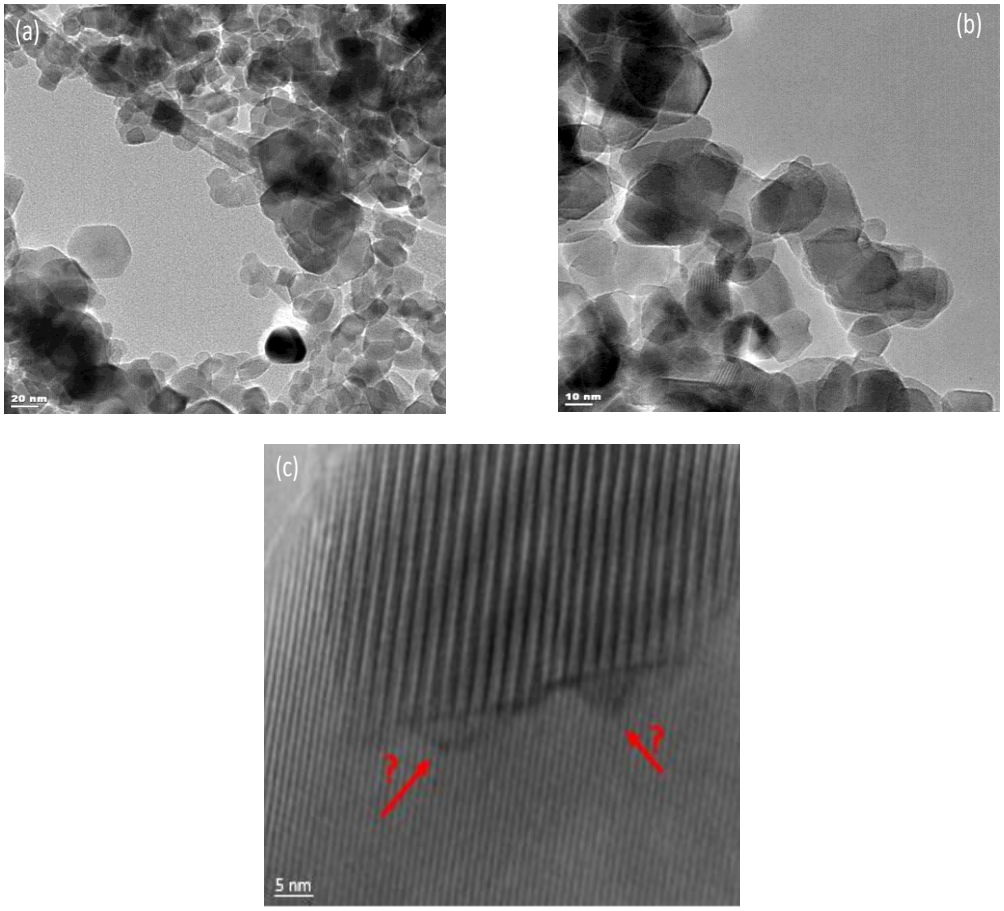

Figure 38. TEM images of 1 wt% $IrCl_3$-CeO_2 (IWI) sample annealed in 20% O_2 in Ar at 500 °C for 2 h.

Likewise, TEM-EDX analysis of the 1 wt% $IrCl_3$-CeO_2 (IWI) catalyst after annealing in oxygen (Fig. 39) did not yield any clear indications of Ir signals due to the fine dispersion of small Ir clusters on this catalyst.

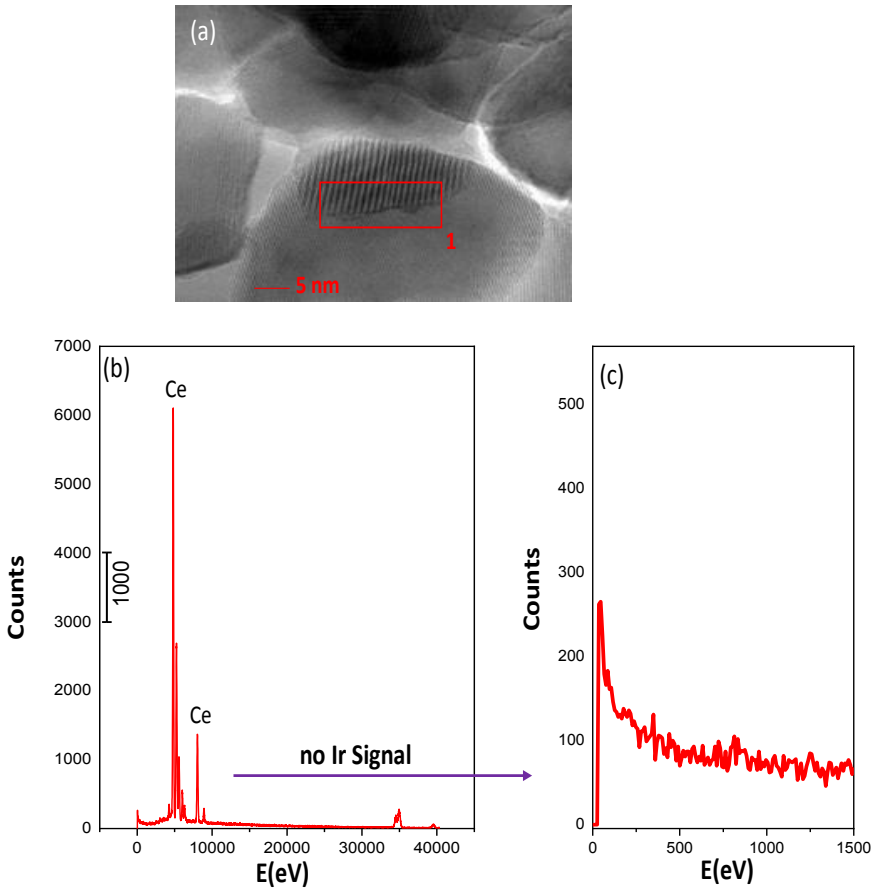

Figure 39. HAADF-TEM image (a) and TEM-EDX spectra (b and c) collected from specified point of 1 wt% $IrCl_3$-CeO_2 annealed in O_2.

In contrast, TEM images of 1 wt% $IrCl_3$-CeO_2 (IWI) sample calcined in air at 800 °C for 5 h presented in Fig. 40-41 and the corresponding EDX data shown in Fig. 42, clearly verifies the presence of detectable and large Ir nanoparticles in very good agreement with the corresponding in-situ FTIR data (Fig. 33c)

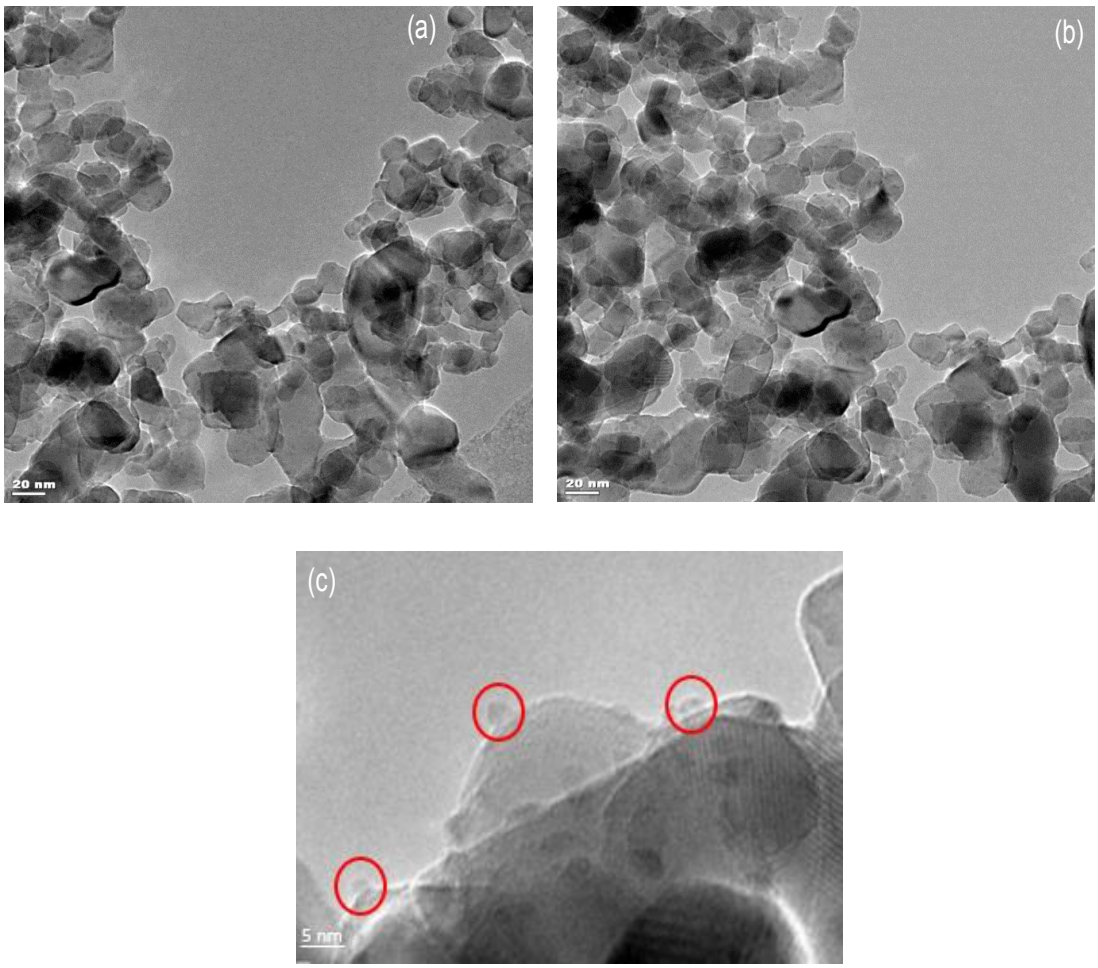

Figure 40. TEM images of 1 wt% $IrCl_3$-CeO_2 (IWI) sample calcined in air at 800 °C for 5 h.

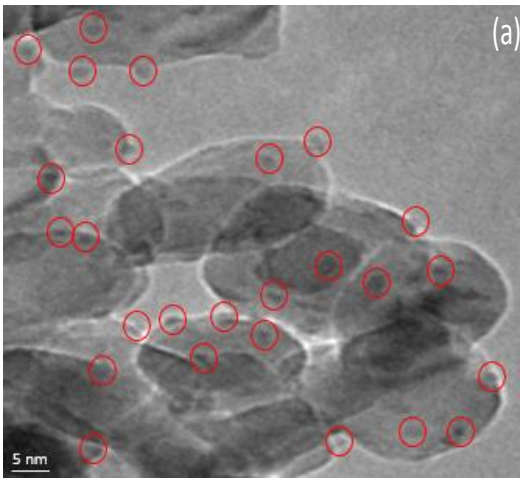

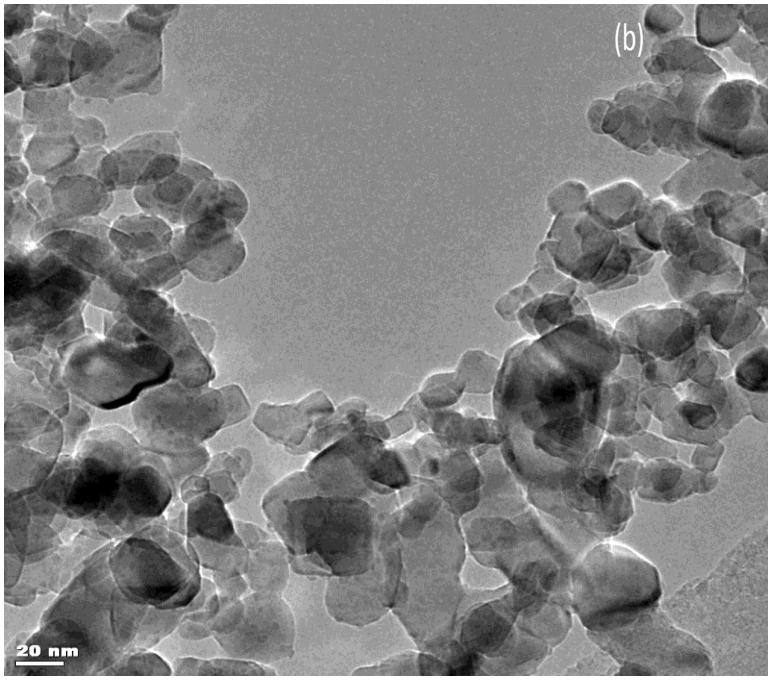

Figure 41. Additional HRTEM images of 1 wt% $IrCl_3$-CeO_2 (IWI) calcined in air at 800 °C for 5 h.

Figure 41 illustrates the presence of highly-dispersed Ir active sites on different parts of metal oxide support.

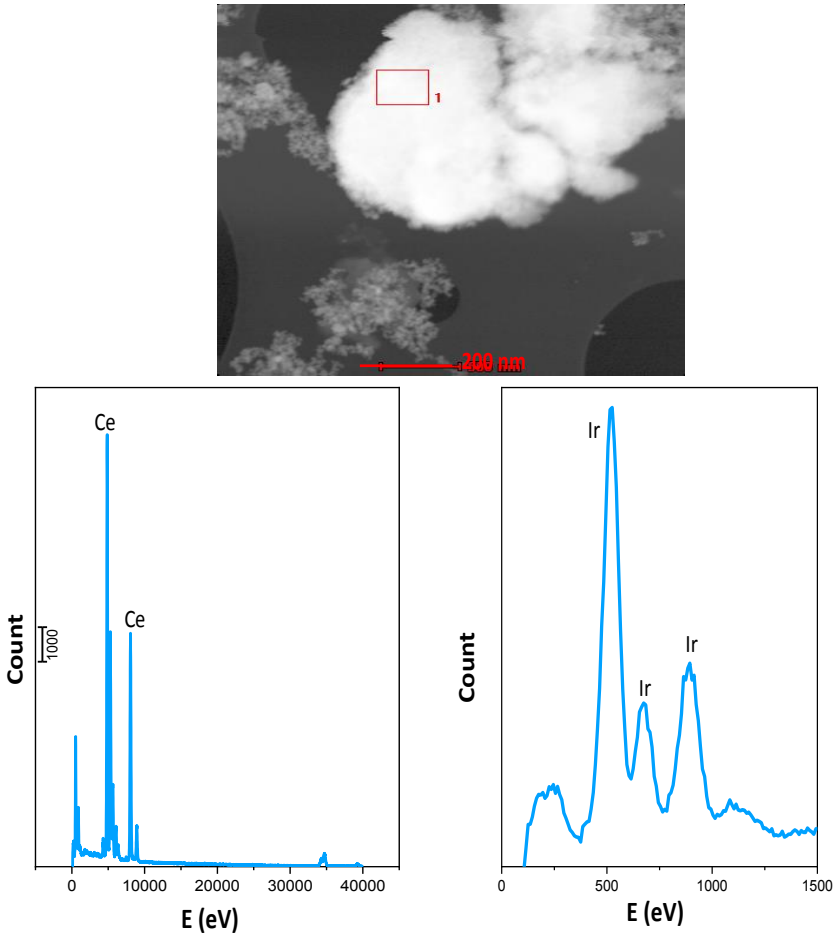

Figure 42. HAADF-TEM image (a) and TEM-EDX spectra (b and c) collected from specified point of 1 wt% $IrCl_3$-CeO_2 calcined in air at 800 °C for 5 h.

TEM images of 1 wt% $IrCl_3$-La/Zr and 1 wt% $IrCl_3$-Ti/Zr (IWI) samples calcined in air at 800 °C for 5 h are presented in Figures 43 and 44 respectively. Fig 43-44 depict Ir active sites which are finely dispersed on La/Zr and Ti/Zr supports.

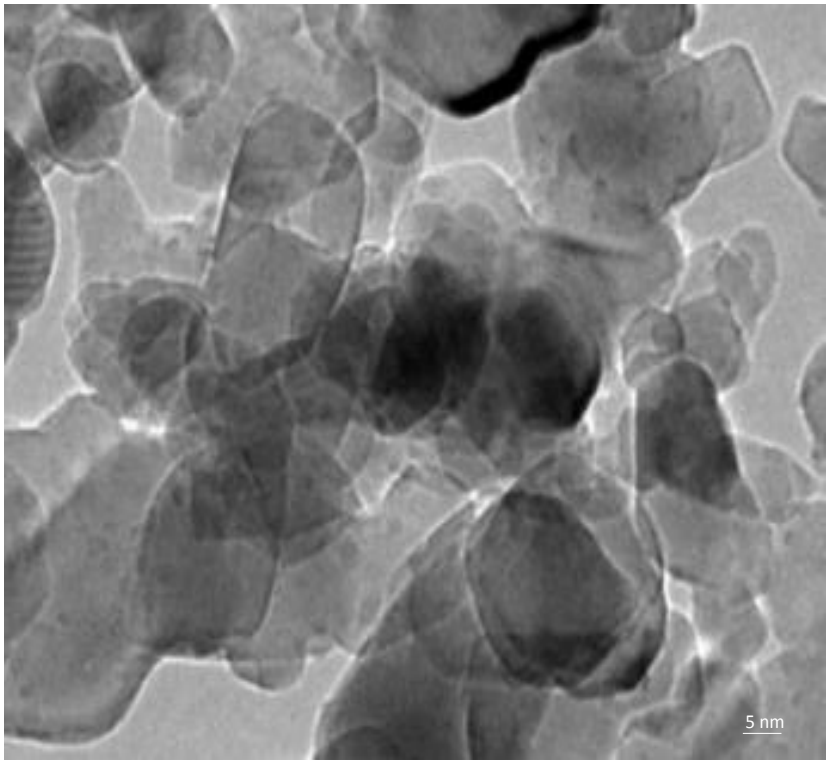

Figure 43. TEM image of 1 wt% $IrCl_3$-La/Zr (IWI) calcined in air at 800 °C for 5 h.

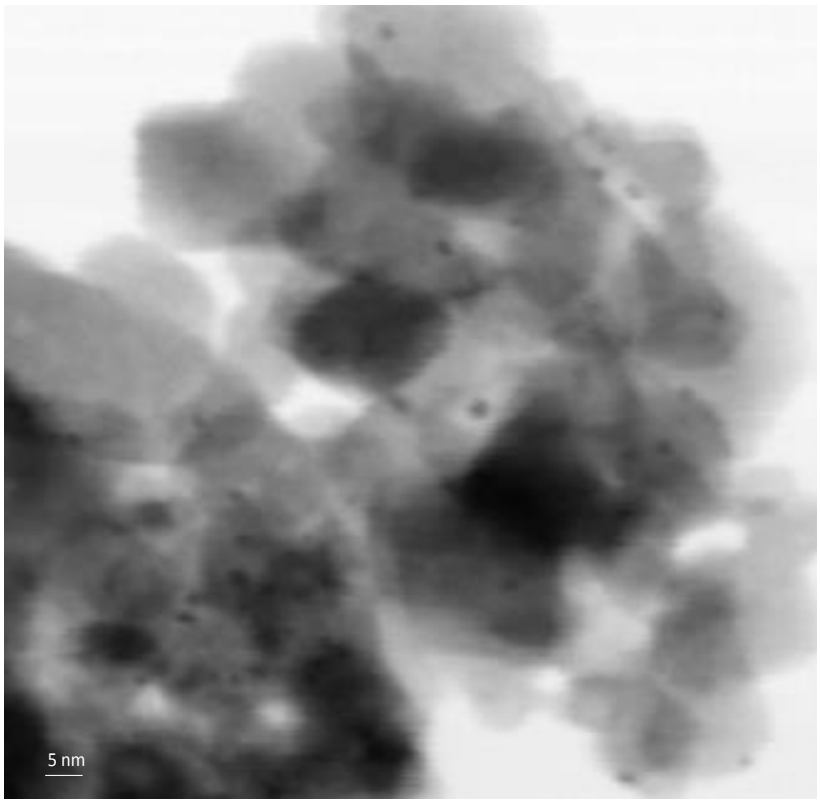

Figure 44. TEM image of 1 wt% $IrCl_3$-Ti/Zr (IWI) calcined in air at 800 °C for 5 h.

3.2.2 XRD

Crystallographic analysis of the investigated catalyst samples was carried out through XRD. Diffraction patterns were assigned using Joint Committee on Powder Diffraction Standards (JCPDS) cards supplied by the International Centre for Diffraction Database (ICDD). Table 12 lists some of the prominent reference phases which were detected in the current XRD data presented in Figures 45-47.

Table 12. Powder diffraction standard card numbers supplied by international database center of the relevant phases detected in the catalytic samples [75-77].

Compound	Phase	JPCD
Ir	Cubic	06-0598
IrO_2	Cubic	58-0335
CeO_2	Cubic	16-4622
TiO_2	Anatase	21-1272
TiO_2	Rutile	04-0551
ZrO_2	Tetragonal	50-1089
ZrO_2	Monoclinic	36-0420
ZrO_2	Cubic	51-1149

Fig. 45 indicates that 1 wt% $IrCl_3$-CeO_2 (IWI) pretreated at different conditions reveal only diffraction features associated with ceria (Fig. 45a) and no XRD peaks associated with metallic Ir or oxidic IrO_x phases are visible (Fig. 45b). This is in good accordance with the aforementioned in-situ FTIR and TEM results suggesting the predominance of small Ir/Ir^{x+} clusters on 1 wt% $IrCl_3$-CeO_2 (IWI). Note that lack of any Ir-related diffraction features for the calcined 1 wt% $IrCl_3$-CeO_2 (IWI) sample (Fig. 45) which showed indications of the existence of larger Ir nanoparticles in the current in-situ FTIR (Fig. 33c) and TEM (Fig. 40-41) results indicate that the large IR nanoparticles are not prominent on the calcined 1 wt% $IrCl_3$-CeO_2 (IWI) sample. Influence of pretreatment conditions on the ceria support material is also presented in Fig. 45c, where calcination in air leads to crystallization and ordering of the ceria phase evident by the narrowing of the corresponding XRD peak for ceria.

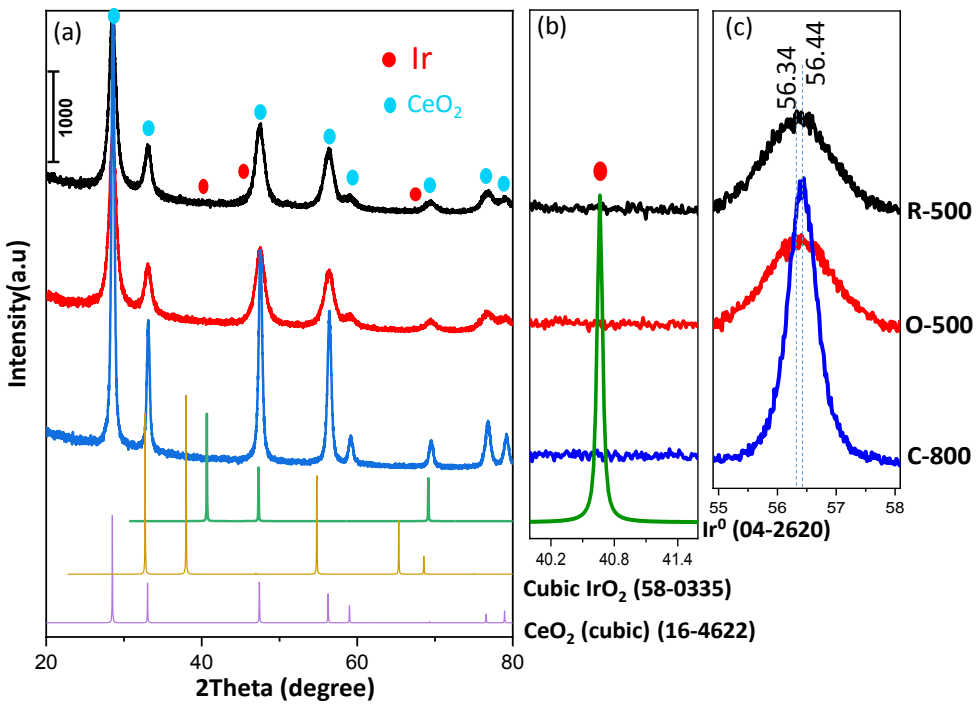

Figure 45. XRD patterns for 1 wt% $IrCl_3$-CeO_2 (IWI) samples. R-500: Reduced in H_2 at 500 °C, O-500: Oxidized in O_2 at 500 °C, C-800: Calcined in air at 800 °C.

XRD analysis of the 1 wt% $IrCl_3$- La_2O_3/ZrO_2 (IWI) samples pretreated under different conditions are given in Fig 46. As in the case of 1 wt% $IrCl_3$-CeO_2 (IWI) sample (Fig. 45), diffraction features that belong to only the support material ($La_2Zr_2O_7$) are visible in Fig. 46 without any indication for the presence of large and ordered Ir or IrO_x phases. Fig. 46c also suggests that difference in pretreatment conditions do not have a significant influence on the crystal structure of the support material unlike ceria (Fig. 45c) which is in good accordance with Raman spectroscopy results. Thus, XRD data for 1 wt% $IrCl_3$- La_2O_3/ZrO_2 (IWI) reveal the predominance of rather small Ir/Ir^{x+} clusters on 1 wt% $IrCl_3$- La_2O_3/ZrO_2 (IWI) where indications for the presence of larger Ir nanoparticles in the in-situ FTIR data probably correspond to minority species.

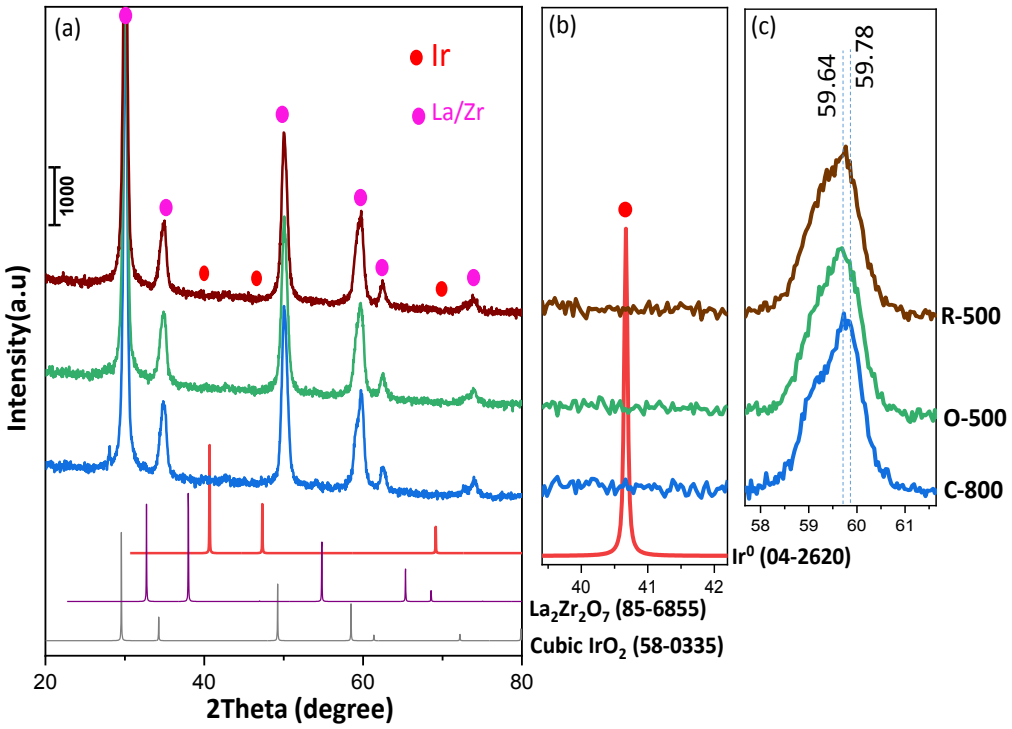

Figure 46. XRD patterns for 1 wt% $IrCl_3$- La_2O_3/ZrO_2 (IWI) samples. R-500: Reduced in H_2 at 500 °C, O-500: Oxidized in O_2 at 500 °C, C-800: Calcined in air at 800 °C.

Fig. 47 presents XRD results for the 1 wt% $IrCl_3$- TiO_2/ZrO_2 (IWI) samples pretreated under different conditions. As can be seen in Fig. 47b, there is no indication of the presence of large Ir/IrO_x nanoparticles on the 1 wt% $IrCl_3$- TiO_2/ZrO_2 (IWI) samples. While the support material exhibits a rather disordered crystal structure for the 1 wt% $IrCl_3$- TiO_2/ZrO_2 (IWI) samples oxidized in O_2 at 500 °C and reduced in H_2 at 500 °C (Fig. 47a), a significant alteration in the support crystal structure is evident after calcination in air at 800 °C leading to the formation of ordered phases. For the 1 wt% $IrCl_3$- TiO_2/ZrO_2 (IWI) catalysts treated at 500 °C, only anatase (TiO_2) diffraction signals are visible. On the other hand, 1 wt% $IrCl_3$- TiO_2/ZrO_2 (IWI) calcined at 800 °C also yields additional ordered phases for tetragonal zirconia (possibly with a minor contribution from monoclinic zirconia) and rutile (TiO_2) [78].

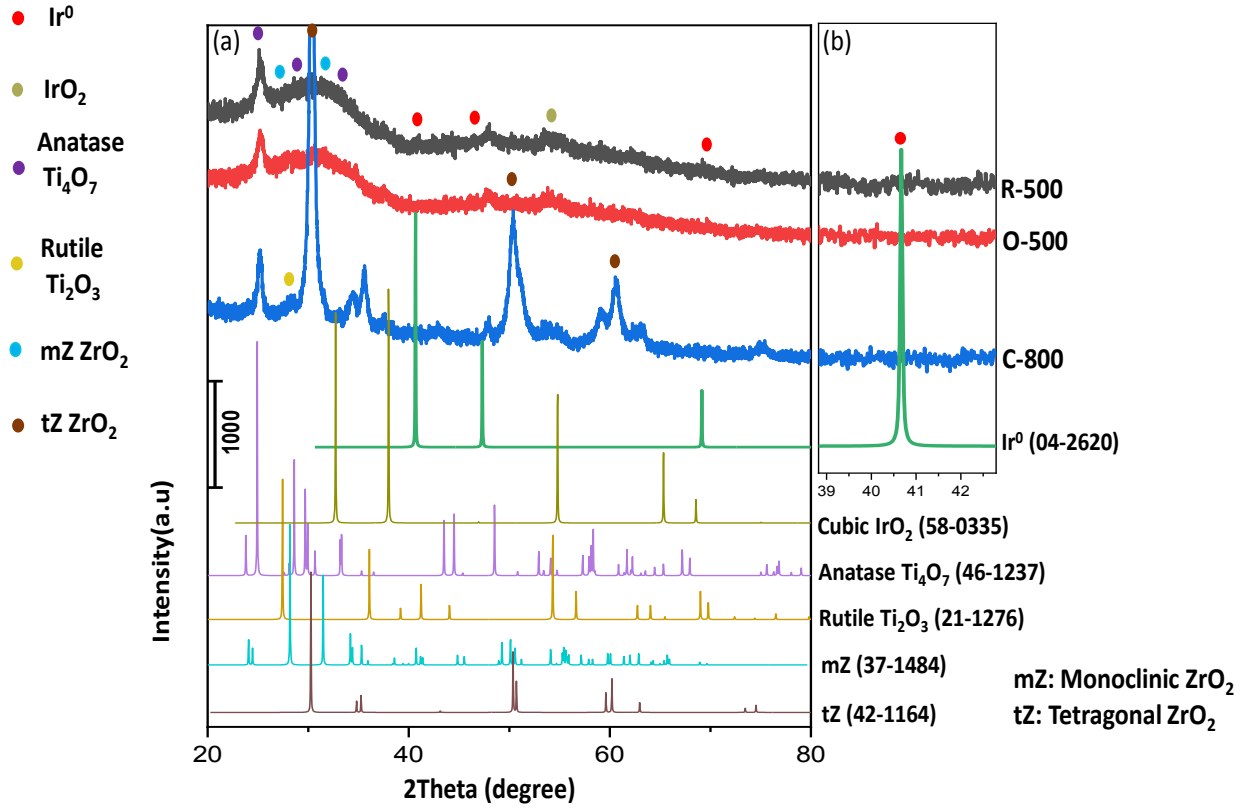

Figure 47. XRD patterns for 1 wt% $IrCl_3$- TiO_2/ZrO_2 (IWI) samples. R-500: Reduced in H_2 at 500 °C, O-500: Oxidized in O_2 at 500 °C, C-800: Calcined in air at 800 °C.

3.2.3 RAMAN spectroscopy

Raman spectroscopy may provide insight on the weak interactions between metal catalysts and support species, and also the effect of pretreatment conditions on the catalyst structure [79]. Thus, Raman spectroscopy measurements were carried out on the synthesized catalysts. Some of the possible species that are relevant to the Raman spectroscopic analysis of the $IrCl_3$-CeO_2 (IWI) catalysts are listed in Table 13.

Table 13. Some of the possible species relevant to the Raman spectroscopic analysis of the $IrCl_3$-CeO_2 (IWI) catalysts [79-81].

Vibrational Mode	**Wavenumber (cm^{-1})**
CeO_2	157-164
CeO_2 (Longitudinal Stretching)	237-245
CeO_2 (Symmetric Stretching)	454-463
IrO_2	646-681
Peroxide	821-832
O-O Stretching	855-863
Superoxide	1141-1170
Carbon Contamination	1539-1565
Gas Phase O_2	1628-1699

Typical Raman spectra for CeO_2 acquired at different temperatures are shown in Fig. 48 [70]. In light of the literature data (Fig. 48 and Table 13) we can discuss the features in the Raman spectra in Fig 49-50 corresponding to the 1 wt% $IrCl_3$-CeO_2 (IWI) [79-81]. In Fig. 48, we can see Raman shifts at 162 and 248 cm^{-1} that are related to rutile and longitudinal stretching modes of ceria support, respectively [80]. Shift of the bands at 157 and 242 cm^{-1} to lower wavenumbers (Fig. 49) for reduced sample is due to the generation of oxygen vacancies and formation of Ce^{+3} ions which expand the ceria lattice [81].

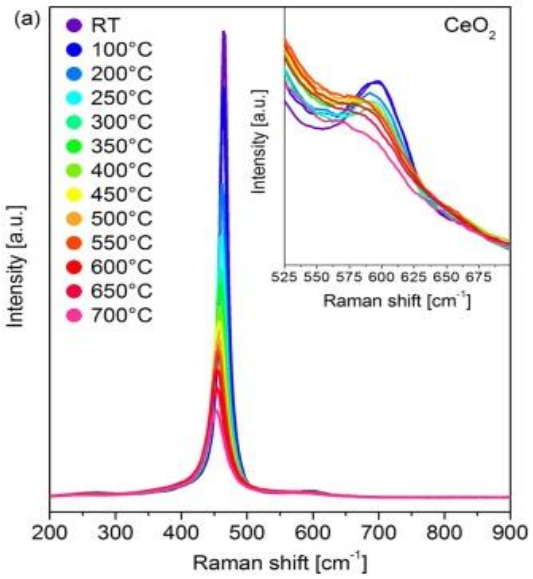

Figure 48. Typical Raman spectra of thermally treated ceria support [82].

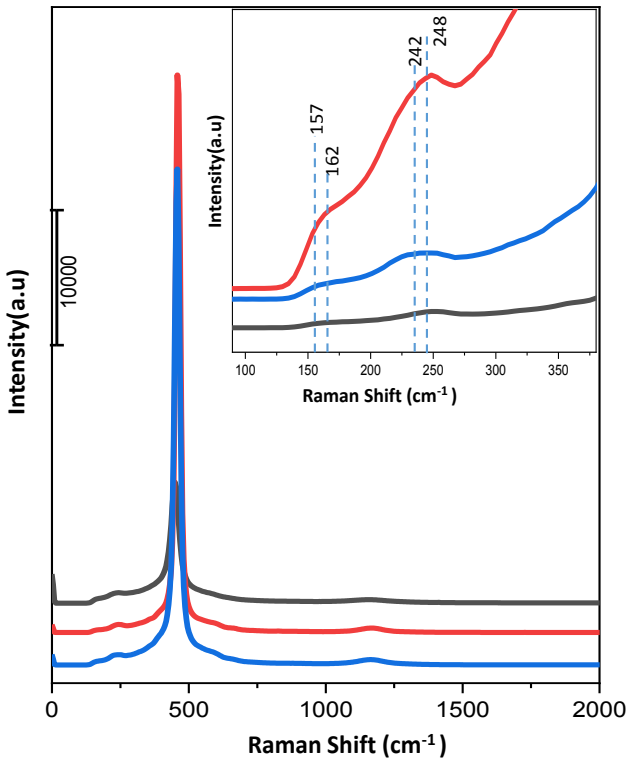

Figure 49. Overall Raman spectra of 1 wt% $IrCl_3$-CeO_2 (IWI) samples. R-500: Reduced in H_2 at 500 °C, O-500: Oxidized in O_2 at 500 °C, C-800: Calcined in air at 800 °C.

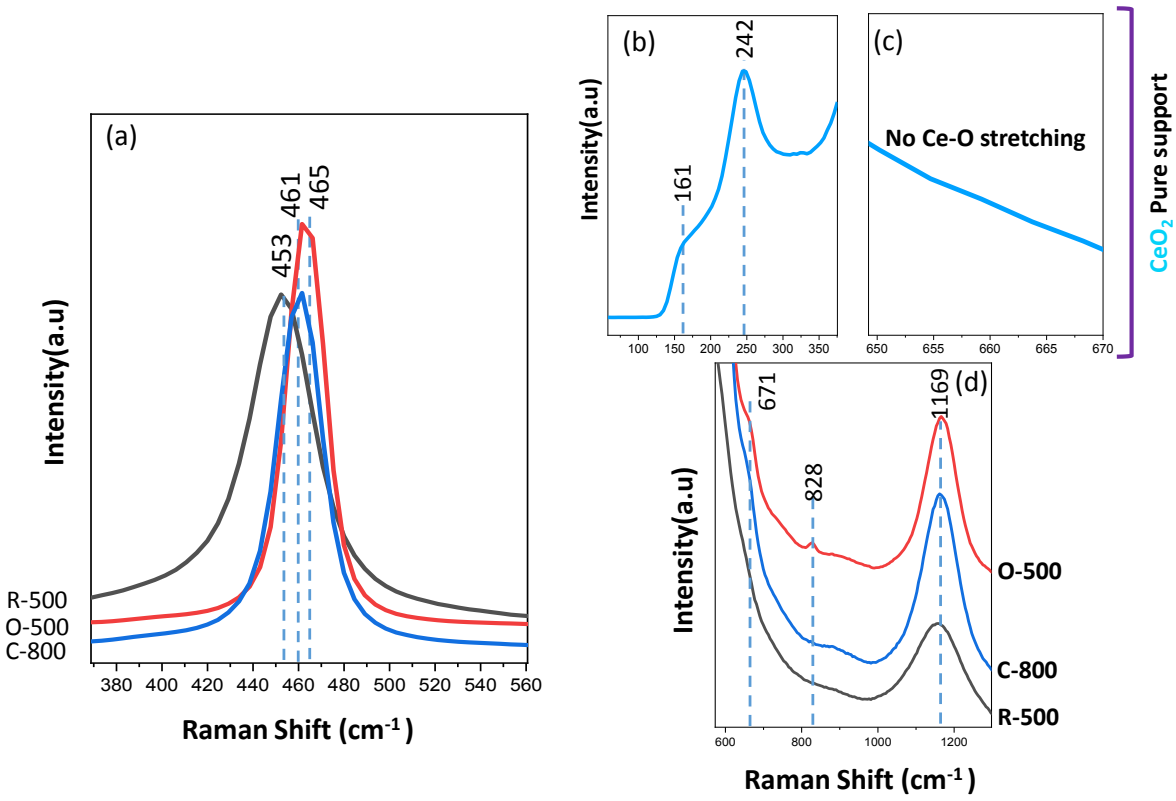

Figure 50. Detailed Raman spectra of 1 wt% $IrCl_3$-CeO_2 (IWI) samples. R-500: Reduced in H_2 at 500 °C, O-500: Oxidized in O_2 at 500 °C, C-800: Calcined in air at 800 °C.

The major signal located at 461 cm^{-1} in Fig. 50a is due to the well-known F_{2g} vibrational mode of fluorite structure related to cubic lattice [80]. Shift of this particular band to lower wavenumbers (Fig. 50a) for reduced samples is due to the generation of oxygen vacancies and Ce^{+3} ions. Figure 50b shows the bands at 161 and 242 cm^{-1} associated with the stretching modes of the top most Ce-O layer of ceria and are not related to Ir species [79]. 671 cm^{-1} (Fig. 50d) is linked to the interaction of Ir sites with oxygen species. This feature is more intense in the case of oxidized samples that could not be detected in pure ceria support lacking any Ir species (Fig. 50c) [78]. 828 cm^{-1} band (Fig. 50d) can be assigned to peroxide features generated upon adsorption of molecular O_2 on ceria [81]. 1169 cm^{-1} band (Fig. 50d) can be ascribed to superoxide species which is more intense in the case of oxidized species and results second order Raman feature through mixing of A_{1g}, E_g and F_{2g} ceria modes and confirms the presence of Ce^{4+} ions as majority species [80].

Along these lines, $IrCl_3$-La_2O_3/ZrO_2 catalysts were also investigated via Raman spectroscopy. Some of the possible species that are relevant to the Raman spectroscopic analysis of the $IrCl_3$-La_2O_3/ZrO_2 (IWI) catalysts are listed in Table 14.

Table 14. Some of the possible species relevant to the Raman spectroscopic analysis of the $IrCl_3$-La_2O_3/ZrO_2 (IWI) samples [83-85].

ZrO_2	**ZrO_2**	**ZrO_2**	**ZrO_2**	**ZrO_4^{4-}**	**La_2O_3**
Pure	**Tetragonal**	**Monoclinic**	**Cubic**	**Tetra-oxo-complex**	**Pure**
475	142	304	142	750	181
560	256	340	256		401
630	320	376	466		
690	466	477	628		
750	637	638			

Further literature results regarding the Raman spectroscopy of the $IrCl_3$-La_2O_3/ZrO_2 (IWI) catalysts can be seen in Fig. 51.

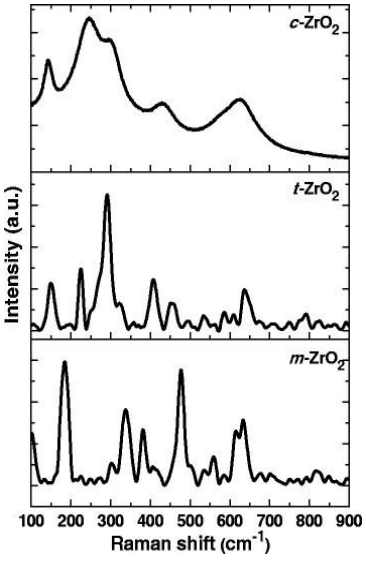

c-Zr (cubic): dominant at lower T (25-1200 °C)
major bands: 256 and 628 cm^{-1}

t-Zr (tetragonal): dominant at moderate T (1200-2400 °C)
major bands: 142, 256, 466, 627 cm^{-1}

m-Zr (monoclinic): dominant at elevated T (>2400 °C)
major bands: 477 and 638 cm^{-1}

Figure 49. Raman patterns of different phases of zirconia [84].

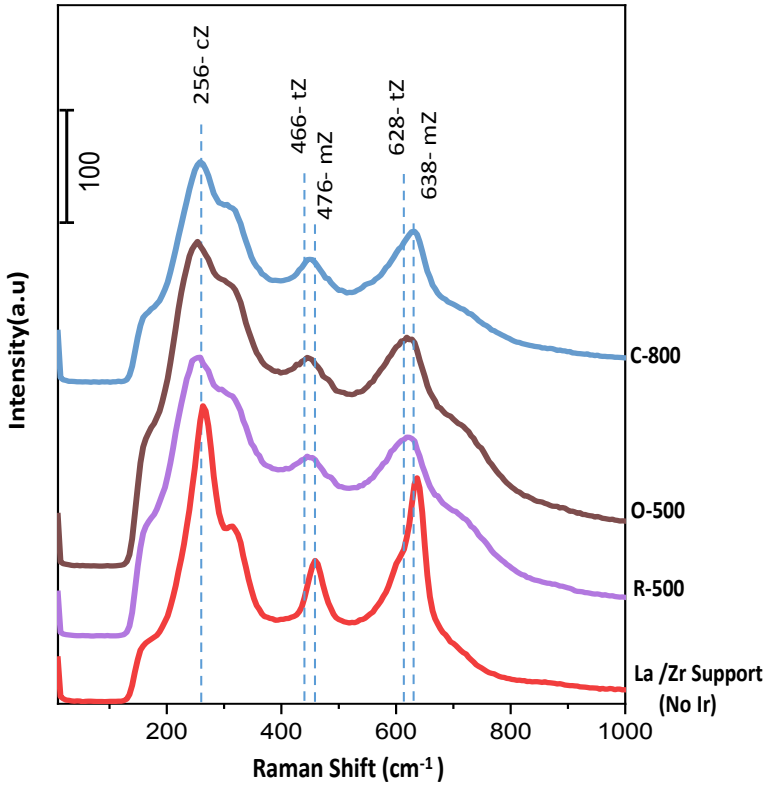

Figure 52. Raman spectra of 1 wt% $IrCl_3$-La_2O_3/ZrO_2 (IWI) samples. R-500: Reduced in H_2 at 500 °C, O-500: Oxidized in O_2 at 500 °C, C-800: Calcined in air at 800 °C.

As the majority (91%) of the La_2O_3/ZrO_2 support material belongs to zirconia, the prominent Raman features in Fig. 52 corresponding to the 1 wt% $IrCl_3$-La_2O_3/ZrO_2 catalyst are due to zirconia. Fig. 52 indicates that pristine La_2O_3/ZrO_2 support material which lacks Ir, has predominantly monoclinic and cubic zirconia features while pretreatment of the 1 wt% $IrCl_3$-La_2O_3/ZrO_2 catalyst at 500 °C in H_2 or O_2 or calcination in air at 800 °C leads to the formation of tetragonal zirconia as an additional phase [83-85].

Table 15 summarizes some of the possible species that are relevant to the Raman spectroscopic analysis of the $IrCl_3$- TiO_2/ZrO_2 (IWI) samples.

Table 15. Some of the possible species relevant to the Raman spectroscopic analysis of the $IrCl_3$- TiO_2/ZrO_2 (IWI) samples [86-88].

TiO_2	TiO_2	ZrO_2	ZrO_2	ZrO_2	ZrO_2	ZrO_4^{4-}	$ZrTiO_4$
Anatase	**Rutile**	**Monoclinic**	**Tetragonal**	**Cubic**	**Pure**	**Tetra-oxo-complex**	**Orthorhombic**
144	144	304	142	142	475	750	135
197	447	340	256	256	560		259
312	612	376	320	466	630		320
399	826	477	466	628	690		391
518		638	637		750		622
638							778

Fig. 53 shows typical Raman features for anatase and rutile phases of titania.

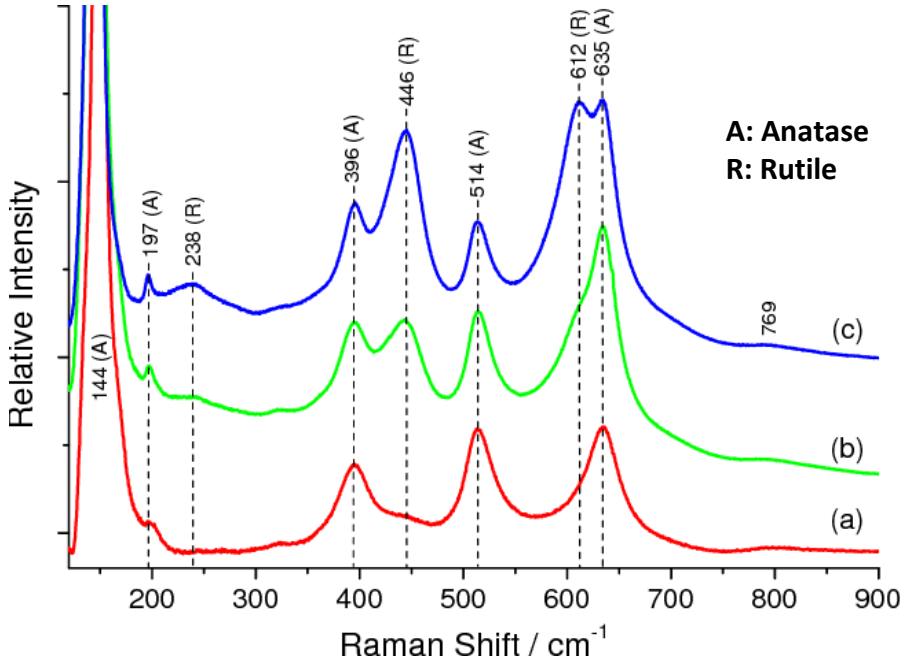

Figure 53. Typical Raman spectra of anatase and rutile phases of titania. [86]

Raman spectra of the 1wt% $IrCl_3$-TiO_2/ZrO_2 (IWI) pretreated under different treatment conditions and the pristine TiO_2/ZrO_2 support (without Ir) are presented in Fig. 54. It is apparent in Fig. 54 that the pristine TiO_2/ZrO_2 support exhibits monoclinic zirconia and anatase titania phases [87]. Pretreatment of the 1 wt% $IrCl_3$-TiO_2/ZrO_2 (IWI) catalyst at 500 °C in H_2 or O_2 or calcination in air at 800 °C results in the broadening and attenuation of the anatase phase and formation of a shoulder at ca. 450 cm^{-1} consistent with the initiation of the anatase to rutile phase transition of the titania domains in the support material. Furthermore, high temperature treatments also lead to the formation of tetragonal zirconia phase [88].

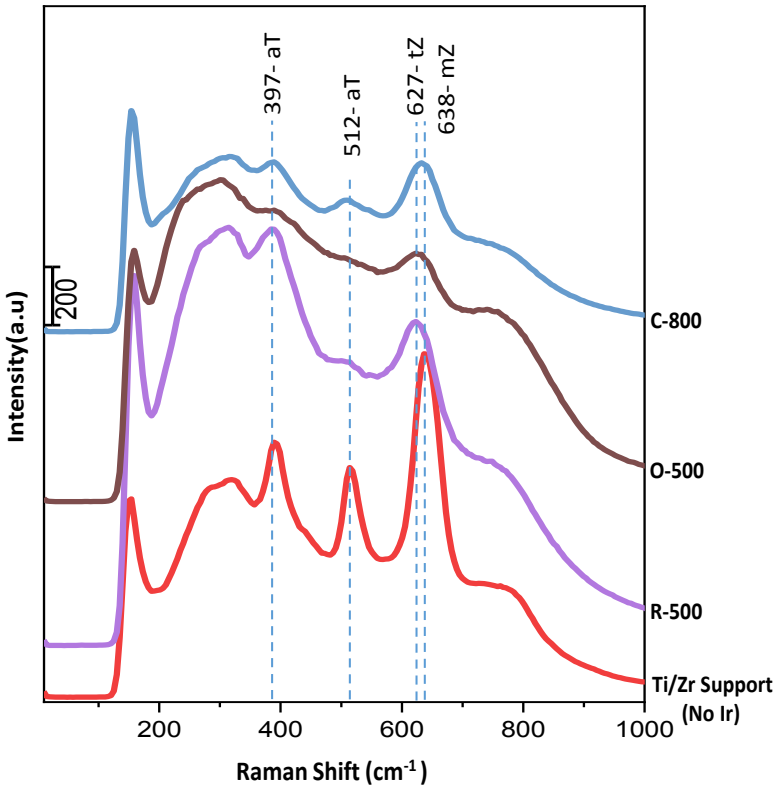

Figure 54. Raman spectra of 1 wt% $IrCl_3$- TiO_2/ZrO_2 (IWI) samples. R-500: Reduced in H_2 at 500 °C, O-500: Oxidized in O_2 at 500 °C, C-800: Calcined in air at 800 °C.

3.2.4 XPS

XPS analysis of the investigated catalyst samples were also carried out in order to obtain more insight into the oxidation state of the Ir sites and the metal oxide support materials. Fig. 55 shows Ir4f XPS data from the literature summarizing typical XPS binding energy (B.E.) values for some of the common oxidation states of Ir.

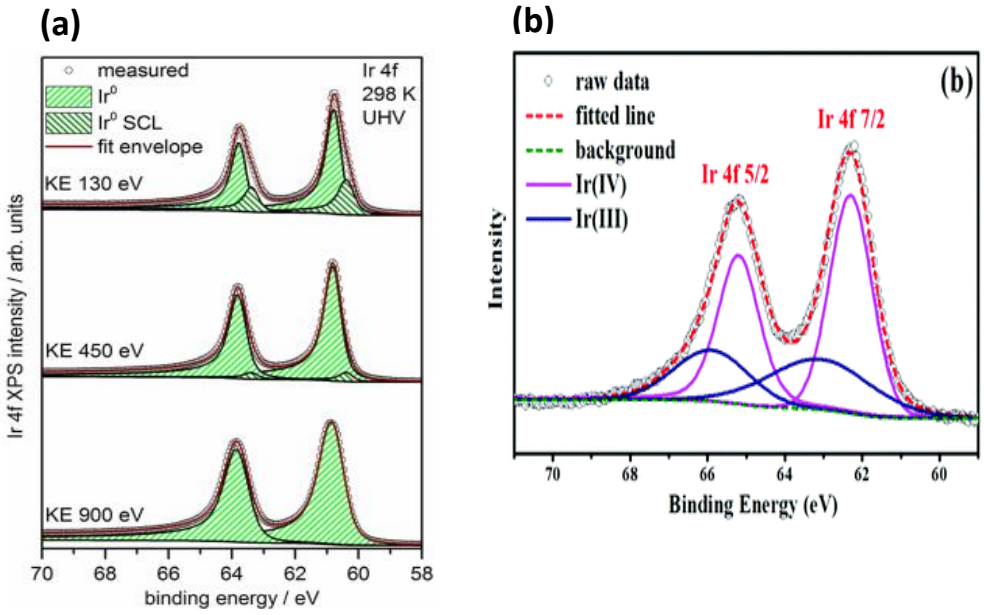

Figure 55. Ir4f XPS spectra for some of the common Ir oxidation states [89], [90].

Ir 4f XPS spectra given in Fig 55 shows that 60.9 and 63.8 eV bands are related to the metallic Ir, 63.1 and 66.2 eV, are related to the Ir^{3+} species, and 62.4 and 65.5 eV are related to Ir^{4+} species [91-93].

XPS results for 1 wt% $IrCl_3$-CeO_2 (IWI) samples annealed in H_2 and O_2 at 500 °C, and calcined at 800 °C are presented below.

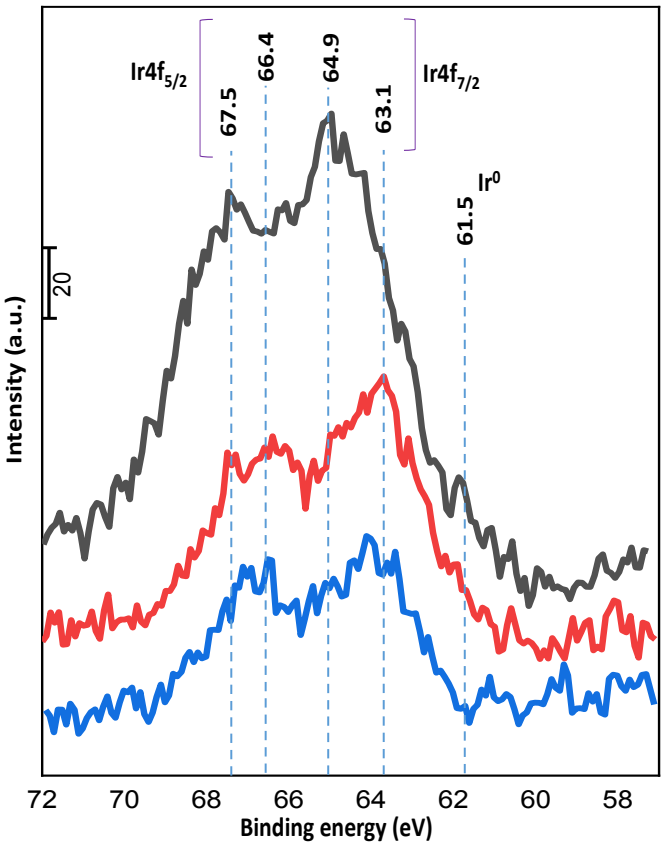

Figure 56. Ir4f XPS spectra for 1 wt% $IrCl_3$-CeO_2 (IWI) samples. R-500: Reduced in H_2 at 500 °C, O-500: Oxidized in O_2 at 500 °C, C-800: Calcined in air at 800 °C.

In Fig. 56, 61.5 eV band that is detected in reduced sample, can be related to metallic iridium. 63.1 and 66.4 eV bands are due to the presence of highly oxidized Ir species (Ir^{4+}) while the 64.9 and 67.5 eV bands are related to Ir^{3+}.

Fig. 57 presents typical Ce3d XPS spectra for some of the common Ce oxidation states. [94], [95].

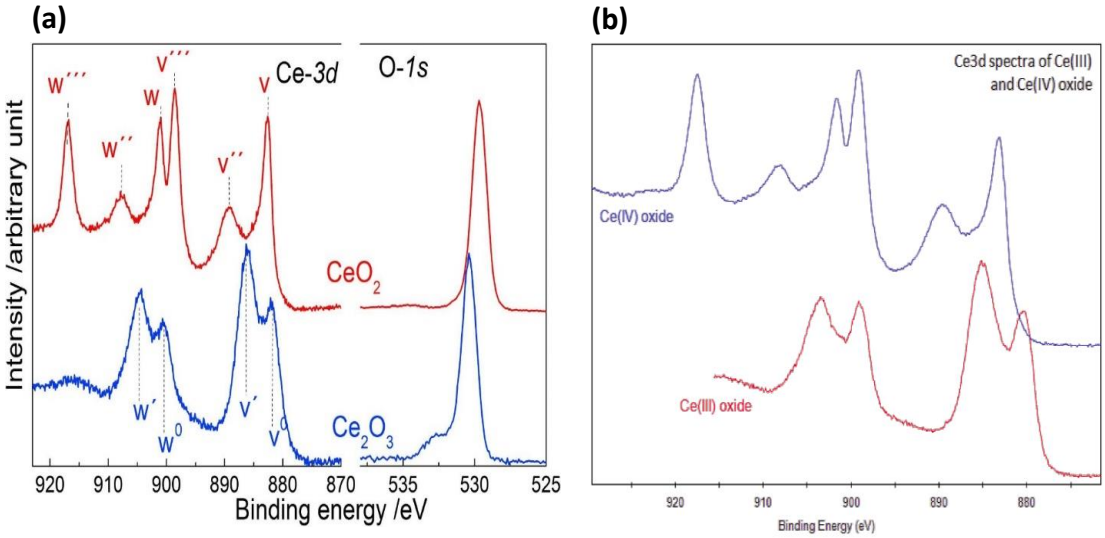

Figure 57. Ce3d XPS spectra for some of the common Ce oxidation states. [94], [95].

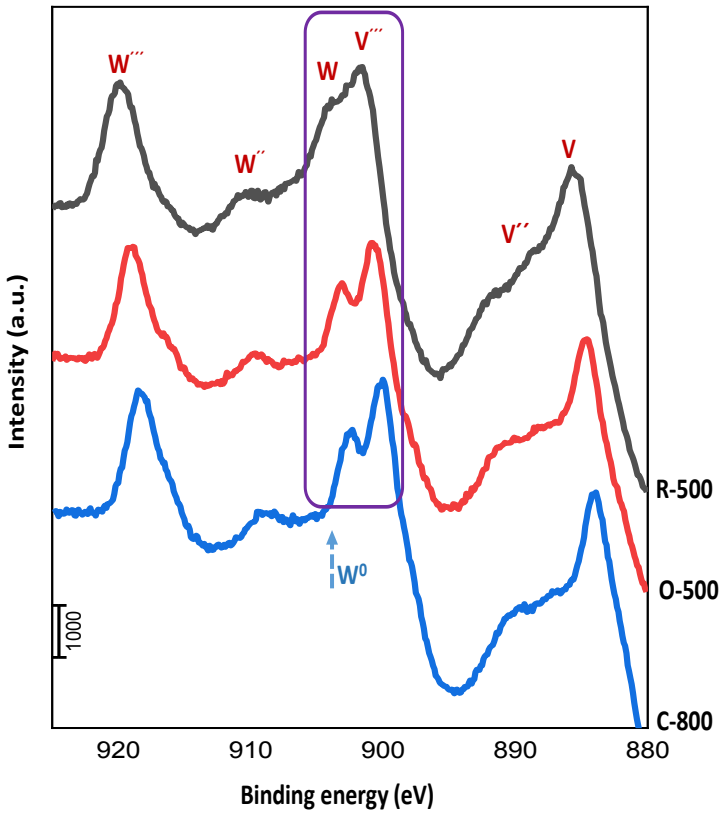

Figure 58. Ce3d XPS spectra for 1 wt% $IrCl_3$-CeO_2 (IWI) samples. R-500: Reduced in H_2 at 500 °C, O-500: Oxidized in O_2 at 500 °C, C-800: Calcined in air at 800 °C.

Based on the reference Ce3d XPS spectra given in Fig. 57, Ce3d XPS spectra of the 1 wt% $IrCl_3$-CeO_2, (IWI) catalyst (Fig. 58) can be analyzed. Peaks labeled with red letters in Fig. 58 are related to the Ce^{4+} ions, and the peak labeled with the blue letter is due to Ce^{3+} ions. The presence of Ce^{4+} species as the majority species in the oxidized cases is clear and in the reduced sample, broadening of v´´´ and w bands due to appearance of w° band is obvious, which confirms the presence of Ce^{3+} ions.

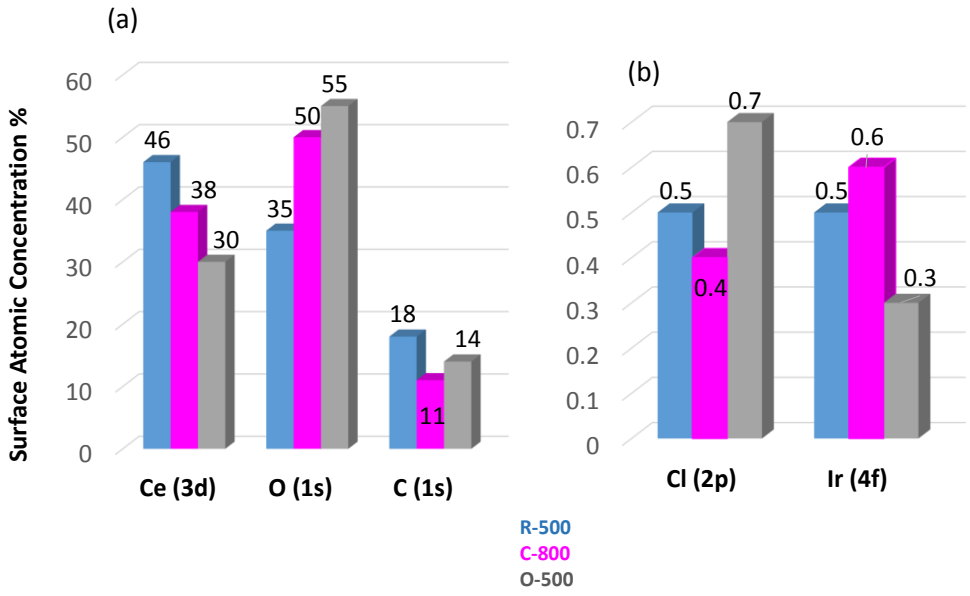

Figure 59. Surface atomic concentration analysis of 1 wt% $IrCl_3$-CeO_2 (IWI) samples via XPS after different types of treatments. R-500: Reduced in H_2 at 500 °C, O-500: Oxidized in O_2 at 500 °C, C-800: Calcined in air at 800 °C.

Figure 59 shows the surface atomic composition of the 1 wt% $IrCl_3$-CeO_2 (IWI) samples via XPS after different types of treatments. It can be seen in Fig. 59a that the reduced sample has the highest Ce and the lowest O surface atom concentration evident by the removal of oxide ions from the surface due to their reaction with hydrogen. As the oxygen content of the pretreatment conditions increases from calcination in air to annealing in 20% O_2, oxygen content of the surface increases concomitant to a decrease in Ce concentration. Carbon content was mostly comparable in all pretreatment cases. Furthermore, Fig. 59b indicates that while surface Ir concentrations after oxidizing treatments are comparable, reducing treatment leads to a lower surface Ir concentration.

La3d XPS data for the typical La species is illustrated in Fig. 60 [96]. In light of these results, we can investigate the corresponding XPS data for the 1 wt% $IrCl_3$-La_2O_3/ZrO_2 (IWI) samples treated under different conditions (Fig. 61). It is evident in Fig. 61 that La3d features for all of the investigated samples are broad and convoluted indicating the presence of multiple La species. The prominently lower La3d B.E. shift in the reduced sample is consistent with the presence of $La(OH)_3$ on this sample surface (in addition to La_2O_3). On the other hand, significant high B.E. shift for La3d features and the well resolved peak at 840.1 eV in the case of calcination in air suggests the formation of $La_2(CO_3)_3$ species in addition to $La(OH)_3$ and La_2O_3.

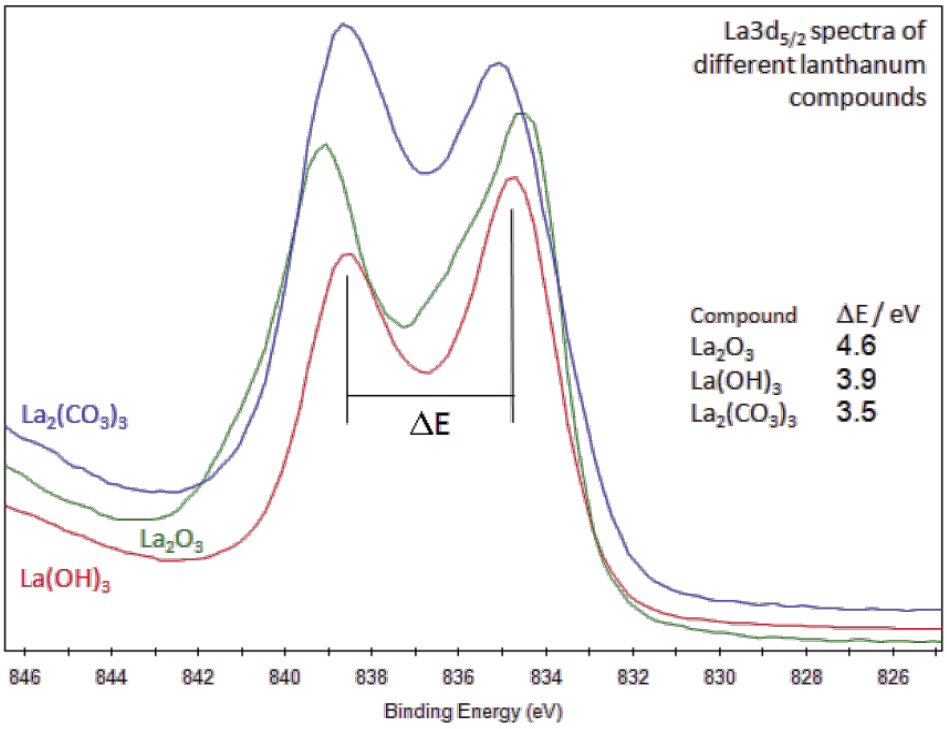

Figure 60. Reference La3d XPS spectra for various La compounds [96].

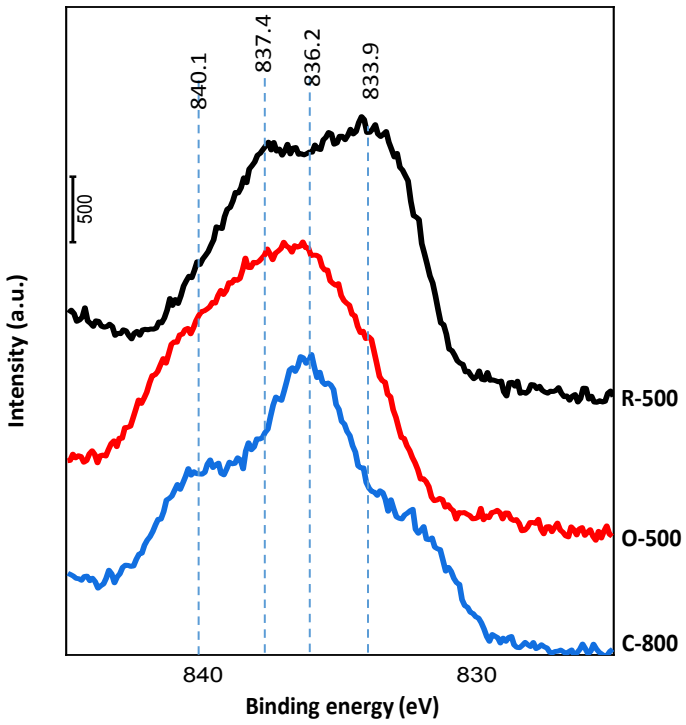

Figure 61. La3d XPS spectra for 1 wt% $IrCl_3$-CeO_2 (IWI) samples. R-500: Reduced in H_2 at 500 °C, O-500: Oxidized in O_2 at 500 °C, C-800: Calcined in air at 800 °C.

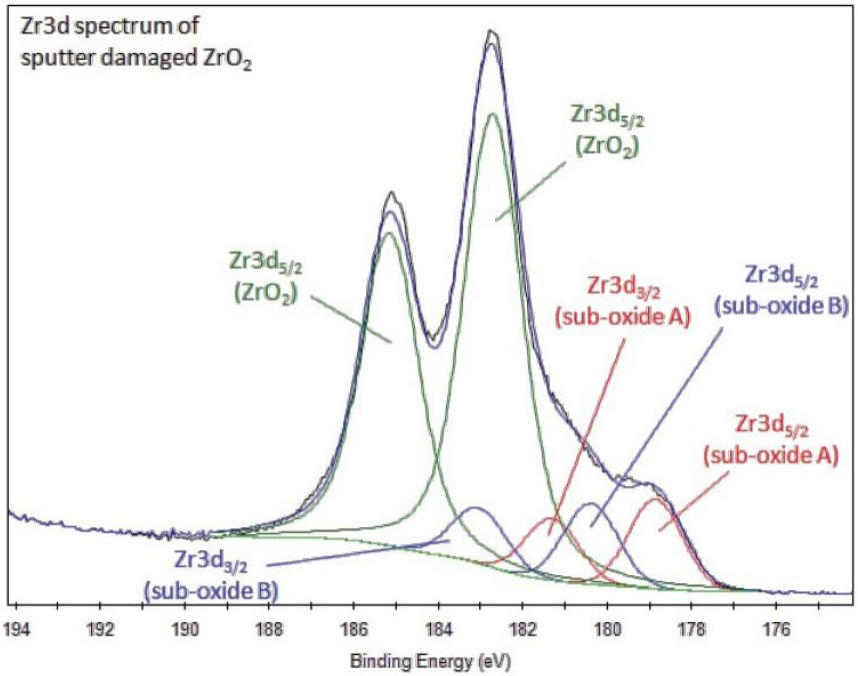

Figure 62. Reference Zr3d XPS spectra for sputtered (defective) ZrO_2 surface [97].

Typical Zr3d features of a defective ZrO_2 surface is given in Fig. 62 reflecting a variety of different Zr^{x+} states. [97]. Zr3d XPS data for XPS data for the 1 wt% $IrCl_3$-La_2O_3/ZrO_2 (IWI) samples are given in Fig. 63. While the Zr3d signal positions were comparable for the calcined and reduced samples, a blueshift was observed for the sample annealed in oxygen revealing a more oxidizing chemical environment around the Zr^{4+} ions for the latter catalyst.

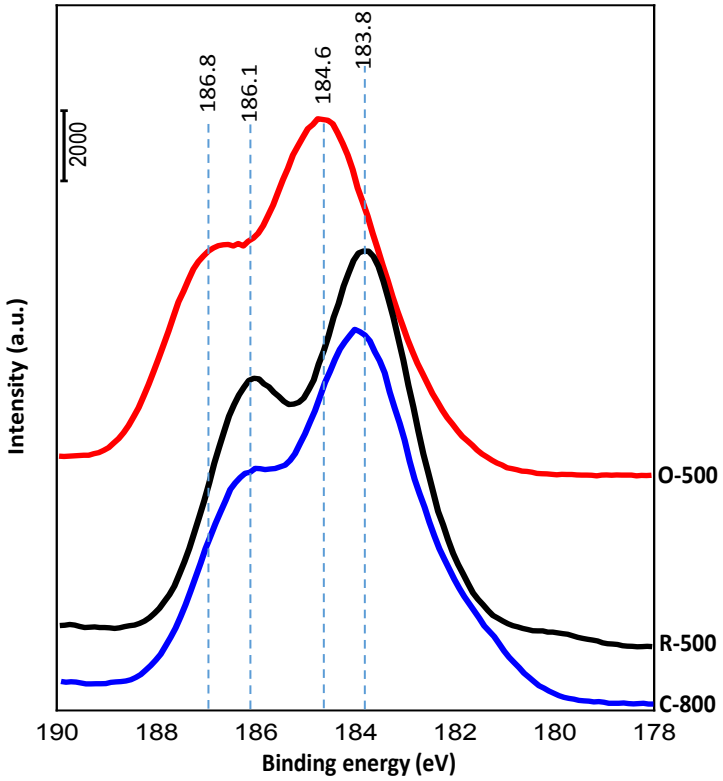

Figure 63. Zr3d XPS spectra for 1 wt% $IrCl_3$-CeO_2 (IWI) samples. R-500: Reduced in H_2 at 500 °C, O-500: Oxidized in O_2 at 500 °C, C-800: Calcined in air at 800 °C.

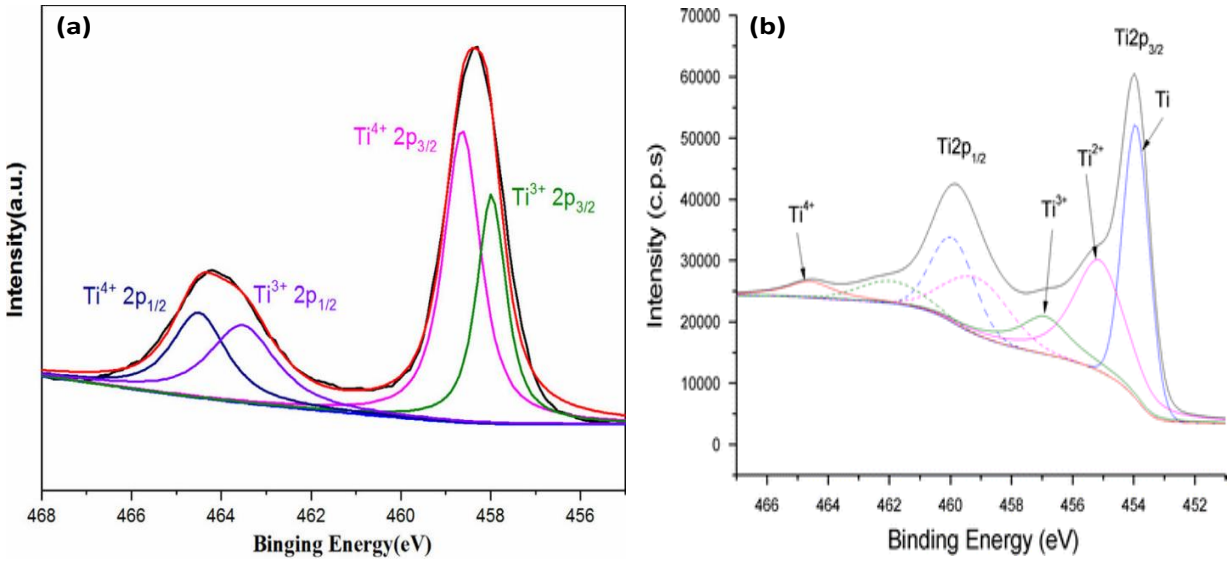

Figure 64. Reference Ti2p XPS spectra for various Ti oxidation states [98], [99].

With the help of the reference Ti2p XPS data given in Fig. 64, we can explore the corresponding Ti2p XPS spectra for the 1 wt% $IrCl_3$-TiO_2/ZrO_2 samples given in Fig. 65. While the broadest Ti2p features are observed for the reduced sample consistent with the formation of Ti^{3+} species, Ti2p signals sharpen under oxidizing conditions indicating decreasing number of Ti^{3+} species and increasing number of fully oxidized Ti^{4+} species.

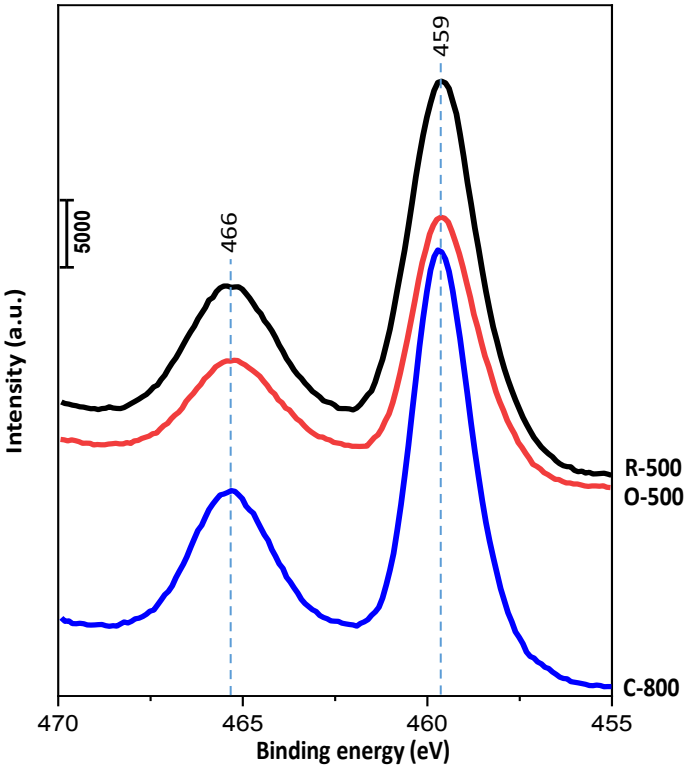

Figure 65. Ti2p XPS spectra for 1 wt% $IrCl_3$-CeO_2 (IWI) samples. R-500: Reduced in H_2 at 500 °C, O-500: Oxidized in O_2 at 500 °C, C-800: Calcined in air at 800 °C.

3.2.5 BET

For each family of samples, specific surface area (SSA), pore volume, and pore size for the pristine support, as well as the 1 wt.% Ir loaded IWI catalysts with different supports annealed in H_2 at 500 °C, calcined at 800 °C, and annealed in O_2 at 500 °C were measured via 12-point BET technique to investigate the effect of different treatment conditions on these parameters.

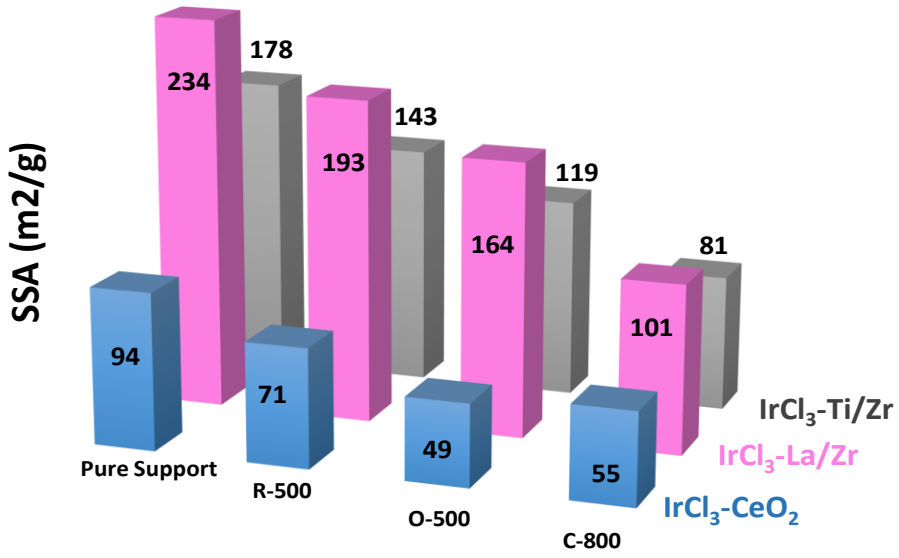

Figure 66. Specific surface area (SSA) of three different family of samples prepared via IWI method and treated under three different conditions. R-500: Reduced in H_2 at 500 °C, O-500: Oxidized in O_2 at 500 °C, C-800: Calcined in air at 800 °C.

Figure 66 shows that the pristine support materials have the highest SSA values and Ir deposition decreases the SSA in all cases, due to blocking of the pores of the support lattice by Ir species [100]. SSA values of the pristine support materials can ranked in the following increasing order: CeO_2 < TiO_2/ZrO_2 < La_2O_3/ZrO_2. For all of the Ir containing samples, typically reduction in hydrogen yields the highest SSA, followed by annealing in 20% O_2, and calcination in air.

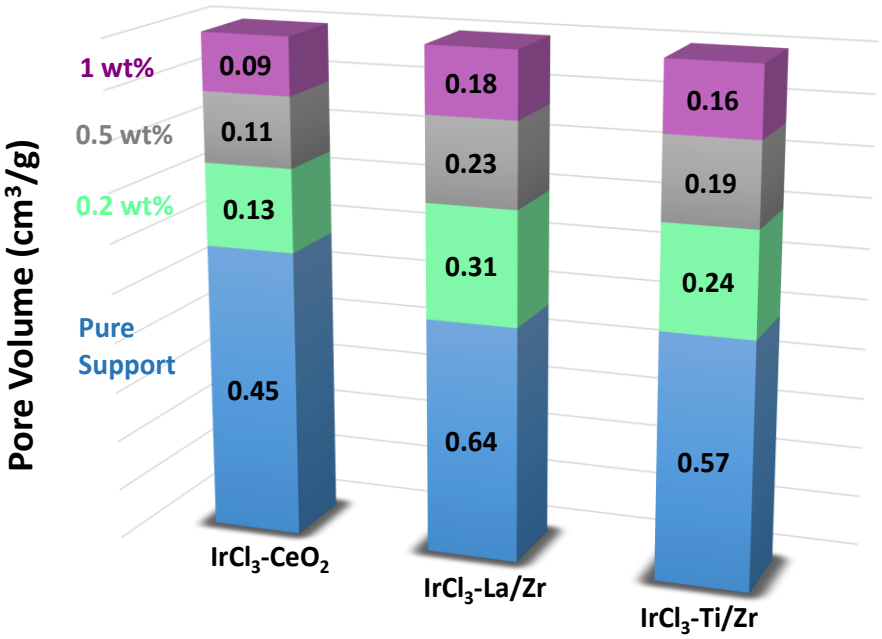

Figure 67. Average pore volume of three different family of samples with three different metal loading (0.2, 0.5, and 1 wt%-IWI) reduced in H_2 at 500 °C for 2 h.

Figure 67 confirms experimentally that due to infusion of metal particles into the pores of the supports, doping metal onto the pure support can diminish the pore volume distribution.

Fig. 68 presents the effect of similar parameters on the pore sizes of the investigated materials. As expected, average pore sizes given in Fig. 68 reveal an inverse trend as compared to the SSA values illustrated in Fig. 66. In other words, higher SSA values are accompanied with smaller pore sizes.

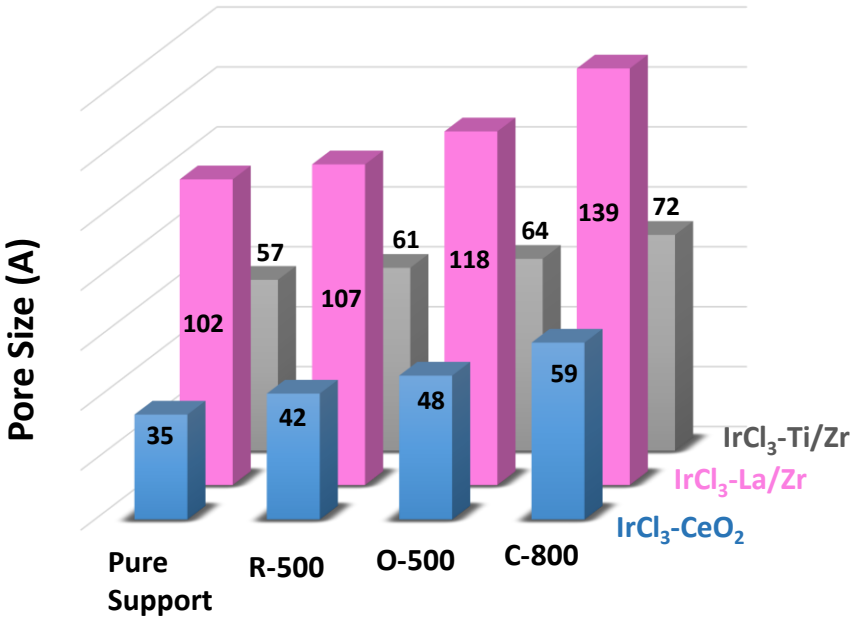

Figure 68. Average pore size of three different family of samples (1 wt%-IWI) under different treatment conditions. R-500: Reduced in H_2 at 500 °C, O-500: Oxidized in O_2 at 500 °C, C-800: Calcined in air at 800 °C.

4. CONCLUSIONS

In this work, we synthesized low metal loading (0.2 and 0.5 wt%) active Ir catalysts that have comparable catalytic performance in CO oxidation with of higher metal loading (1 wt%) ones. The importance of highly-dispersed active sites with sub-nanometer diameters to synthesize extremely low metal loading active catalysts were confirmed by functional and characterization techniques. Magnesium oxide (MgO), ceria (CeO_2), lanthana-zirconia (La_2O_3–ZrO_2) and titania-zirconia (TiO_2–ZrO_2) support materials were utilized in the catalyst synthesis.

In addition, effect of the catalyst pre-treatment conditions (e.g., reduction in H_2, oxidation in O_2, and calcination in air) on the catalyst structure and performance was investigated in detail. Our results indicate that on some of the investigated support materials, high-dispersion Ir sites can be generated where Ir exists as small clusters with < 1 nm particle size. On the other hand, these small Ir clusters are often accompanied by the presence of larger Ir nanoparticles as well. Moreover, catalyst pretreatment conditions revealed noticeable alterations in the catalyst structure in terms of average support particle size, reduction extent of the support, specific surface area, pore volume, pore size, and Ir oxidation state.

Currently developed synthesis methods enable the design of three different catalytic families containing high number of active Ir sites with high activity in the CO oxidation reaction which may help the development of prospective cost-effective oxidation catalysts.

References

[1] D. Vallero, Fundamentals of Air Pollution, 5th Edition, Academic Press, 9780124046023, 54-59, 2014

[2] C. Stern, Air Pollution: The Effects of Air Pollution, 3rd Edition, Elsevier, 9780323139977, 117-124, 3, 2010

[3] P. Landrigan, Air Pollution and Health, The Lancet Publication, 2468-2667(16)30023-8, 111-119, 2, 2017

[4] R. Harrison, Handbook of Air Pollution Analysis, Springer Science & Business Media, 9789400940833, 237-245, 2012

[5] M. Jerrett, Nature, 525, 330–331, 2015

[6] J. Lelieveld, J. S. Evans, M. Fnais, D. Giannadaki & A. Pozzer, Nature, 525, 367–371 2015.

[7] Jon G Ayres, Robert L Maynard, Roy J Richards, Air Pollution And Health, World Scientific, 9781783261918, 3, 107-119, 2006

[8] G. C. Koltsakis, I. P. Kabdylas & A. M. Stamatelos, Three-Way Catalytic Converter Modeling and Applications, Taylor & Francis, 0098-6445, 164, 153-189, 2018

[9] M. Twigg, Applied Catalysis, 70, 2-15, 2007

[10] H. Hirata, Catalysis Surveys, 18, 128–133, 2014

[11] D. Johnson, P. Gallagherr, E. Vogell, Journal of Catalysis, 48, 87-97, 1977

[12] A.S. Ivanova, E.M. Slavinskaya, R.V. Gulyaev, V.I. ZaikovskiiI, Applied Catalysis, 97, 57-71, 2020

[13] G. Spezzati, Y. Su, P. Hofmann, A. Benavidez, A. Abhaya, and M. Hensen, ACS Catal, 7, 6887−6891, 2017

[14] A. Therrien, R. Hensley, D. Marcinkowski, R. Lucci, C. Schilling, Jean-Sabin McEwen & E. Charles, Nature Catalysis, 1, 192–198, 2018

[15] H.-J.Freund, G. Meijer, M. Scheffler, R. Schlçgl, M. Wolf, Angew. Chem. Int. Ed. 2011, 50, 10064 – 1009

[16] You Zhou, Zongyuan Wang and Changjun Liu, Catal. Sci. Technol., 2015, 5, 69.

[17] Hung-Chi Wu, Tse-Ching Chen, Nien-Chu Lai, Chia-Min Yang, Jia-Huang Wu,

Yan-Chu Chen, Jyh-Fu Leed and Ching-Shiun Chen, Nanoscale, 2015, 7, 16848

[18] S. Senanayake, D. Stachiolla, and J. Rodriguez, ACS Catal, 46, 1702-1711, 2013

[19] Jason R. Gaudet, Andrew de la Riva, Eric J. Peterson, Trudy Boli, and Abhaya K. Datye, ACS Catal. 2013, 3, 5, 846–855

[20] Z. Luo, D. Yuan, F. Zhang, Y. Wang, Y. Li, and L. Zhu, Nano Energy, 62, 653-659, 2019

[21] Shilong Chen, Liangfeng Luo, Zhiquan Jiang, and Weixin Huang, ACS Catal. 2015, 5, 3, 1653–1662

[22] Mayfair C. Kung, Robert J. Davis, and Harold H. Kung, J. Phys. Chem. C 2007, 111, 32, 11767–11775

[23] J. Raub, M. Nolf, B. Hampson, S. Thom, Toxicology 145 (2000) 1 – 14

[24] Hao Chen, Jie Fu, Pengfei Zhang, Honggen Peng, de Carter W. Abney,

Kecheng Jie, Xiaoming Liu, Miaofang Chi and Sheng Dai, J. Mater. Chem. A, 2018, 6, 11129

[25] Philip G. Harrison, Ian K. Ball, Wan Azelee, Wayne Daniell, and Daniella Goldfarb, hem. Mater. 2000, 12, 12, 3715–3725

[26] Botao Qiao, Aiqin Wang, Xiaofeng Yang, Lawrence F. Allard, Zheng Jiang, Yitao Cui, Jingyue Liu, Jun Li & Tao Zhang, Nature Chemistry, 3, 634–641, 2011

[27] Qiuxia Cai, Xinde Wang, and Jian-guo Wang, J. Phys. Chem. C 2013, 117, 41, 21331–21336

[28] Mingming Du, Daohua Sun, Hongwei Yang, Jiale Huang, Xiaolian Jing, Tareque Odoom-Wubah, Haitao Wang, J. Phys. Chem. C 2014, 118, 33, 19150–19157

[29] K. Grass and G. Lintz, JOURNAL OF CATALYSIS, 172,446–452, 1997

[30] Yu Bai, Wenhua Zhang, Zhenhua Zhang, Jie Zhou, Xijun Wang, Chengming Wang, Weixin Huang, Jun Jiang, and Yujie Xiong, J. Am. Chem. Soc. 2014, 136, 42, 14650–14653

[32] H. Cordatos and R. Corte, JOURNAL OF CATALYSIS, 157, 222-226, 1995

[33] P. Muller and R. Kern, Surface Science, 457, 229-253, 2000

[34] A. Kiejna, K.F. Wojciechowski, Metal Surface Electron Physics, Elsevier, 9780080536347. 108-114, 1996

[35] F. Pederen and P. Andersson, Surface Science 601 (2007) 1747–1753

[36] Yi Gao, Nan Shao, Yong Pei, Zhongfang Chen, and Xiao Cheng Zeng, ACS Nano 2011, 5, 10, 7818–7829

[37] M. Kipnis, Applied Catalysis, 152-153, 38-45, 2014

[38] W. Fang, and L. Zhi, Acta Physico-Chimica Sinica, 28, 6, 2012, 1455-1460(6)

[39] G. Ertl, F. Schuth, and J. Wietkamp, Handbook of Heterogeneous Catalysis, WILEY-VCH, 2nd Edition, 5, 2008

[40] D. Kuling and Y. Uzoumi, Handbook of Heterogeneous Catalysis, WILEY-VCH, 3rd Edition, 2008

[41] Lichen Liu and Avelino Corma, Chem. Rev. 2018, 118, 4981−5079

[42] X. Feng, B. Qiao, J. Li, and T. Zhang, ACS, 1740–1748, 2013, 46, 8

[43] Jiayu Chen, Yongjin Wanyan, Jianxin Zeng, Huihuang Fang, Zejun Li, Yongdi Dong, Ruixuan Qin, Changzheng Wu, Deyu Liu, Mingzhi Wang, Qin Kuang, Zhaoxiong Xie, and Lansun Zheng, ACS Sustainable Chem. Eng. 2018, 6, 14054−14062

[44] Hua Xie, Min Hong, Emily M. Hitz, Xizheng Wang, Mingjin Cui, Dylan J. Kline, Michael R. Zachariah,and Liangbing Hu, J. Am. Chem. Soc. 2020, 142, 17364−17371

[45] Arno Bergmann and Beatriz Roldan Cuenya, ACS Catal. 2019, 9, 10020−10043

[46] Y. Zheng, H. Xiao, K. Li, Y. Wang, X. Zhu, and H. Wang, ACS Appl. Mater. Interfaces 2020, 12, 37, 42274–42284

[47] Li Cheng Kao, aYifan Ye, Yi-Sheng Liu, Chung Li Dong, Jinghua Guo, and Sofia Ya Hsuan Liou, : J. Mater. Chem. A, 2018, 6, 10663

[48] Haiping Li, Tianxing Yang, Yiwei Jiang, Shuai Chen, Yufei HeJunting, Feng Dianqing, Journal of Catalysis, 385, 313-321, 2020

[49] Zhennan Huang, Pengfei Xie, Tangyuan Li, Steven D. Lacey, Miaolun Jiao, Hua Xie, Kun Kelvin Fu, Rohit Jiji Jacob, Dylan Jacob Kline, Yong Yang, Michael R. Zachariah, Chao Wang, Reza Shahbazian-Yassar, and Liangbing Hu, ACS Appl. Mater. Interfaces 2019, 11, 33, 29773–29779

[50] Sharon Mitchell, Ruixuan Qin, Nanfeng Zheng & Javier Pérez-Ramírez, Nature Nanotechnology, 16, 129–139, 2021

[51] Gregory Tate, Nathan Robert Leaphart, and John R. Regalbuto, ACS Catal. 2018, 8, 11, 10383–10391

[52] F Kapteijn, RJ Berger, JA Moulijn, AE van Diepen, H van Bekkum, Handbook of Heterogeneous Catalysis, WILEY_VCH, 978-3-527-31241-2, 2nd Edition, 1173-1190, 2008

[53] J. Ancheyta, Chemical Reaction Kinetics, WILEY-VCH, 978-1119226642, 1st Edition,212-231

[54] Toolenaar, F. J. C. M.; Bastein, A. G. T. M.; Ponec, V. The Effect of Particle Size in the Adsorption of Carbon Monoxide on Iridium: An Infrared Investigation. *J. Catal.* **1983**, *82* (1), 35–44.

[55] Cao, W.; Lin, L.; Qi, H.; He, Q.; Wu, Z.; Wang, A.; Luo, W.; Zhang, T. In-Situ Synthesis of Single-Atom Ir by Utilizing Metal-Organic Frameworks: An Acid-Resistant Catalyst for Hydrogenation of Levulinic Acid to γ-Valerolactone. *J. Catal.* **2019**, *373*, 161–172.

[56] Haneda, M.; Fujitani, T.; Hamada, H. Effect of Iridium Dispersion on the Catalytic Activity of Ir/SiO_2 for the Selective Reduction of NO with CO in the Presence of O_2 and SO2. *J. Mol. Catal. A Chem.* **2006**, *256* (1), 143–148.

[57] Ivanov, A. V; Kustov, L. M. State of Iridium Supported on SO_4/ZrO_2. *Russ. Chem. Bull.* **1998**, *47* (11), 2124–2128.

[58] Lu, Y.; Wang, J.; Yu, L.; Kovarik, L.; Zhang, X.; Hoffman, A. S.; Gallo, A.; Bare, S. R.; Sokaras, D.; Kroll, T.; Dagle, V.; Xin, H.; Karim, A. M. Identification of the Active Complex for CO Oxidation over Single-Atom Ir-on-$MgAl_2O_4$ Catalysts. *Nat. Catal.* **2019**, *2* (2), 149–156.

[59] Chen, L.; Ali, I. S.; Sterbinsky, G. E.; Zhou, X.; Wasim, E.; Tait, S. L. Ligand-Coordinated Ir Single-Atom Catalysts Stabilized on Oxide Supports for Ethylene Hydrogenation and Their Evolution under a Reductive Atmosphere. *Catal. Sci. Technol.* **2021**, *11* (6), 2081–2093.

[60] Hoffman, A. S.; Fang, C.-Y.; Gates, B. C. Homogeneity of Surface Sites in Supported Single-Site Metal Catalysts: Assessment with Band Widths of Metal Carbonyl Infrared Spectra. *J. Phys. Chem. Lett.* **2016**, *7* (19), 3854–3860.

[61] McVicker, G. B.; Baker, R. T. K.; Garten, R. L.; Kugler, E. L. Chemisorption Properties of Iridium on Alumina Catalysts. *J. Catal.* **1980**, *65* (1), 207–220.

[62] Adam S. Hoffman,Chia-Yu Fang, and Bruce C. Gates, J. Phys. Chem. Lett. 121, 34-47, 2017.

[63] Beutel, T.; Kawi, S.; Purnell, S. K.; Knoezinger, H.; Gates, B. C. Tetra- and Hexanuclear Iridium Clusters in NaY Zeolite: Characterization by Infrared Spectroscopy. J. Phys. Chem. 1993, 97 (28), 7284–7289.

[64] Kawi, S.; Chang, J. R.; Gates, B. C. Tetrairidium Clusters Supported on .Gamma.-Alumina: Formation from [Ir4(CO)12] and Carbon Monoxide-Induced Morphology Changes. J. Phys. Chem. 1993, 97 (20), 5375–5383.

[65] Li, F.; Gates, B. C. Metal Carbonyl Cluster Synthesis in Nanocages: Spectroscopic Evidence of Intermediates in the Formation of Ir4(CO)12 in Zeolite NaY. J. Phys. Chem. B 2004, 108 (31), 11259–11264.

[66] Tanaka, K.; Watters, K. L.; Howe, R. F. Characterization of Supported Iridium Catalysts Prepared from Ir4(CO)12. J. Catal. 1982, 75 (1), 23–38.

[67] Gelin, P.; Coudurier, G.; Taarit, Y. B.; Naccache, C. Formation of Iridium Carbonyl Complex in NaY Zeolite. J. Catal. 1981, 70 (1), 32–40.

[68] Hernández-Cristóbal, O.; Díaz, G.; Gómez-Cortés, A. Effect of the Reduction Temperature on the Activity and Selectivity of Titania-Supported Iridium Nanoparticles for Methylcyclopentane Reaction. Ind. Eng. Chem. Res. 2014, 53 (24), 10097−10104.

[69] X. Wang, A. Qiao, B. Li, J. Liu, J. Zhang, and T. Acc. Chem. Res. 2013, 46, 1740−1748.

[70] Joaquin Resasco, Sheng Dai, George Graham, Xiaoqing Pan, and Phillip Christopher, J. Phys. Chem. C 2018, 122, 25143−25157

[71] Matsubu, J. C.Yang, V. Christopher. J. Am. Chem. Soc. 2015, 137, 3076−3084.

[72] K. Hadjiivanov and G. Vayssilov. Adv. Catal. 2002, 47, 307−511.

[73] H. Miessner, J. Burkhardt, D. Gutschick, A. Zecchina,. J. Chem. Soc., Faraday Trans. 1 1989, 85, 2113−2126.

[74] M. Mihaylov, V. Ivanova, E. Thibault-Starzyk, F. Daturi. J. Phys. Chem. B 2006,

[75] Ma. Schaube, Rotraut Merkle, and Joachim Maier, J. Phys. Chem. C 2020, 124, 34, 18544–18556

[76] P. Cop, M. Göttlicher, J. Schörmann, C. Boissiere, A. Beyer, C. Becker, K. Volz, H. Over, and B. M. Smarsly, J. Phys. Chem. C 2019, 123, 20, 12851–12861

[77] Taeyoon Kim, John M. Vohs, and Raymond J. Gorte, Ind. Eng. Chem. Res. 2006, 45, 16, 5561–5565

[78] A. V. Chadwick, G. Mountjoy, V. M. Nield, I. J. F. Poplett, M. E. Smith, J. H. Strange, and M. G. Tucker, Chem. Mater. 2001, 13, 4, 1219–1229

[79] M. Mehdipour, H. Tabaian, and S. Firoozi, Ceramic International, 45, 71-80, 2019

[80] Ming Guo, Jiqing Lu, Yanni Wu, Yuejuan Wang, and Mengfei Luo, Langmuir 2011, 27, 7, 3872–3877

[81] Lan Chen, Pete Fleming, Virginia Morris, Justin D. Holmes, and Michael A. Morris, J. Phys. Chem. C 2010, 114, 30, 12909–12919.

[82] Ann-Kathrin Elger, Julian Baranyai, Kathrin Hofmann, and Christian Hess, ACS Sens. 2019, 4, 6, 1497–1501

[83] Meijun Li, Zhaochi Feng, Pinliang Ying, Qin Xin and Can Li, Phys. Chem. Chem. Phys., 2003, 5, 5326–5332

[84] Sulaiman N Basahel, Tarek T Ali, Mohamed Mokhtar, and Katabathini Narasimharao, Nanoscale Research Letters (2015) 10:73

[85] Junwei Xu, Yan Zhang, Xianglan Xu, Xiuzhong Fang, Rong Xi, Yameng Liu, Renyang Zheng, and Xiang Wang, ACS Catal. 2019, 9, 5, 4030–4045

[86] Franklin D. Hardcastle, Hidetaka Ishihara, Rajesh Sharmac and Alexandru S. Biris, : J. Mater. Chem., 2011, 21, 6337

[87] A.P. Naumenko, N.I. Berezovska, M.M. Biliy, O.V. Shevchenko, PHYSICS AND CHEMISTRY OF SOLID STATE, 9, 1, 2008, 121-125

[88] C. Wulfman, M. Sadoun, and M. Lamy, IRBM 31 (2010) 257–262

[89] Verena Pfeifer, Travis E. Jones, Juan J. Velasco Vélez, Cyriac Massué, Rosa Arrigo, Detre Teschner, Frank Girgsdies, Michael Scherzer, Mark T. Greiner, Jasmin Allan, Maike Hashagen, Gisela Weinberg, Simone Piccinin,e Michael Hävecker, Axel Knop-Gericke, and Robert Schlögla, Surf. Interface Anal. 2016, 48, 261–273

[90] Qingyong Wu , Di Xu , Ning Xue, Tengyi Liu, Min Xiang and Peng Diao, Phys. Chem. Chem. Phys., 2017, 19, 145-154

[91] Ziba S. H. S. Rajan, Tobias Binninger, Patricia J. Kooyman, Darija Susac a and Rhiyaad Mohamed, Catal. Sci. Technol., 2020,10, 3938

[92] Verena Pfeifer, Travis E. Jones, Juan J. Velasco elez, Rosa Arrigo,Simone Piccinin, Michael avecker, Axel Knop-Gerickea and Robert Schloglac, Chem. Sci., 2017, 8, 2143

[93] Regina M. Kluge , Richard W. Haid , Aliaksandr S. Bandarenka, Journal of Catalysis 396 (2021) 14–22

[94] R. Eloirdi, P. Gakir, F. Huber, and T. Gouder, Applied Surface Science, 457, 566-571, 2018

[95] J. Mysilvecek, V. Matolin, and I. Matolinova, Materials 2015, 8(9), 6346-6359

[96] Yi Zhang, Liangjie Fu, Zhan Shu, Huaming Yang, Aidong Tang & Tao Jiang. Nanoscale Research Letters, 12, 456 (2017)

[97] M. Gondal, A. Fasasi, Baig, Umair; Mekki, Journal of Nanoscience and Nanotechnology, 18, 6, 2018, 4030-4039

[98] Hayat Khan, Imran Khan Swati, Mohammad Younas, Asmat Ullah, International Journal of Photoenergy, 17, 2017

[99] M. Hierro-Oliva, A. M. Gallardo-Moreno & M. L. González-Martín, Metallurgical and Materials Transactions, 45, 6285–6290, 2014

[100] Marina Massaro, Carmelo G. Colletti, Giuseppe Lazzara, Susanna Guernelli, Renato Noto, and Serena Riela, ACS Sustainable Chem. Eng. 2017, 5, 4, 3346–3352